

Investigations on Turbulence Impacted Structured Laser Beams for Free-Space Optical Communications

A thesis submitted
in partial fulfilment for the award of the degree of

Doctor of Philosophy

in

Physics

by

Lekshmi S R



Department of Physics
Indian Institute of Space Science and Technology
Thiruvananthapuram, India
March 2024

CERTIFICATE

This is to certify that the thesis titled '*Investigations on Turbulence Impacted Structured Laser Beams for Free-Space Optical Communications*', submitted by **Lekshmi S R**, to the Indian Institute of Space Science and Technology, Thiruvananthapuram, in partial fulfilment for the award of the degree of **Doctor of Philosophy in Physics**, is a *bona fide* record of research work carried out by her under my supervision. The contents of this thesis, in full or in parts, have not been submitted to any other Institute or University for the award of any degree or diploma.

Prof. C.S. Narayanamurthy

Outstanding Professor

Department of Physics

Dr. Sudheesh Chethil

Professor & Head

Department of Physics

Place:Thiruvananthapuram

Date: March 2024

DECLARATION

I declare that this thesis titled '*Investigations on Turbulence Impacted Structured Laser Beams for Free-Space Optical Communications*', submitted in partial fulfilment for the award of the degree of Doctor of Philosophy in Physics is a record of original work carried out by me under the supervision of Prof. C.S. Narayanamurthy, and has not formed the basis for the award of any degree, diploma, associateship, fellowship, or other titles in this or any other Institution or University of higher learning. In keeping with the ethical practice in reporting scientific information, due acknowledgments have been made wherever the findings of others have been cited.

Place: Thiruvananthapuram

Date: March 2024

Lekshmi S R

(SC18D042)

ACKNOWLEDGEMENTS

I express my sincere gratitude to my supervisor Prof. C S Narayanamurthy for holding a space for me to evolve into an independent researcher. I wholeheartedly thank his patience and support during the challenging times. I acknowledge his vision for setting up one of the finest optical laboratories in the country and I am grateful for having the privilege to carry out my research under his guidance in the well-equipped laboratory facility.

I would like to extend my heartfelt gratitude to Dr . Dinesh N Naik, for the time and effort he has taken for helping me solve many of the difficulties I faced during my tenure. His resourcefulness has tremendously improved the quality of my research work.

A sincere thanks to my doctoral committee members for their constructive comments, timely evaluation, and insightful discussions.

I am thankful to CSIR India for the financial support and IIST for providing the opportunity to embark on my research career.

I express my gratitude to all my lab mates, friends, faculty members, and staff of IIST for creating a healthy workspace.

I am grateful to all my teachers and the public education system for bringing up the best in me.

I would like mention Vaisakhan for all the help he has provided during the uncertain times of my PhD journey.

I am thankful to my friends for their unwavering faith in me.

I am forever indebted to Kiran for being my lifeline.

I take this moment to acknowledge the blessing of having a supportive family.

I am eternally grateful to my grandmothers for their unconditional love and making me feel that I matter.

I thank my sister-in-law for her love and support. My heartfelt gratitude to my parents and my brother for always being at my side and respecting my choices. I owe everything I achieved in my life to them.

Finally, I am grateful to Rithu for lighting up even the darkest days of my life.

Dedicated to all the pioneering women in science for their brilliance, extraordinary perseverance, and courage in breaking stereotypes and igniting a path of inspiration for generations to come.

ABSTRACT

There is a renewed interest in wave propagation analysis through turbulent and turbid media because of its wide range of applications ranging from astronomical to biomedical imaging. Researchers have been constantly trying to optimise the free space optical communication systems without or with the minimal use of adaptive optics system. Many attempts have been made to optimize the transmitting beams to improve communication efficiency. Such optimization of transmitting beams consists of many methods like altering their degree of coherence, and degree of polarization, or using different classes of beam shapes. In this thesis, different classes of beams are analysed after passing through a laboratory level turbulence simulator to see their potential to be used in free space communication systems.

The main objective of the thesis is to investigate the effect of atmospheric turbulence when different structured laser beams are propagated through it. We considered different classes of beams in different coherence regimes and their resilience to the impact of dynamic turbulence is thoroughly studied.

In the first section, the Fried coherence length of the rotating pseudo random phase plate is calculated. This work describes a new approach for determining the Fried's coherence length of a dynamic Kolmogorov type turbulence in a laboratory setting. The autocorrelation function generated from the quantitative properties of a rotating PRPP in one of the arms of a Mach-Zehnder interferometer is used in this method and the Fried parameter is found out with a better accuracy.

The next session of the thesis deals with the wave propagation analysis of partially coherent Gaussian-Schell model beams, zero order Bessel-Gaussian beams and partially coherent Gaussian vortex beams through a rotating pseudo random phase plate. The effect of turbulence is quantitatively characterized by calculating their scintillation index, beam wandering and Zernike polynomials and qualitatively by finding the intensity line profiles at the laboratory level. The experimental results are further extended and verified using simulations. It was found that certain classes of beams under certain criteria show more resilience to the impact of turbulence making them desirable for free space optical communication purposes.

Towards the end of the thesis, the phenomenon of enhanced backscattering is studied using Laguerre Gaussian and Bessel-Gaussian beams. These beams are focused onto a detector after passing through a rotating dynamic turbulence twice. The backscattered rays are examined. When a beam is reflected off a retroreflector, it exhibits enhanced backscattering. When we employ a typical Gaussian beam, the amplification factor approaches two, and it decreases as the topological charge increases. The BG beam also exhibits enhanced backscattering, with an enhancement factor comparable to that of Gaussian beam. Along with the increased backscatter, the endurance of the BG beams is preserved as compared to the other incident beams.

Table of Contents

CERTIFICATE	i
DECLARATION	iii
ACKNOWLEDGEMENTS	v
ABSTRACT.....	ix
List of Figures	xiv
List of Tables	xvi
ABBREVIATIONS	xvii
NOTATIONS.....	xviii
CHAPTER 1	1
INTRODUCTION	1
1.1 Overview	1
1.2 Free-space Optical Communication Systems.....	1
1.3 Atmospheric Turbulence	2
1.3.1 Kolmogorov theory of turbulence.....	2
1.3.2 Mitigating the Effect of Turbulence	6
1.4 Structured Light Beams.....	7
1.5 Research Objectives	9
1.6 Organization of the Thesis	9
CHAPTER 2	11
FRIED'S COHERENCE LENGTH MEASUREMENT OF DYNAMIC KOLMOGOROV TYPE TURBULENCE USING THE AUTOCORRELATION FUNCTION.....	11
2.1 Introduction.....	11
2.2 Experimental Procedure and Theory	12
2.2.1 Pseudo Random Phase Plate (PRPP)	12
2.2.2 Experimental scheme	15
2.3 Results and Discussion	18
2.3.1 Calculation of percentage error and probable sources of errors	20
2.3.2 Comparison of the proposed scheme with the previously reported methods.	21
2.4 Conclusion	25
CHAPTER 3	27
INSENSITIVITY OF PARTIALLY COHERENT GAUSSIAN-SCHELL MODEL BEAMS TO THE IMPACT OF DYNAMIC KOLMOGOROV TYPE TURBULENCE.....	27
3.1 Introduction.....	27

3.2 Theoretical background and simulations.	28
3.2.1 Simulation.....	28
3.3 Experimental Procedure.....	28
3.3.1 Single passage.....	28
3.3.2 Double passage	29
3.4 Results and Discussion	30
3.4.1 GSM beams simulated using CS and PI methods.....	30
3.4.2 Experimental observations.....	31
3.4.3 Scintillation index	32
3.4.4 Beam wandering calculations.	36
3.4.5 Zernike coefficients evaluation.....	37
3.5 Conclusion	39
CHAPTER 4	41
THE RESILIENCE OF ZERO ORDER BESSEL-GAUSSIAN BEAMS TO THE IMPACT OF DYNAMIC KOLMOGOROV TYPE OF TURBULENCE.....	41
4.1 Introduction.....	41
4.2 Experimental Procedure and Theory	42
4.2.1 Bessel Gaussian beams (BG beams).....	42
4.2.2 Generation of BG beams using an axicon.....	42
4.2.3 Simulation scheme	43
4.2.4 Experimental scheme	44
4.3 Results and Discussion	45
4.3.1 Line profiles	45
4.3.2 Scintillation index	48
4.3.3 Beam wander	49
4.3.4 Simulation studies.....	51
4.4 Conclusions.....	58
CHAPTER 5	61
ROBUSTNESS OF PARTIALLY COHERENT VORTEX BEAMS TO THE IMPACT OF DYNAMIC KOLMOGOROV KIND OF TURBULENCE.....	61
5.1 Introduction.....	61
5.2 Experimental Procedure and Theory	61
5.3 Simulation Scheme	62
5.4 Results and Discussion	62
5.4.1 Amplitude and phase images of GSM beams	62

5.4.2 Experimental observations	63
5.4.3 Line profiles	64
5.4.4 Scintillation index	67
5.4.5 Simulation results.....	68
5.5 Conclusion	71
CHAPTER 6	73
ENHANCED BACKSCATTERING THROUGH TURBULENCE.....	73
6.1 Introduction.....	73
6.2 Theoretical Description of EBS	74
6.3 Experimental	76
6.4 Results and Discussion	78
6.5 Conclusion	82
CHAPTER 7	83
CONCLUSION AND FUTURE SCOPE	83
7.1 Conclusions.....	83
7.2 Future Perspectives	84
REFERENCES	87
List of Papers Based on the Thesis	95
• Journal papers.....	95
• Conference papers	95
• Papers under preparation.....	95

List of Figures

Figure. 1. 1 Block diagram of a typical FSO communication system.	2
Figure 2. 1 Photograph of a pseudo random phase plate.	12
Figure 2. 2 Principle of Near-Index-Match (NIM TM)	12
Figure 2. 3 Schematic representation of PRPP.	14
Figure 2. 4 Photograph of a PRPP mount	14
Figure. 2. 5 Schematic of experimental setup used for correlation measurements.	17
Figure. 2. 6 Clockwise rotation of PRPP	18
Figure. 2. 7 Autocorrelation coefficient corresponding to different movespeeds for 36 FPS.	19
Figure. 2. 8(a) is the image captured at CCD before inserting PRPP. (b) shows the distorted pattern after inserting PRPP into the set up.	20
Figure. 2. 9 (a) to (d) represent the sequential images captured with rotating PRPP.	22
Figure. 2. 10 (a) to (d) represent the phase map of sequential images.	23
Figure. 2. 11 shows the phase map with five chosen points A, B, C, D and E for correlation measurements. Red arrow shows the direction of the fringe movement due to the rotation of PRPP.	23
Figure. 2. 12 Autocorrelation for five different points for the sequential images captured.	24
Figure 3. 1 shows the experimental setup for single passage geometry. SFA is spatial filter assembly and L is the collimating lens. SLM denotes spatial light modulator. A is an aperture and M denotes a mirror. PRPP is the pseudo random phase plate, ND denotes neutral density filter while BS is a beamsplitter. CCD and SHWFS are respectively the camera and Shack Hartmann wavefront sensor.	29
Figure 4. 1 Generation of Bessel Gaussian beam using an axicon of opening angle α . BG beams are formed in DOF (depth of focus) region.	42
Figure. 4. 2 shows the scheme used for simulation studies. BG denotes Bessel-Gaussian beams.	43
Figure. 4. 3 (a) shows the experimental setup for the generation of BG beams and passage through PRPP.	44
Figure. 4. 4 line profiles corresponding to BG beams of varying axicon angle (a-e) and conventional Gaussian beam(f).	45
Figure. 4. 5 Images captured using CCD and their corresponding line profiles before and after turbulence impact.	47
Figure. 4. 6 shows the scintillation index corresponding to turbulence-impacted BG beams in Fourier, Fresnel and Fraunhofer regions corresponding to the simulation geometry shown in Fig. 4. 2.	48
Figure. 4. 7 shows the beam wander corresponding to turbulence-impacted BG beams simulated using different axicons.	50
Figure. 4. 8 Schematic representation of the PRPP. Shaded region represents the area of phase aberrations. Point A shows the input beam and arrow shows the direction of rotation of the PRPP.	50
Figure 5. 1 shows the experimental setup where SFA denotes the spatial filter assembly and L is the collimating lens. VPP is the vortex phase plate while SLM denotes the spatial light modulator. A is an aperture and M denotes a mirror. PRPP is the pseudo-random phase plate,	

ND denotes a neutral density filter while BS is a beamsplitter. CCD is the camera used for recording images.....	62
Figure 6. 1 Ray model of double passage through the phase screen P using the reflector R. .	74
Figure 6. 2 Schematic of experimental set up for double passage of Gaussian vortex beams through the PRPP.....	77
Figure 6. 3 Schematic of experimental set up for double passage of BG beams through the PRPP	77
Figure 6. 4 (a) shows the average intensity obtained at the CCD plane	79
Figure 6. 5 shows the intensity line profiles of backscattered beams. (a)-(c) show the line profiles corresponding to Gaussian vortex beams respectively having charges zero, two and four. (d) shows the intensity line profile of backscattered BG beam.....	81
Figure 6. 6 shows the enhancement factor for different beam shapes. L0 denoted Gaussian beam, L2 and L4 denote Gaussian vortex beams having topological charges two and four respectively. BG means the Bessel-Gaussian beam generated using an axicon of opening angle one degree.	81
Figure 6. 7 shows the scintillation index for different beam shapes. L0 denoted Gaussian beam, L2 and L4 denote Gaussian vortex beams having topological charges two and four respectively. BG means the Bessel-Gaussian beam generated using an axicon of opening angle one degree.....	81

List of Tables

Table 2. 1 Fried coherence length estimated for different points.	24
Table 3. 1 Percentage reduction in scintillation index from the value corresponding to a fully coherent source.	34
Table 3. 2 Percentage reduction in beam wander from the value corresponding to a fully coherent source.	36
Table 4. 1 The calculated scintillation index and speckle sizes for BG beams and Gaussian beam in Fourier, Fresnel and Fraunhofer regions.	48
Table 4. 2 The calculated beam wander for BG beams and Gaussian beam in Fourier, Fresnel and Fraunhofer regions along x and y directions.....	50
Table 4. 3 Turbulence impacted BG beams for different propagation regions.	53
Table 4. 4 Turbulence impacted BG beams for different propagation regions	54
Table 4. 5 Turbulence impacted BG beams for different propagation regions	55
Table 5. 1 Turbulence impacted GSMV beams of topological charges zero to three for different propagation regions.....	70
Table 6. 1The values of enhancement factor , scintillation index and their percentage variation from the values corresponding to the conventional Gaussian beam.....	92

ABBREVIATIONS

FSO	Free Space Optics
PSD	Power Spectral Density
LG	Laguerre Gaussian
BG	Bessel Gaussian
HG	Hermite Gaussian
GSM	Gaussian Schell Model
GSMV	Gaussian Schell Model Vortex
PRPP	Pseudo Random Phase Plate
CCD	Charge Coupled Device
NIM	Near Index Matching
OPD	Optical Path Difference
SFA	Spatial Filter Assembly
BS	Beam Splitter
ND	Neutral Density
FPS	Frames per Second
MVS	Move speed.
HWHM	Half Width Half Maximum
CS	Complex Screen
PI	Phase and Intensity
CSD	Cross Spectral Density
SLM	Spatial Light Modulator
SHWFS	Shack Hartmann Wavefront Sensor
SI	Scintillation Index
BW	Beam wander
FCS	Fully Coherent Source
DOF	Depth of Focus
EBS	Enhanced Backscattering

NOTATIONS

D_ϕ -Phase structure function

n -Refractive index

L_0 -Outer scale

l_0 -Inner scale

r_0 -Fried's coherence length

θ_0 -Isoplanatic angle

ϕ -Phase

C_n^2 - Refractive index structure constant

f -focal length

χ -Autocorrelation coefficient.

δ -Coherence length

α -axicon angle

CHAPTER 1

INTRODUCTION

1.1 Overview

Optical communication has been an integral and inevitable part of human history. In free-space optical communications and astronomical imaging using ground-based telescopes, a light beam has to pass through several kilometres in the atmosphere. The presence of the atmosphere greatly hinders the quality of optical beams passing through it[1]. The impact of the atmospheric turbulence on the propagating light beam is observed as the intensity fluctuations (scintillation) and beam wandering[2–4]. These intensity fluctuations lead to an increase in the link error probability which will in turn reduce the overall performance[5]. The scintillating effect and beam wandering effect further introduce higher order aberrations which are, normally corrected using adaptive optics systems. A closed-loop real-time corrective system using adaptive optics requires high-end computational power and moving mechanical parts[2].

Free-space optical (FSO) communications, which complement the current wireless radio frequency channels, offer hope for resolving the pervasive "last mile" network issues and bridging the digital divide[6–8]. This is because of the non-requirement of licences and tariffs, practically unlimited bandwidth, link range of several kilometres, reliability of data transmission medium and cost effectiveness[9].

The following sections will give a brief introduction to the concepts of free-space optical communication systems, the phenomenon of atmospheric turbulence and theoretical background of the structured light beams.

1.2 Free-space Optical Communication Systems

FSO communication system comes under the broader optical wireless communications systems. These systems work by propagating infrared light through free space and an optical transceiver is used in the system at both ends to provide bidirectional communication. In order to overcome the capacity constraints affordably, FSO communications offers a line-of-sight, high-speed, and secure wireless technology that can help realize next-generation carrier grade high-reliability backbone and last-mile network access[10].

A typical FSO system consists of transmitter, channel, and receiver[11]. The primary purpose of a transmitter is to modulate the incoming message signal onto the optical carrier which will be passed through the atmospheric channel to the receiving end. The main components of the transmitter are the modulator, the optical source, and a transmitting telescope or optical antenna. Along with beam shaping, the telescope's moveable component is also in charge of beam tracking. Unlike fiber optical communication, here the atmosphere itself acts as the channel for communication. However, this channel is the main limiting factor of communication efficiency. Weather conditions like rain, fog, snow, cloud, or the presence of smog severely deteriorate the power of signal reaching the receiver. The sent data is recovered using the receiver. It is made up of a demodulator, a receiver telescope, and a very sharp optical bandpass filter[12]. Fig.1.1 shows the block diagram of a typical FSO communication system.

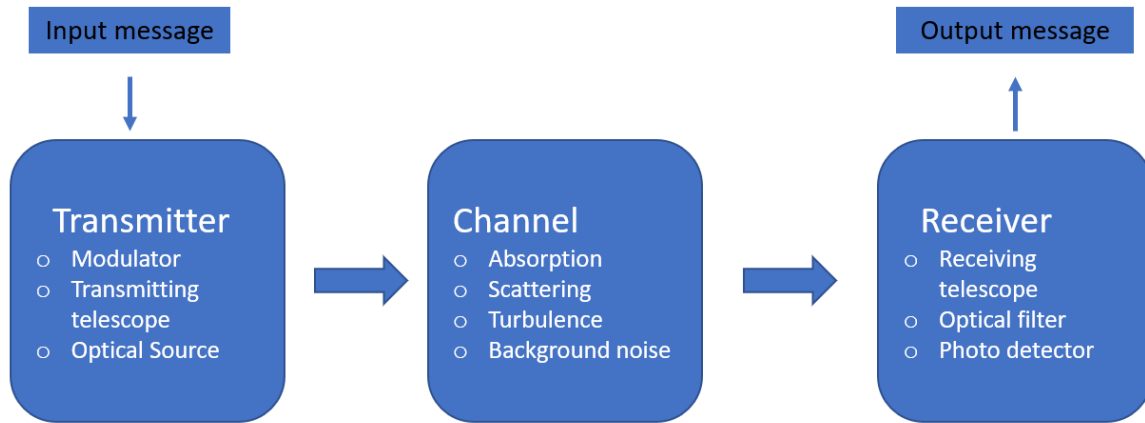


Figure. 1. 1 Block diagram of a typical FSO communication system.

1.3 Atmospheric Turbulence

As mentioned earlier, the atmospheric channel is the major limiting factor of an FSO communication system. Because of the wind and random temperature differences the atmosphere acts as a medium consisting of spatially and temporally varying refractive indices. This leads to the scattering and random deflection of the beam propagating through it[13–19]. In order to study the effect of atmosphere on the propagating beam we need to have a thorough understanding of the underlying physics of the phenomenon of turbulence. Since it is impossible to precisely characterize the spatial and temporal variations of refractive indices, statistical studies have to be implemented. There have been many statistical models to predict the behaviour of atmospheric turbulence among which the Kolmogorov theory of turbulence forms the basis. All these theories of turbulence are successful in relating these temperature fluctuations to refractive index fluctuations[19].

Turbulence in adaptive optics may be summed up using fundamental ideas that link physical turbulence phenomena to optical propagation and phase effects. Propagation through air turbulence is not well understood, particularly for small-scale instances. Because the complexity of the real atmosphere exceeds the powers of deterministic prediction or numerical analysis, turbulence theories are based on statistical studies. The emphasis on statistical modelling of air turbulence has resulted in a variety of extremely helpful theories and scaling laws that characterize the average impacts on gross parameters such as total beam wander, beam spread, and scintillation.

1.3.1 Kolmogorov theory of turbulence

Turbulent flow is a nonlinear process governed by the Navier-Stokes equations. Since it is extremely difficult to find a complete analytical solution to this equation for a fully developed turbulence, Kolmogorov proposed a statistical approach. According to his theory, in turbulent motions the kinetic energy in large eddies is transferred into smaller eddies. The average size of the larger eddies is called the outer scale and is denoted by L_0 . Near to the earth surface the value of L_0 is in the order of height above the ground and the value increases to tens to hundreds of meters as we go higher. Similarly, the inner scale is the average size of the smallest turbulent eddies and is denoted by l_0 . At scales smaller than the inner scale, the

energy dissipation caused by friction prevents turbulence from self-sustaining. The inner scale can range in values from a few millimetres close to the ground to a few centimetres above the ground. The range of eddy sizes between the inner and outer scales is termed as the inertial subrange[20]. The smaller eddies of turbulence deform the propagating wavefront which results in the random aberrations of the wavefront and intensity fluctuations. The outer scale deflects the beam from its original path which causes beam wandering and angle of arrival fluctuations. These effects are detrimental to the FSO communication systems[21,22].

Kolmogorov in his seminal work on the statistics of the turbulent flow developed an expression for the velocity structure function given by,

$$D_{ij} = \left\langle \left[v_i(r_1 + r) - v_i(r_1) \right] \left[v_j(r_1 + r) - v_j(r_1) \right] \right\rangle \quad (1.1)$$

It is not a simple equation to calculate using real velocity descriptors; however, the structure tensor may be reduced by making three assumptions about the atmosphere. First, the atmosphere is locally homogeneous (velocity is determined by the vector r); second, the atmosphere is locally isotropic (velocity is determined only by the magnitude of r); and third, turbulence is incompressible ($\nabla \cdot v = 0$). The tensor is now reduced to a single structural function, as ,

$$D_v(r) = \left\langle \left[v(r_i + r) - v(r_i) \right]^2 \right\rangle = C_v^2 r^{2/3} \quad (1.2)$$

The angle brackets in the above expression denote the statistical expectation operator, the scalar r is the magnitude of the position vector, $v(r_i)$ is the velocity vector point at r_i and C_v is the velocity structure constant.

This expression was further extended by Tatarskii [13] to derive at the expression for potential temperature θ . This potential temperature is linearly related to ordinary temperature T . The potential temperature structure function $D_\theta(r)$ follows the same power law as the velocity structure function.

$$D_\theta(r) = \begin{cases} C_\theta^2 l_0^{-4/3} r^2, & 0 \leq r \ll l_0 \\ C_\theta^2 r^{2/3}, & l_0 \ll r \ll L_0 \end{cases} \quad (1.3)$$

Where C_θ^2 is the structure parameter of θ .

The refractive index at point r is given by,

$$n(r) = \mu_n(r) + n_1(r) \quad (1.4)$$

Where $\mu_n(r) \cong 1$ is the mean value of the refractive index and $n_1(r)$ is the deviation from the mean value. At the visible spectrum the refractive index value attains the form,

$$n(r) = 1 + 77.6 \times 10^{-6} \left(1 + 7.52 \times 10^{-3} \lambda^{-2} \right) \frac{P(r)}{T(r)} \quad (1.5)$$

Where λ is the wavelength, P is the pressure in millibars and T is the temperature in Kelvin. When $\lambda = 0.5\mu m$ the value of refractive index becomes,

$$n(r) \cong 1 + 7.99 \times 10^{-5} \frac{P(r)}{T(r)} \quad (1.6)$$

Correspondingly the variation in the refractive index becomes,

$$dn = 7.99 \times 10^{-5} \left[dP - \left(\frac{-dT}{T^2} \right) \right] \quad (1.7)$$

If we consider the pressure of each eddy to be a constant Eqn.(1.7) becomes ,

$$dn = 7.99 \times 10^{-5} \frac{dT}{T^2} \quad (1.8)$$

Since the potential temperature θ is linearly proportional to the actual temperature T , the variation in the refractive index attains the form,

$$dn = 7.99 \times 10^{-5} \frac{d\theta}{T^2} \quad (1.9)$$

Note that the variation in refractive index is linearly related to the variation in the potential temperature. Hence the refractive index structure function follows the same power law as the potential temperature structure function given by,

$$D_n(r) = \begin{cases} C_n^2 l_0^{-4/3} r^2, & 0 \leq r \ll l_0 \\ C_n^2 r^{2/3}, & l_0 \ll r \ll L_0 \end{cases} \quad (1.10)$$

Here C_n^2 is the refractive index structure constant which is related to C_T^2 as,

$$C_n^2 = \left[77.6 \times 10^{-6} \left(1 + 7.52 \times 10^{-3} \lambda^{-2} \right) \frac{P}{T^2} \right]^2 C_T^2 \quad (1.11)$$

In general, the atmosphere is assumed to have mean refractive index of refraction $\langle n(r) \rangle$ and a fluctuating index part, $n_1(r)$. The covariance of the refractive index field B_n is given by,

$$B_n = \langle n_1(r + r_1) n_1(r_1) \rangle \quad (1.12)$$

It is desirable to have a spectral description of refractive-index fluctuations. The power spectral density (PSD) is defined as the Fourier transform of the covariance and is given by,

$$\Phi_n(K) = \frac{1}{(2\pi)^3} \int d^3r B_n(r) \exp(-iKr) \quad (1.13)$$

Where K is the three-dimensional spatial wave number.

Further for Kolmogorov kind of turbulence, the PSD is given by,

$$\Phi_n(K) = 0.033C_n^2 K^{-11/3} \quad (1.14)$$

If the finite inner and outer scales are considered we have the Von Karman spectrum given by,

$$\Phi_n(K) = \frac{0.033C_n^2}{(K^2 + K_0^2)^{11/6}} \text{ for } 0 \leq K \ll 1/l_0 \quad (1.15)$$

And we have the modified Von Karman spectrum as follows,

$$\Phi_n(K) = 0.033C_n^2 \frac{\exp(-K^2 / K_m^2)}{(K^2 + K_0^2)^{11/6}} \text{ for } 0 \leq K < \infty \quad (1.16)$$

Where $K_m = 5.92 / l_0$ and $K_0 = 2\pi / L_0$. The modified von Karman is the simplest PSD model that includes effects of inner scales as well as outer scales.

Typically, the values of refractive index structure constant range from $10^{-17} - 10^{-13} m^{-2/3}$ and is a measure of the intensity of local turbulence[22]. However, more useful quantities with more physical meanings exist. Furthermore, since C_n^2 is a function of the propagation distance z , single values may be used to characterise certain optical effects. As a result, parameters such as atmospheric coherence diameter r_0 and isoplanatic angle θ_0 are more commonly used.

The atmospheric coherence diameter r_0 also known as the Fried parameter is an important parameter which was first introduced by D. L. Fried. The Fried parameter is mathematically defined as[24,25],

$$r_0 = \left[0.423k^2 \sec(\beta) \int_0^{\Delta z} C_n^2(z) dz \right]^{-3/5} \quad (1.17)$$

Here β is the zenith angle, zero is the origin and Δz is the distance to the receiver while $k = 2\pi(f_x \hat{i} + f_y \hat{j})$ is angular spatial frequency in rad/m. The typical values of the Fried parameter ranges from five to ten centimetres for visible wavelengths.

Any optical system has a property called anisoplanatism[2], which means the optical properties of the system are not shift invariant. For the atmosphere the strength of the anisoplanatism can be computed using the angular structure function of the phase given by,

$$D_\phi(\Delta\theta) = \left\langle |\phi(\theta) - \phi(\theta + \Delta\theta)|^2 \right\rangle \quad (1.18)$$

Where θ is the angular coordinate and $\Delta\theta$ is the angular separation in the object field. The isoplanatic angle θ_0 is defined such that ,

$$D_\phi(\theta_0) = 1 \text{ rad} \quad (1.19)$$

Which can be computed using the equation,

$$\theta_0 = \left[2.91 k^2 \Delta z^{5/3} \int_0^{\Delta z} C_n^2(z) \left(1 - \frac{z}{\Delta z} \right)^{5/3} dz \right]^{-3/5} \quad (1.20)$$

The typical values of θ_0 are $5 - 10 \mu\text{rad}$.

Another useful parameter called the wave structure function for a plane wave in Kolmogorov turbulence regime given by,

$$D(|\Delta r|) = 6.88 \left(\frac{r}{r_0} \right)^{5/3} \quad (1.21)$$

With the knowledge of wave structure function and refractive index power spectral density the most useful parameter called the phase power spectral density can be calculated as is given by,

$$\Phi_\phi(k) = 2\pi^2 k^2 \Delta z \Phi_n(k) \quad (1.22)$$

For a plane wave in Kolmogorov turbulence regime the phase power spectral density reduces to,

$$\Phi_\phi(k) = 0.49 r_0^{-5/3} k^{-11/3} \quad (1.23)$$

In terms of frequency,

$$\Phi_\phi(f) = 0.023 r_0^{-5/3} f^{-11/3} \quad (1.24)$$

1.3.2 Mitigating the Effect of Turbulence

With the invention of the laser, free-space optical communication underwent a paradigm shift. The extreme directionality of laser beams enhanced the range and quality of data transmission. However, since the beam must pass through several kilometers of atmosphere, the quality of communication is still compromised [1]. The result of these impacts is manifested as scintillations and beam wandering. These distortions caused by the atmosphere can be addressed utilizing adaptive optics devices. It uses the phase conjugation method, deformable mirror systems, or segmented mirror systems to fairly recreate an aberration-free wavefront. A true adaptive optics system, on the other hand, necessitates very complicated equipment with moving mechanical parts and high-end computer capability. Because of these difficulties, it is almost impossible to provide real-time sensing and adjustments in a closed-loop for stronger turbulence. The optimization at the transmitter end would be a completely new way of looking at the problem. To fine-tune transmitting beam properties, several strategies such as changing the degree of coherence, degree of polarization, and employing different classes of beam shapes, called the structured light beams, have been used. [1,6,7,26-33]. There are some insightful results and observations which would pave a new direction to look at the problem of atmospheric turbulence and mitigation methods.

The next section provides a brief introduction to the basics of structured light beams.

1.4 Structured Light Beams

Electromagnetic fields in free space can be described by the Helmholtz equation given by[21],

$$\left[\nabla^2 + n^2 k^2 \right] E = 0 \quad (1.25)$$

Where E is the electric field, n is the refractive index and k is the wave number. In the case of uniformly polarised scalar fields, we can represent the electric field as a scalar field, U , a solution to the scalar Helmholtz equation.

$$\left[\nabla^2 + n^2 k^2 \right] U(s, z) = 0 \quad (1.26)$$

Where s is the transverse coordinate and z represents the propagation direction. Here we are only considering the spatial component in the paraxial regime. In cylindrical coordinates the solutions to the scalar Helmholtz equation are known as the Laguerre-Gaussian (LG) modes given by,

$$U(r, \phi, z) = E_0 \left(\sqrt{2} \frac{r}{\omega} \right)^l L_p^l \left(2 \frac{r^2}{\omega^2} \right) \frac{\omega_0}{\omega(z)} \exp[-i\psi_{pl}(z)] \times \exp \left[i \frac{k}{2q(z)} r^2 \right] \exp(il\phi) \quad (1.27)$$

Where $L_p^l(.)$ is the associated Laguerre polynomial, E_0 is a constant electric field amplitude, $\omega(z)$ is the beam size, ω_0 is the beam size at the beam waist, $z_0 = \pi\omega_0^2 / \lambda$ is the Rayleigh range, $q(z) = z - iz_0$ is the complex beam parameter, l is the topological charge of the mode carrying the orbital angular momentum and $\psi_{pl}(z) = (2p + l + 1) \tan^{-1}(z / z_0)$ is the Gouy phase shift.

In Cartesian coordinates the solution attains the form of Hermite-Gaussian (HG) mode given by,

$$U(x, y, z) = E_0 H_m \left(\sqrt{2} \frac{x}{\omega(z)} \right) H_n \left(\sqrt{2} \frac{y}{\omega(z)} \right) \frac{\omega_0}{\omega(z)} \times \exp[-i\psi_{mn}(z)] \exp \left[i \frac{k}{2q(z)} r^2 \right] \quad (1.28)$$

Here, $H_m(.)$ represents the Hermite polynomial and $\psi_{mn}(z) = (m + n + 1) \tan^{-1}(z / z_0)$ is the Gouy phase shift.

Similarly, in elliptical coordinates there exist a family of orthogonal solutions called the Ince-Gaussian modes represented by[26],

$$\begin{aligned}
U(\xi, \eta, z) = & D \frac{\omega_0}{\omega(z)} C_p^m(i\xi, \varepsilon) C_p^m(\eta, \varepsilon) \exp\left[\frac{-r^2}{\omega^2(z)}\right] \\
& \times \exp\left[ikz + \frac{ikr^2}{2R(z)} - i(p+1) \tan^{-1}\left(\frac{z}{zr}\right)\right]
\end{aligned} \tag{1.29}$$

where D represents the normalisation constant, ε denotes the ellipticity parameter while C_p^m is the even Ince polynomial of order p and degree m . The variables ξ and η are respectively the radial and angular elliptic coordinates, given by $x = \omega_0 \sqrt{\varepsilon/2} \cosh(\xi) \cos(\eta)$ and $y = \omega_0 \sqrt{\varepsilon/2} \sinh(\xi) \sin(\eta)$. It has to be noted that, for odd modes C_p^m will be replaced by odd Ince polynomials S_p^m .

In cylindrical coordinates we have Bessel-Gaussian (BG) beams having the general form,

$$\begin{aligned}
U(r, \phi, z) = & E_0 \frac{\omega}{\omega(z)} \exp[i\psi(z)] \exp\left[i \frac{k}{2q(z)} r^2\right] \\
& \times J_l\left(\frac{\beta r}{1 + iz/z_0}\right) \exp\left[\frac{\beta^2 z / (2k)}{1 + iz/z_0}\right] \exp[i l \phi]
\end{aligned} \tag{1.30}$$

where β is related to the wave vector of the plane waves which form the mode while J_l is the Bessel function of the l^{th} order. BG modes carry orbital angular momentum through the topological charge l .

Another regime of structured light beams comes under the class of partially coherent beams called the Gaussian-Schell model beams. Any physically realizable partially coherent beam can be synthesized using the superposition integral [27,28],

$$W(r_1, r_2) = \int \int_{-\infty}^{\infty} p(\nu) H(r_1, \nu) H^*(r_2, \nu) d^2 \nu \tag{1.31}$$

where, W is the cross-spectral density (CSD) of the source, p is a positive real function and H is the kernel and $r = xx + yy$.

For a Gaussian Schell model (GSM) beam cross-spectral density attains the following form [29],

$$W(r_1, r_2) = \exp\left(-\frac{r_1^2 + r_2^2}{4\sigma^2}\right) \exp\left(-\frac{|r_1 - r_2|^2}{2\delta^2}\right) \tag{1.32}$$

where, σ is the beam radius and δ is the coherence radius.

1.5 Research Objectives

Now, having defined the basic theory we can look into the research objectives and the scope of the work. The main objective of the thesis is to investigate the effect of atmospheric turbulence when different structured laser beams are propagated through it. We considered different classes of beams in different coherence regimes and their resilience to the impact of dynamic turbulence is thoroughly studied.

In the first part of thesis, the atmospheric simulator used in our experiments is quantitatively characterized by calculating the Fried coherence parameter. And in the latter part of the work, different classes of beams are passed through a dynamic turbulence. The effect of turbulence is quantitatively characterized by calculating their scintillation index, beam wandering and Zernike polynomials and qualitatively by finding the intensity line profiles.

1.6 Organization of the Thesis

- In the second chapter we propose a simple and straightforward method to find the Fried parameter of a laboratory level dynamic turbulence simulator. A novel method has been employed to calculate the Fried coherence length. We made use of the autocorrelation function of a single point in a two-dimensional phase map obtained from a Mach-Zehnder interferometer. Unlike the previously reported characterization techniques this method is straightforward uses a simple experimental set up and yields better accuracy.
- In the next chapter of the thesis, the effect of dynamic Kolmogorov kind of turbulence on Gaussian- Schell model (GSM) beams in different coherence regimes have been explored in detail. The propagation characteristics of such turbulence impacted beams are quantitatively verified at the laboratory level by calculating beam wandering, scintillation index, and Zernike polynomials.
- In the fourth chapter, we have generated Bessel-Gaussian (BG) beams through simulations and by using axicons. These BG beams and conventional Gaussian beams are passed through a dynamic transmissive Kolmogorov turbulence simulator. The scintillation index, beam wander and intensity line profiles are calculated for different axicon angles in Fresnel, Fourier and Fraunhofer regions and some interesting results are obtained.
- In chapter five, we generated Gaussian- Schell model vortex (GSMV) beams of different orders using a vortex phase plate and are passed through a dynamic transmissive Kolmogorov turbulence simulator. Scintillation index, beam wander and intensity line profiles are calculated for different coherence regimes. It has been experimentally verified that GSMV beams of higher orders show less scintillation and beam wander effects. And their resilience decreases as we increase the coherence width.
- Chapter six deals with the effect on Gaussian vortex beams and Bessel-Gaussian while passing through the turbulence twice. Enhanced backscattering effect is observed for these beams. The scintillation index is calculated for the beams under varied conditions and some useful results are obtained.
- The final chapter outlines the conclusion of the work and its future scope.

CHAPTER 2

FRIED'S COHERENCE LENGTH MEASUREMENT OF DYNAMIC KOLMOGOROV TYPE TURBULENCE USING THE AUTOCORRELATION FUNCTION.

2.1 Introduction

Realistic simulation of atmospheric turbulence is a main precursor before establishing any adaptive optics system. Atmospheric turbulence simulators help us effectively fine tune different parameters affecting the adaptive optics systems. However, it has to be made sure that these simulators correctly employ the prevalent laws that guide real atmospheric turbulence. Out of the available laboratory level turbulence mimicking media, transmissive type simulators with near index matching are widely used because of their ease of handling, cost effectiveness and ability to repetitively produce different turbulence strengths[30].

Pseudo random phase plates (PRPP, Lexitek Corporation, USA) [31,32] can be used to simulate various atmospheric turbulence regimes in a well-controlled fashion. Manufacturers of this random phase plate claim to have imprinted a Kolmogorov kind of turbulence with known Fried coherence length at a given wavelength. However, as we have to use phase plates for broad spectrum we have to make sure that these statistical estimations are still valid for different wavelengths[33,34].

One major concern that has to be considered is the compatibility between the detectors (CCDs, CMOSs, wavefront sensors etc.) and the dynamic random phase generators. Various parameters of the detector ,like aperture width, its ability to record the time varying phase structures, and pixel size have to be scrutinized thoroughly before employing them to any real adaptive optics system. Together with a well characterized atmospheric turbulence simulator and a compatible detector one can ensure a realistic adaptive optics system simulation.

Many attempts have been made to characterize pseudo random phase plates. These include phase estimations of turbulence impacted laser beams and a systematic characterization using angle-of-arrival fluctuations, Fried parameter, Hurst exponent, turbulence frequencies and the scintillation index[30].

Fried's coherence length is an intrinsic parameter of any type of turbulence system. It is essentially the strength of turbulence under consideration. One can find numerous techniques to find Fried parameter in literature for actual atmospheric conditions [35–37].A detailed comparison of three methods used to find Fried parameter is presented by Ann C. Slavin . All these techniques either use sophisticated instruments or complex calculations. For a laboratory level turbulence regime, angle of arrival fluctuations are usually carried out to estimate Fried parameter[30,38] . One article reports an off axis holographic scheme to calculate Fried parameter for a transmissive phasescreen[38].

Here, we propose a simple and straightforward method to find the Fried parameter of a laboratory level dynamic turbulence simulator. In this article first, we checked the compatibility of CCD to the temporally varying turbulence caused by the rotation of PRPP.

We used autocorrelation coefficients of the sequential images captured to check for continuity. Secondly, we characterised PRPP quantitatively by calculating Fried coherence length. A novel method has been employed to calculate the Fried coherence length. We made use of the autocorrelation function of a single point in a two-dimensional phase map obtained from a Mach-Zehnder interferometer. Unlike the previously reported characterization techniques this method is straightforward uses a simple experimental set up and yields better accuracy.

2.2 Experimental Procedure and Theory

2.2.1 Pseudo Random Phase Plate (PRPP)

Pseudo Random Phase Plate (PRPP) is a 3D atmospheric turbulence simulator manufactured by Lexitek [32]. PRPP along with its controlling systems have been purchased from Lexitek motors . It has been designed and verified to provide atmospheric turbulence-like conditions when the light propagates with a wavelength of 1550nm. The phase plate appears to be static, round, and transparent media with annular regions. The thickness of the phase plate is around 10mm. The photograph of a phase plate without the controlling system is shown in Fig. 2.1.

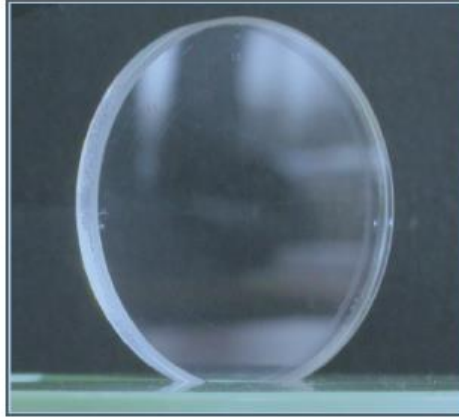


Figure 2. 1 Photograph of a pseudo random phase plate.

On the inside, it is composed of optical glass, acrylic, and a special near-index-matching (NIMTM) polymer, which provides them a solid mechanical structure. The principle of NIMTM is shown in Fig.2.2.

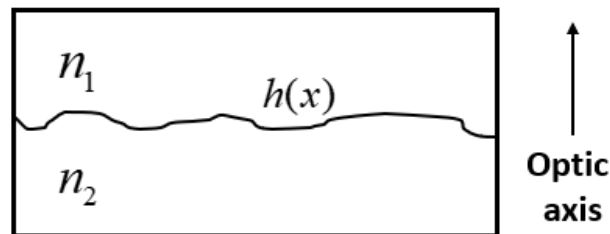


Figure 2.2 Principle of Near-Index-Match (NIMTM)

Two different materials of refractive indices n_1 and n_2 with an interfacial surface profile $h(x)$ provides an optical path difference (OPD) on an incident plane wave which is given by,

$$\begin{aligned} OPD(x) &= h(x)(n_1(\lambda) - n_2(\lambda)) \\ &= h(x)\Delta n(\lambda) \end{aligned} \quad (3.1)$$

For an index difference (n) of 0.02, a relief height of 50 is necessary to generate an OPD of 1. For extremely tiny n , the needed surface relief for appropriate OPD should be quite high when constructing such combinations. If n is sufficiently large, the precision of the machine tool will have an effect on OPD accuracy. In practice, an index difference of 0.02-0.06 works well for wavelengths 0.5-1.5 μm with maximum machine tool precision.

The inner structure of the PRPP consists of five layers: two outer layers of BK7 glass, two inner layers of near-index-matching polymer, and one layer of acrylic with the desired turbulence profile written on one side as seen in Fig.2.3. To create such a structure, the acrylic layer is machined with turbulence onto one surface first. After that, a layer of polymer is applied to either side of the acrylic, resulting in a near-index matching sandwich. Following that, the plate is sealed with optical window glass, which keeps the entire package together mechanically. An anti-reflective coating is then applied to the BK7 glass. The layer arrangement appears to be mechanically symmetric, which reduces the likelihood of external influences such as stress due to thermal expansion causing the PRPPs to split into their individual layers. Because of their design, the PRPPs are mechanically strong enough to be easily attached without distortion. The Starfire Optical Range designed the PRPPs, which were manufactured by Lexitek Corporation. These PRPPs were imprinted with Kolmogorov turbulence and a known Fried's parameter. This was accomplished by creating phase screens with standard Fourier transform techniques filtered with a Kolmogorov spectrum. One side of each phase screen featured 4096 sample phase points. The turbulence was inscribed on a 3.28" diameter acrylic annulus, with a 1.35" diameter obscuration, resulting in roughly 20 μm sample spacing. To aid with fabrication tolerances, two modes of tilt were deleted before machining the phase profile into acrylic. The PRPPs may be controlled and rotated at speeds ranging from 0.15625 rpm to 2470.2 rpm when installed on a specially constructed high speed rotary stage. A photograph of the PRPP mount is shown in Fig 2.4.

A PRPP's variable refractive index profile is only found in the annular area, and the entire phase plate is split into 4096 sample phase points. Fig 2.3 shows the diameters of several areas, as well as a portion illustrating the layers involved in the construction of a phase plate to the right of the picture.

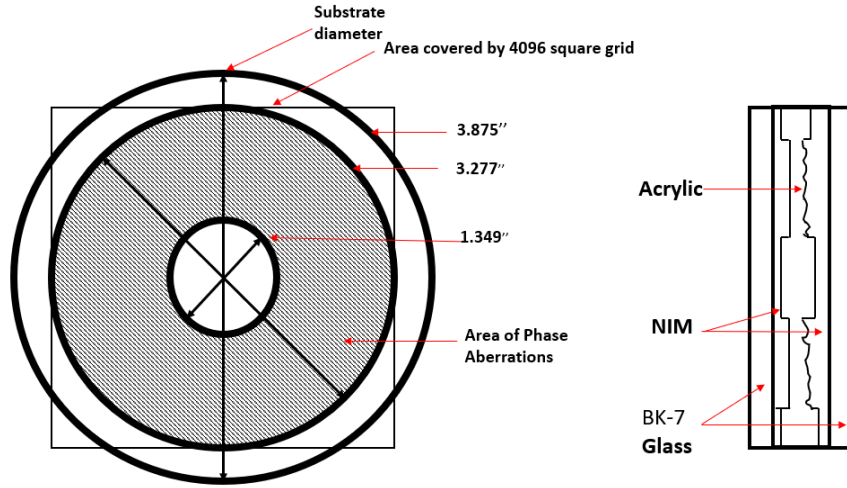


Figure 2. 3 Schematic representation of PRPP. Different layers are shown in the right. (Redrawn from the original figure. given by Lexitek [2])



Figure 2. 4 Photograph of a PRPP mount

There are many other available laboratory level atmospheric simulators like hot plates, hot air chambers, liquid filled chambers, air sprays, ion exchange phase screens and spatial light modulator(SLM) based turbulence generation methods. Each of these methods tries to implement Kolmogorov or non-Kolmogorov kind of turbulence. Every method comes with its own advantages and disadvantages. Some methods simulate the atmospheric turbulence regime more realistically, but the ease of implementation is compromised just like one of the recently reported turbulence simulator using two SLMs[39].

In general, the atmospheric simulator should create aberrated waves with temporal and spatial properties similar to air turbulence. For testing, it's ideal to have both spatial and temporal components to be controlled independently. For systems with a wide range of wavelengths, the simulator's spectral properties should match those of the actual atmospheric turbulence. The device should be compact, easy to create and employ, and not interfere with the functionality of other system components[40].

One of the widely used turbulence simulator comprises hot plates which replicates atmospheric processes and is simple to implement[41]. To achieve significant wavefront aberrations, a long passage through turbulence is required, as well as temperature differences of many degrees. This strategy may not be suitable for restricted space or if the device's heat interferes with surrounding optical components. Furthermore, the interdependence of temporal and spatial statistics may not be analogous to the atmosphere. There is a very similar approach in which a liquid is used instead of the hot air[42,43]. This approach reduces the need for long paths and large temperature gradients. But the presence of fluids can make assemblies heavier, increase the chance of leaks and the dependence of temporal and spatial statistics is still present. A well-modified design can mitigate some of the shortcomings of these techniques, but they do not provide controlled turbulence. They lack the ability to generate static phase profiles or repeatable turbulence sequences, as well as independent control over turbulence amplitude and speed.

Apart from these there are active optical elements like spatial light modulators which can produce turbulence in controllable fashion and provides independent control on spatial and temporal statistics[39,44–48]. However, these systems are more costly and complicated, with limited resolution due to actuator density. To accurately assess an adaptive optics system's performance, the actuator density for the turbulence generator should be higher than the corrective element density. Turbulence generators of this sort are unsuitable for advanced adaptive optics systems.

Static phase plates like PRPP are the most feasible way to simulate air turbulence for testing complex adaptive optics systems. Phase plates can be manufactured using several processes, including binary diffractive optics, moulded plastic optics, computer-generated holography, and near-index matching. A motorised assembly may replicate the temporal evolution of turbulence by moving a phase plate over a light path. These turbulence simulators have the same benefits as the active devices. Furthermore, phase plates have less severe resolution limits compared to active devices[40].

One problem with the use of PRPP as a turbulence simulator is that it is created with spatially uniform correlations but the real turbulence is spatially varying. However, since the phase plate is rotated during the experiments the spatial variation also comes into picture which realistically simulate the actual dynamic turbulence scenario. Moreover, out of the available laboratory level turbulence simulators, PRPP is the easiest and cheapest one to be implemented into any experimental geometry and the strength of the turbulence can be controlled just by altering the incident beam width and the speed of rotation.

2.2.2 Experimental scheme

Correlation studies have been extensively used in various fields of science. One approach to find the compatibility of CCD camera with a rotating PRPP is by considering autocorrelation of sequential images. This can be effectively employed to check the reliability of the detectors like CCD which we regularly use in our experiments. The continuous variation of autocorrelation ensures the right combination of experimental conditions and detector parameters. Fig. 2.5 shows the typical experimental geometry used to find the autocorrelation function. As shown in figure, a laser beam of 543 nm is spatially filtered using a spatial filter assembly (SFA) and then passed through a collimating lens L1 of focal length 100 mm for obtaining a perfect collimated beam. Then the beam is split in to two beams by a non-

polarizing cube beam splitter (BS1). The direct beam from the beam splitter falls on mirror M_1 and gets reflected to the second beam splitter (BS2). The other beam from BS1 is reflected by mirror M_2 and passes through the PRPP before reaching the second beam splitter (BS2). The beam splitter BS2 combines both the beams, and the interference pattern is recorded using a CCD (PCO Pixelfly usb). Neutral density filters (ND) are used to balance the intensity of the incoming beams for obtaining high contrast interference pattern. Initially, the interference is recorded without inserting the PRPP along one of the arms of Mach – Zehnder interferometer. Then the PRPP is inserted into the set up as shown in Fig. 2.5. The distance between the front plane of the PRPP, the imaging lens (L2) and CCD are kept at a distance $2f$ (where $f=100\text{mm}$ is the focal length of L2). This is to make sure that whatever phase fluctuations happen at the plane of PRPP is exactly reproduced at the detector plane with unit magnification and any effect of propagation is avoided. This experiment is repeated for different combinations of rotation speeds or movespeeds (MVS) of PRPP and FPS (frames per second) of CCD. Interference patterns for each one of these combinations have been recorded sequentially for further processing.

The interference at the plane of the detector is given by,

$$I(x, y) = I_1(x, y) + I_2(x, y) + 2I_1I_2 \cos(\theta(x, y)) \quad (3.2)$$

Here, $I_1(x, y)$ and $I_2(x, y)$ are respectively the object and reference beam intensities. Third term in Eq. (3.2) represents the interference term with θ being the phase term. Any change in the optical path of one of the beams will be detected by the phase term. Two sequential images recordings with and without inserting the PRPP will enable us to calculate the phase acquired exclusively due to the insertion of PRPP. In this experiment, the PRPP is fixed on to a rotary stage which can be driven using a computer-controlled stepper motor. This ensures the dynamic behaviour of the atmospheric turbulence. Rotation speed was changed from 1MVS to 100 MVS in steps of 10 and for each move speed data has been recorded for different frames per second settings of CCD (7fps, 12 fps, 15fps, 22fps, 27fps and 36fps). Different rotation speeds of PRPP correspond to different velocities. For a particular rotation speed, PRPP simulates a single layer of atmosphere with a fixed wind speed.

First, we find the phase term contribution without PRPP as Φ_{direct} then with PRPP as $\Phi_{\text{turbulence}}$. We employ Fourier fringe method to extract the phase information in both the cases [49]. Then phase fluctuation that arises exclusively due to PRPP, Φ_{prpp} , is given by,

$$\Phi_{\text{prpp}} = \Phi_{\text{turbulence}} - \Phi_{\text{direct}} \quad (3.3)$$

Obtained phase values are unwrapped using a 2D phase unwrapping algorithm. These unwrapped phase values are used for further correlation studies. Correlation coefficient, χ_k^1 , between temporally varying sequential images is given by,

$$\chi_k^1 = \frac{E[(A^1 - \mu^1)(A^k - \mu^k)]}{\sigma^1 \sigma^k} \quad (3.4)$$

Here, k corresponds to the index of the sequential images recorded and E represents the expectation value while μ and σ are mean and standard deviation respectively. It is explicit in the equation that images are always correlated with the first image to see time evolution. Using these correlation values, we propose a novel method to calculate the Fried parameter of PRPP.

Fried coherence length, r_0 , is the measure of the strength of atmospheric turbulence at a particular site. For a given structure constant profile, $C_n^2(z)$ the Fried coherence length is given by,

$$r_0 = [0.423 \sec \zeta \int_{\text{path}} C_n^2(z) dz]^{-3/5} \quad (3.5)$$

Where, z is the altitude and ζ is the zenith angle. Consider Fig. 2.6. PRPP is rotated in clockwise direction. At time $t=0$, a beam passes through the point A. Since the PRPP is rotating, after time t , beam now passes through a different part of the PRPP, say point B. Interference is recorded for the whole process. From the definition of Fried coherence length, it is evident that if the arc length AB is less than the Fried coherence length, phase of these interferograms will be strongly correlated. As the arc length increases there will be a gradual decrease in correlation and gets completely decorrelated once the arc length exceeds the Fried parameter. Hence it is proposed that this correlation coefficient can be effectively used to find the coherence length of any turbulence simulator.

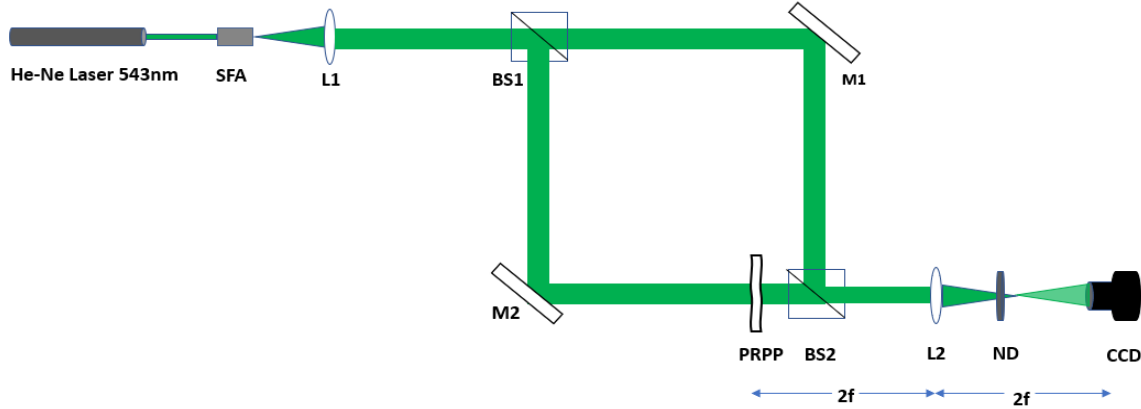


Figure. 2. 5 Schematic of experimental setup used for correlation measurements. SFA is spatial filter assembly. L1 is the collimating lens. BS1 and BS2 are two non-polarizing beam splitters. M1 and M2 represents two mirrors while PRPP is the pseudo random phase plate. L2 is the imaging lens. ND represents neutral density filters and CCD is the camera used.

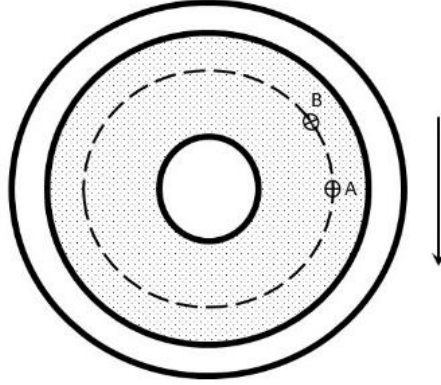


Figure. 2. 6 Clockwise rotation of PRPP

2.3 Results and Discussion

Using the experimental geometry shown in Fig. 2.5 first the interference patterns obtained without inserting the turbulent mimicking PRPP. Then PRPP is inserted in one of the arms of Mach-Zehnder interferometer. Interference fringes were recorded for different combinations of rotation speeds of PRPP and frames per second of CCD at the detector plane. Sequential images captured were processed and their corresponding phase values were calculated. Then a single point from the 2D phase map of sequential images was correlated. This was done for each combination of rotation speed of PRPP and each frame per second of CCD. This procedure was repeated for different points on the phase map. It was observed that only for a single combination of rotation speed of PRPP and FPS value of CCD, which is slowest rotation speed of PRPP (move speed one) and highest FPS (36 FPS), we get a correlation curve without any discontinuity. From Fig. 2.7 it is clear that even at the highest FPS of the CCD, for larger move speeds images become highly decorrelated even within a very short time span. This makes the further processing extremely difficult. Even when the movespeed is kept at 5MVS the corresponding autocorrelation curve is not very smooth. Hence, we limit our experimental scheme to a single combination of FPS and MVS, that is 36 FPS and 01 MVS. Fig. 2.8 shows the interference patterns observed for the experimental set up shown in Fig. 2.5 both before and after insertion of PRPP.

Sequential images captured with rotating PRPP at the lowest speed are shown in Fig. 2.9. Phase values of these images were found out using Fourier fringe method [12] and are shown in Fig. 2.10. When doing correlation measurements, it is not advisable to do it for the whole 2D phase map, hence we chose five different pixel positions, and their correlations were studied individually. Fig. 2.11 shows phase map of a single frame with chosen points.

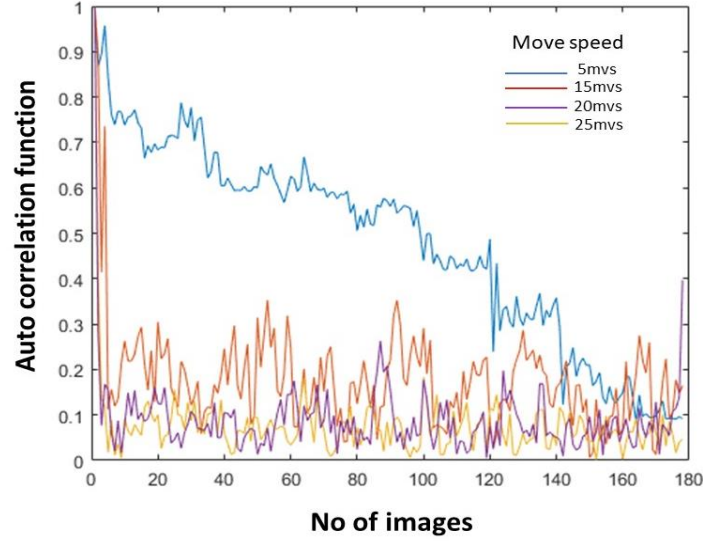


Figure. 2. 7 Autocorrelation coefficient corresponding to different movespeeds for 36 FPS.

From figure 2.11 it can be seen that the line connecting the positions of the chosen points are normal to the direction of the fringe movement. If we choose five points along the direction of the fringe movement, essentially, we will be doing the correlation studies of the temporally shifted copy of the same point. Hence, the choice of the points as shown in Fig. 2.11 ensures that the averaging is done for the points corresponding to the five different regions in the phase map.

Fig. 2.12 shows the normalised autocorrelation coefficient vs distance moved. Unwrapped phase of these points follows an exponential trend. It can be seen in Fig. 2.12 that, as the PRPP rotates correlation gradually decreases and once it moves beyond a certain length, it becomes completely decorrelated. It is proposed that half width half maximum (HWHM) of this autocorrelation curve gives an estimate of the Fried coherence length. Rotation speed of PRPP for each move speed (MVS) is calculated by measuring the time taken for a complete rotation and the distance travelled. (Refer to Fig. 2.6. Circumference of the dotted circle gives the distance travelled). For the lowest move speed, rotation speed was found to be 0.43 m/s. This rotation speed multiplied with the width of autocorrelation curve gives Fried coherence length. For each of the five points we found the width of the autocorrelation curve and corresponding Fried parameters are listed in table 1. Average r_0 is calculated to be 316.95 μm which closely agrees with the value given by the manufacturers, i.e., is 300 μm .

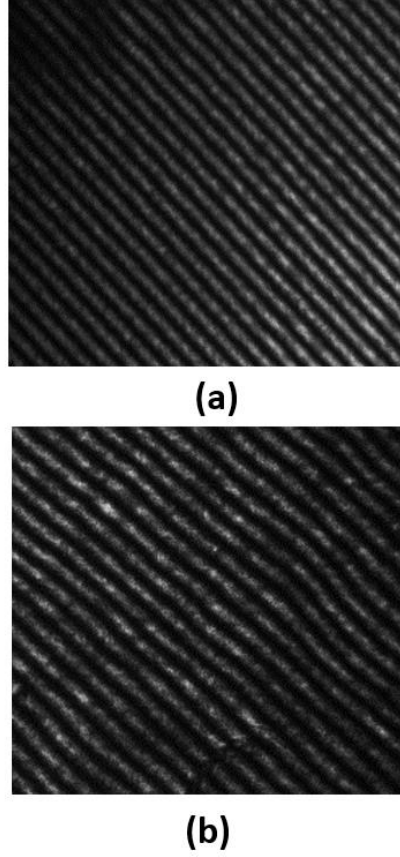


Figure. 2. 8(a) is the image captured at CCD before inserting PRPP. (b) shows the distorted pattern after inserting PRPP into the set up.

2.3.1 Calculation of percentage error and probable sources of errors

The average calculated value of Fried coherence length differs from the value provided by the manufacturers with a percentage error of just 5.34%. Even though it is an insignificant error, it can be seen in table 1 that two points A and E suffer a larger variation. The presence of above-mentioned errors could be attributed to the fundamental assumptions made during the theoretical formalism. In Fig. 2.6 we assumed the incident beam to be a point, however in the actual case there is a finite beam width. Hence, the linear velocity we calculated for the center might not be applicable to the points corresponding to the points on the outer edge of the beam. Another important factor to be mentioned is that manufacturers claim to have imprinted Kolmogorov kind of turbulence for when the incident beam has a wavelength of 1500 nm. However, there could be slight departure from such behavior once we change the wavelength. One of the limitations of the current procedure is that we consider phasescreen as a single layer. However, that is not the case in the actual set up. The PRPP has a thickness of 2 mm. Deviation of calculated Fried parameter from the actual value could be attributed to the combined effect of all these.

Hence, our proposed method proves to be an easy and effective method to find out the coherence length of PRPP. This method can be extended to any kind of turbulence since we do the correlation only from the recorded interferogram. Unlike other direct measurements of coherence length this does not require any complicated experimental set up and still yields reliable values. Fried coherence length of any type of turbulence can be calculated for any wavelength just by changing the source of required wavelength.

2.3.2 Comparison of the proposed scheme with the previously reported methods.

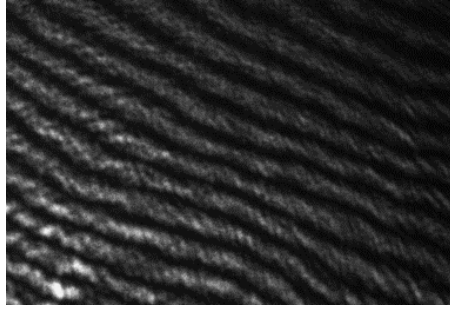
One can find many methods in literature to find the Fried parameter for actual atmospheric conditions. To the best of our knowledge, however, there are only a few methods reported for the estimation of Fried parameter in the laboratory level. One such method reported by A. Dixit et al [1] makes use of the angle of arrival fluctuations measurements for the calculation of Fried parameter of a transmissive random phase screen. Their experimental results show an excellent agreement with the theoretical values and error bar is negligible. But the use of a MATLAB based high-speed video processing method in their proposed scheme makes it a bit difficult to perform.

Jun Zhang et al [11] also use angle of arrival measurements for the calculation of Fried parameter of a convective tank. Their experimental results also show good match with the theoretical values in the moderate turbulence regime with a percentage error close to 18.

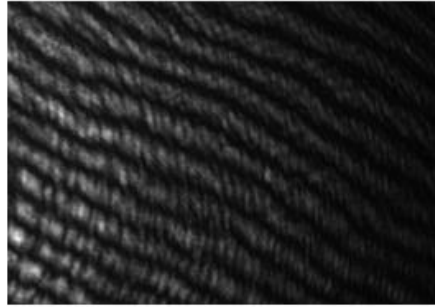
Another method successfully demonstrated by Horst S et al [11] follows a similar experimental scheme proposed in this chapter to calculate the Fried parameter of a PRPP. They make use of a digital holographic scheme to calculate complex coherence factors and along with an image sharpening algorithm for the estimation of Fried parameter. While in this chapter we employed the autocorrelation of the distorted sequential images captured using CCD, they took an average of the distorted images, and a spatial correlation method has been employed. This averaging eventually removes the effect of the rotation of the PRPP. In that case our method, it considers a dynamic turbulence regime, outdoes the former. Also, while considering the accuracy of the estimations our scheme outperforms the other one. The maximum error reported in our method is 14% while that of the digital holographic scheme is 52%.

2.3.3 Limitations of the proposed scheme.

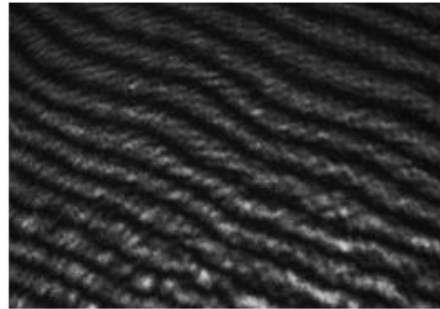
Even though our reported method is experimentally verified it suffers some limitations mainly due to the fundamental assumptions made with the theoretical formalism. One important point is the assumption of point source in Fig. 2.6. But a perfect point source is impossible to achieve in a practical scenario. Another major concern is the compatibility of CCD and the rotating PRPP. As depicted in Fig. 2.7, for higher rotation speeds of the PRPP autocorrelation estimation and further phase value calculation becomes difficult to perform. Hence, we need to limit our experimental scheme for the lowest rotation speed of PRPP. It has to be mentioned that this limitation cannot be eliminated by the use of high-speed sensors. That is because we employ the Fourier fringe method for the estimation of phase values, and it is assumed that fringes are nearly parallel. For higher turbulence strengths we might have to use another phase estimation algorithm which is not restricted by such assumptions.



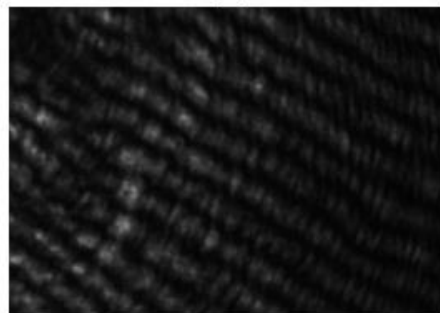
(a)



(b)



(c)



(d)

Figure. 2. 9 (a) to (d) represent the sequential images captured with rotating PRPP.

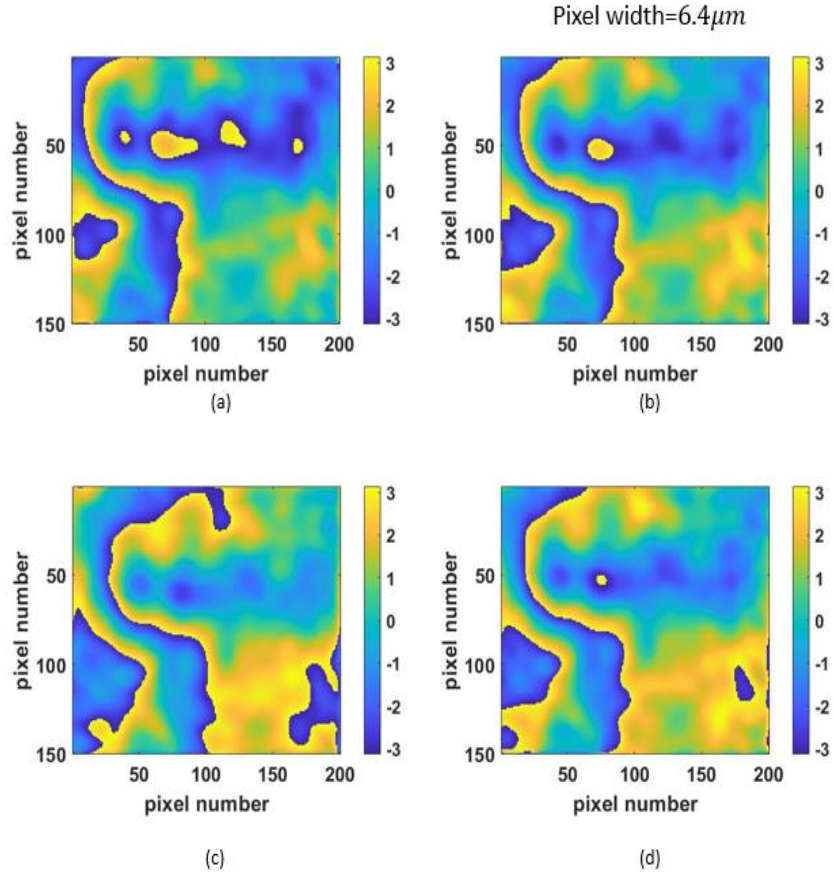


Figure. 2. 10 (a) to (d) represent the phase map of sequential images.

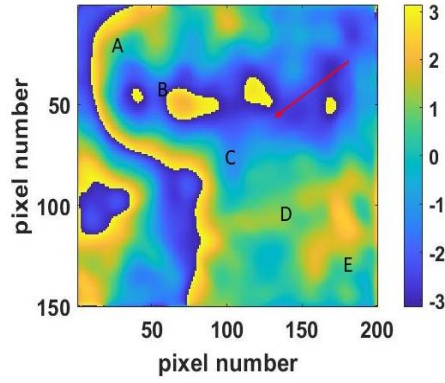


Figure. 2. 11 shows the phase map with five chosen points A, B, C, D and E for correlation measurements. Red arrow shows the direction of the fringe movement due to the rotation of PRPP.

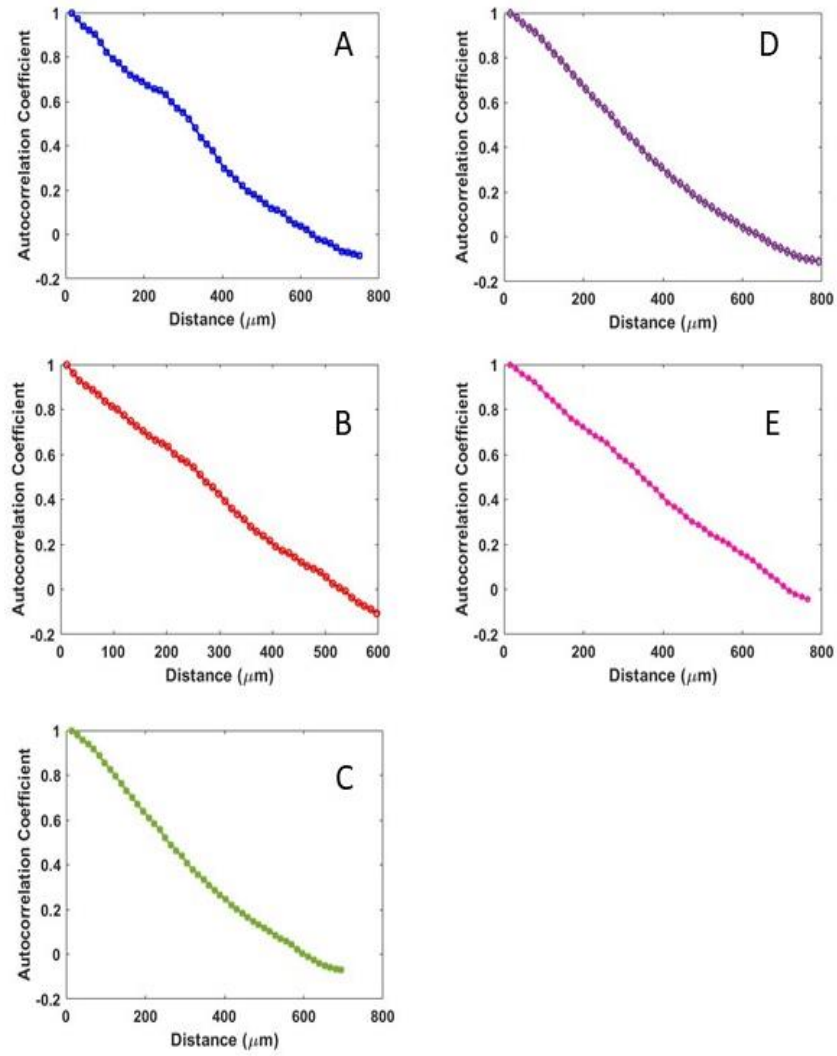


Figure. 2. 12 Autocorrelation for five different points for the sequential images captured. A, B, C, D, and E correspond to the points shown in Fig. 2.11.

Table 2. 1 Fried coherence length estimated for different points.

Points	Fried parameter (r_0 in μm)	Percentage error (%)
A	330.10	9.09
B	290.21	3.37
C	302.11	0.66
D	314.32	4.55
E	348.01	13.79

2.4 Conclusion

By doing autocorrelation calculations compatibility between rotating phase plate and CCD was established. PRPP has been quantitatively characterised for Fried coherence length. A novel method to estimate Fried coherence length has been presented. Using autocorrelation measurements average Fried parameter of rotating phase plate is found to be $316.95\text{ }\mu\text{m}$.

CHAPTER 3

INSENSITIVITY OF PARTIALLY COHERENT GAUSSIAN-SCHELL MODEL BEAMS TO THE IMPACT OF DYNAMIC KOLMOGOROV TYPE TURBULENCE.

3.1 Introduction

The resilience of partially coherent beams to the effect of turbulence has been analytically proven and experimentally verified[5,50–54] . A partially coherent beam carries its energy in multiple spatial modes, which are mutually incoherent. Each of these modes produces a distinct interference pattern on the receiver after passing through turbulence. Since these modes are mutually incoherent their interference patterns add only by intensity. This results in a more uniform intensity pattern at the receiver [55]. One can find rich literature on this topic and Gbur wrote an extensive review article on the same[1].

One important class of partially coherent beams is the Gaussian-Schell model beam (GSM beam). Its beam properties for free-space communications have been extensively studied and a considerable reduction in scintillation index is observed [29,56]. But this is achieved at the cost of reduced energy at the receiver because of the larger angular spread and beam wander. One can look for a tradeoff between these effects, however analytically optimizing the beam parameters would be quite a task. Schulz used a variational and iterative method for the optimization of GSM beams[57,58] . But we still do not know how to physically achieve such optimal beams for actual communications systems.

In this chapter, we simulated Gaussian Schell model beams in different coherence regimes using a complex screen method (CS method) [59]and a recently reported phase and intensity method (PI method) [27]. The simulated beams are then separately passed through a dynamic (rotating) pseudo-random phase plate mimicking Kolmogorov type turbulence [31,32] with the aid of a spatial light modulator. These turbulence-impacted beams are finally observed through a CCD camera and a wavefront sensor to calculate scintillation index, beam wandering, and Zernike coefficients. We investigated the effect of coherence on these results by changing the correlation width of the random field in our simulations [46,47]. There are two different experimental geometry used for our investigations. One includes a single passage through the turbulence phase screen while the other includes a double passage. We chose these geometries because they respectively resemble ground to ground (horizontal), and ground to space to ground (vertical) communication channels. For each of the simulated Gaussian Schell models beams, we investigated how the coherence length of input beams affects the scintillation index, beam wandering, and Zernike modes. It has been repeated for both single passage and double passage.

3.2 Theoretical background and simulations.

3.2.1 Simulation¹

There are many methods to create the GSM beams[60–66]. However, we limit our analysis to the simulation scheme designed recently as the previous methods concentrate on creating optical field realisations whose ensemble-averaged autocorrelation corresponds to a certain second-order field moment known as the cross-spectral density function. Because optical field realisations are supposed to follow Gaussian statistics, these approaches ignore the irradiance moments, which, according to the Gaussian moment theorem, are entirely governed by the field's first and second moments. This scheme extends previous synthesis methodologies by providing control over irradiance statistics (in addition to the CSD function), allowing for the design, modelling, and simulation of novel partially coherent beams with non-Gaussian field realisations as well.[27].

Here we use two different simulation methods to generate Gaussian Schell model beams. One is a commonly used complex screen method (we call it the CS method) and the other one is the phase and intensity method (called PI method). The PI method includes the independent control of both the phase and amplitude statistics of the random field[27].

3.3 Experimental Procedure

3.3.1 Single passage

Two different experiment schemes were employed to study the effect of coherence and simulation methods on the turbulence impacted beam. In the first experimental scheme, light from a He-Ne laser of wavelength 633nm is allowed to pass through an atmospheric turbulence simulator only once. This experimental scheme is similar to ground-to-ground (horizontal) communication. Fig. 3.1 shows the experimental geometry where a laser beam is spatially filtered and collimated using a lens L of focal length 50mm. The collimated laser beam further passes through a polarizer and falls on the spatial light modulator (SLM). The SLM used in the experiment is Holoeye PLUTO phase-only SLM based on reflective LCOS micro-displays with a resolution of 1920×1080 pixels and pixel size of 8 μ m. It is optimized for different wavelength ranges (420-1700 nm). Phase profiles of simulated GSM beams are fed onto the SLM one at a time. The reflected beam from SLM then passes through an aperture and a mirror. Here the aperture is used to select first-order diffraction order. The mirror reflects this beam towards a pseudo-random phase plate which is the atmospheric turbulence simulator. After passing through the PRPP the beam further gets split by a beamsplitter BS to reach the CCD camera (Charge Coupled Device, PCO pixelfly USB) and a Shack-Hartmann wavefront sensor simultaneously for detection. CCD and SHWFS are kept at an equal distance from the beamsplitter. The distance is chosen to be 50cms such that the effect of propagation also comes into the picture. To create a dynamic turbulence effect, PRPP, which is fixed on a rotary stage, is rotated using a stepper motor with the aid of LabVIEW software. However, the speed of PRPP is kept at the lowest value so that CCD and SHWFS see PRPP stationary at a particular instance. In order to synchronize the CCD with the SLM we used an external trigger function with a function generator (Tektronics-AFG3022B).

¹ A detailed description of the simulation algorithm can be found at [27]

Phase maps of GSM beams via CS and PI methods are loaded onto SLM for different coherence lengths. For each phase map, turbulence impacted beams are viewed with CCD and SHWFS. 1000 images are sequentially captured using CCD and ten sample spot fields are captured using SHWFS for each phase map.

3.3.2 Double passage

Double passage geometry which resembles to ground to space to a ground communication system is shown in Fig. 3.2. The beam reflected from SLM passes through an aperture and a mirror. The mirror reflects this beam towards a beamsplitter. One half of the beam is blocked using a black screen and the other half passes through the PRPP. Mirror M2 reflects this beam again towards the PRPP and thus double passage through turbulence is ensured. Turbulence impacted beam is then viewed using CCD and SHWFS placed equidistant from the beamsplitter BS2. The distance is again chosen to be 50cms such that the effect of propagation also comes into the picture. Just like in single passage geometry, phase maps of GSM beams via CS and PI methods are loaded onto SLM for different coherence lengths. For each phase map, turbulence impacted beams are viewed with CCD and SHWFS. 1000 images are sequentially captured using CCD ten instances are captured using SHWFS for each of the phase map. The rest of the experimental conditions are similar to the single passage scheme.

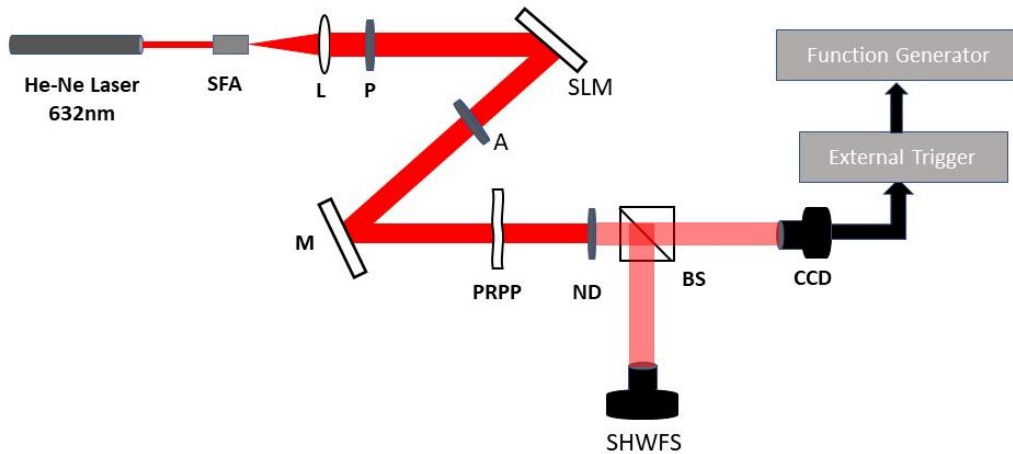


Figure 3. 1 shows the experimental setup for single passage geometry. SFA is spatial filter assembly and L is the collimating lens. SLM denotes spatial light modulator. A is an aperture and M denotes a mirror. PRPP is the pseudo random phase plate, ND denotes neutral density filter while BS is a beamsplitter. CCD and SHWFS are respectively the camera and Shack Hartmann wavefront sensor.

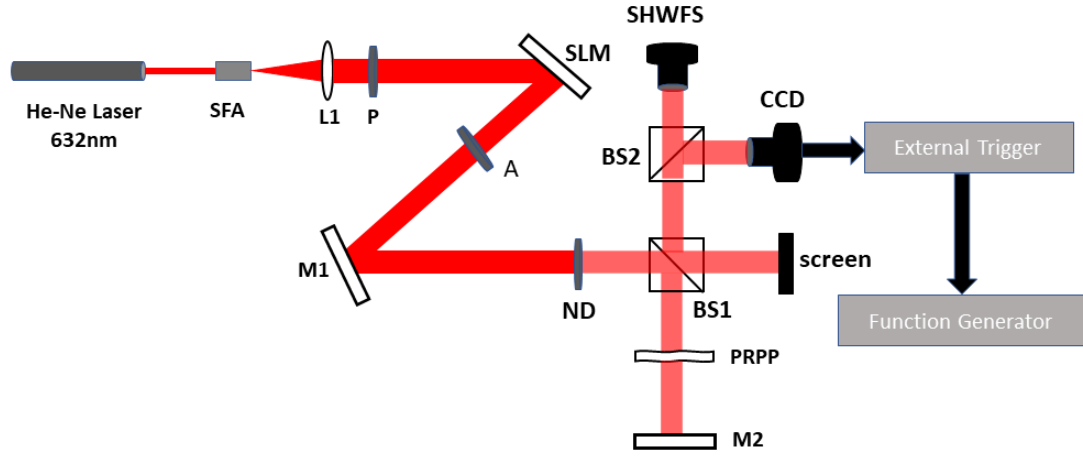


Figure. 3. 2 shows the experimental setup for double passage geometry. SFA is spatial filter assembly and L is the collimating lens. SLM denotes spatial light modulator. A is an aperture, M denotes a mirror and ND is a neutral density filter. PRPP is the pseudo-random phase plate, BS is a beamsplitter CCD is the camera used and SHWFS denotes a Shack-Hartmann wavefront sensor.

3.4 Results and Discussion

3.4.1 GSM beams simulated using CS and PI methods.

A few instances of phase and amplitude of GSM beams simulated using CS and PI methods are shown in Fig. 3.3. It is clear from the figure that phase maps of GSM fields simulated via two techniques are different and the difference becomes conspicuous as the coherence length increases.

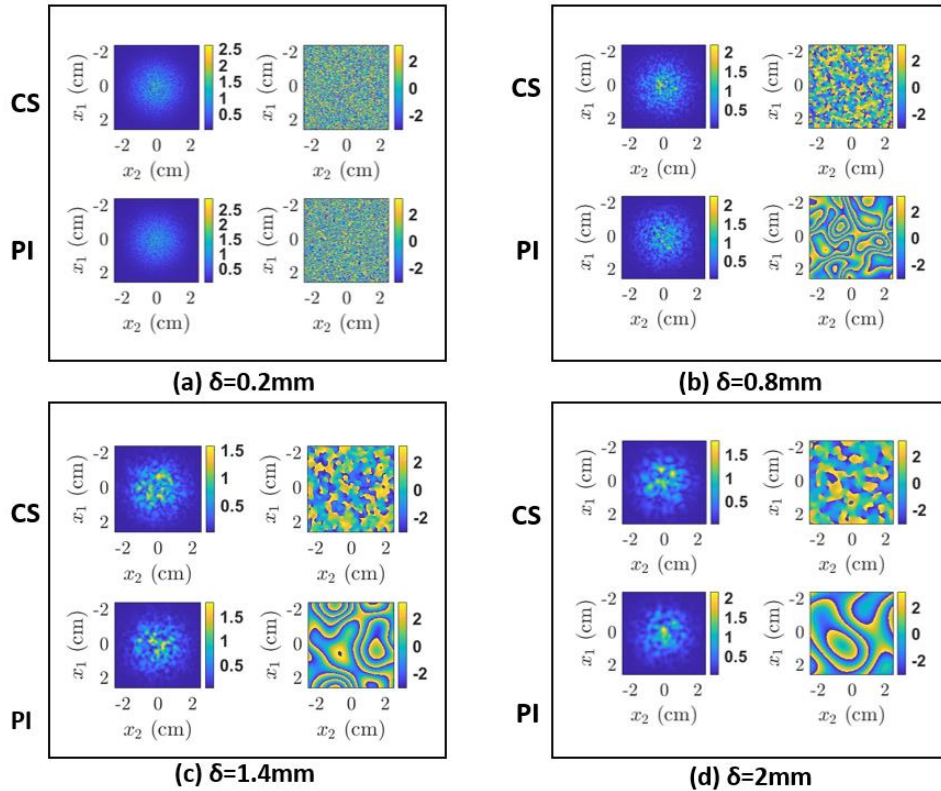


Figure. 3. 3 shows the amplitude and phase of simulated Gaussian Schell model beams for $\delta = 0.2\text{mm}$, 0.8mm , 1.4mm , and 2mm respectively. The phase values are in radians.

3.4.2 Experimental observations

A few examples of images captured using CCD are shown in Fig. 3.4 and Fig 3.5. Images viewed through CCD are markedly different from each other for the different experimental schemes employed. The effect of stronger turbulence can be seen in Fig. 3.5.

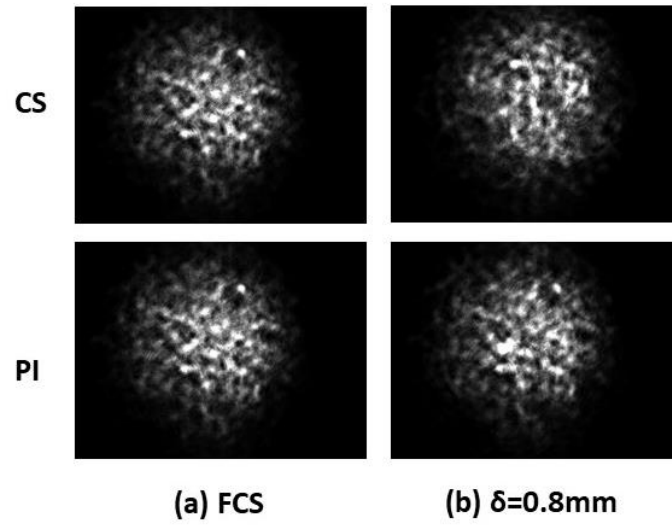


Figure. 3. 4 shows the images of turbulence impacted beam for single passage geometry. Beams corresponding to both CS and PI methods are shown. FCS means a fully coherent source.

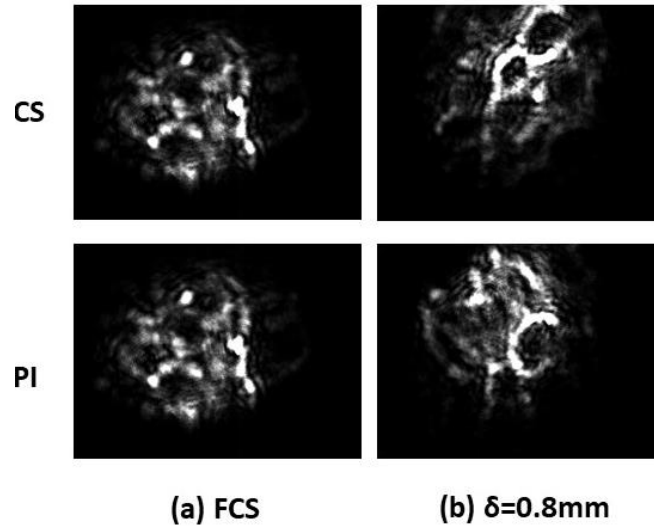


Figure. 3. 5 shows the images of turbulence impacted beam for double passage geometry. Beams corresponding to both CS and PI methods are shown. FCS means a fully coherent source.

3.4.3 Scintillation index

The intensity of a light beam changes when it travels through air turbulence, and scintillation of a light beam correlates to these intensity variations. The major source of scintillation is refractive index changes in the turbulent environment.

Consider one turbulent layer that operates as a random-phase screen, with a thickness δh selected to be substantial in comparison to the correlation scale of the inhomogeneities but small enough for diffraction effects across the distance δh (thin screen approximation). The layer input is $U_h(r) = 1$, and the output complex field after traversing the layer of thickness δh is [67],

$$U_{h+\delta h}(r) = e^{i\phi(r)} \quad (3.6)$$

where $\phi(r)$ is the phase variation produced by random fluctuations in the index of refraction $n(r, h)$ given by,

$$\phi(r) = k \int_h^{h+\delta h} n(r, z) dz \quad (3.7)$$

Where k is the wave number.

The small perturbation approximation is used to characterize optical path variations (usually valid for vertical pathways with zenith angles less than 60degrees). The phase variation generated by a "thin" layer is assumed to be very modest in comparison to unity such that,

$$\phi(r) \ll 1 \quad (3.8)$$

Then the field at the output layer is given by,

$$U_h(r) = 1 + i\phi(r) \quad (3.9)$$

The complex field at the ground is a result of a free propagation, and is given by,

$$U_0(r) = 1 + i\phi(r) * \frac{1}{i\lambda h} \exp\left[\frac{i\pi r^2}{\lambda h}\right] \quad (3.10)$$

If we define a complex quantity $\varepsilon(r)$ such that,

$$\varepsilon(r) = \phi(r) * \frac{1}{\lambda h} \exp\left[\frac{i\pi r^2}{\lambda h}\right] \quad (3.11)$$

Then the complex field at the ground becomes,

$$U_0(r) = 1 + \varepsilon(r) \quad (3.12)$$

Where ε defines the relative variations of the complex amplitude at the ground caused by the layer at height h . Its real component shows the relative fluctuations of the modulus, and

similarly its imaginary component describes the relative fluctuations of the phase. The real and imaginary parts are respectively given by,

$$\chi(r) = \phi(r) * \frac{1}{\lambda h} \cos\left(\frac{\pi r^2}{\lambda h}\right) \quad (3.13)$$

$$\varphi(r) = \phi(r) * \frac{1}{\lambda h} \sin\left(\frac{\pi r^2}{\lambda h}\right) \quad (3.14)$$

The complex amplitude at the ground in terms of $\chi(r)$ and $\varphi(r)$ is given by,

$$U_0(r) = 1 + \chi(r) + i\varphi(r) \quad (3.15)$$

Then the intensity becomes,

$$I(r) = |U_0(r)|^2 \simeq 1 + 2\chi(r) \quad (3.16)$$

The term $2\chi(r)$ describes the intensity's relative variations. The "amount" of scintillation, or the scintillation index σ_I^2 , is the simplest variable to quantify. It is defined as the variance of the relative irradiance (Intensity I) variations given by,

$$\sigma_I^2 = \frac{\langle I^2 \rangle - \langle I \rangle^2}{\langle I \rangle^2} \quad (3.17)$$

Where the angular bracket represents the ensemble average.

3.4.3.1 Calculation of scintillation index

In order to measure the scintillation index 1000 images have been captured using CCD. Each of these images is saved in MATLAB as matrix, $I_n(x, y)$. Here, I_n , represents the intensity value at each point and n corresponds to each realisation. Its value varies from 1 to 1000. x and y are pixel spatial coordinates. Coordinates of the centroid (\bar{x}_n, \bar{y}_n) for each frame is given by[30],

$$\bar{x}_n = \frac{\sum_i \sum_j x_i I_n(x_i, y_j)}{\sum_i \sum_j I_n(x_i, y_j)} \quad (3.18)$$

$$\bar{y}_n = \frac{\sum_i \sum_j y_i I_n(x_i, y_j)}{\sum_i \sum_j I_n(x_i, y_j)} \quad (3.19)$$

Let the intensity at the centroid of each frame be, $I_n(\bar{x}, \bar{y})$, N be the total number of frames then average intensity for each frame at the centroid will be,

$$\bar{I} = \frac{\sum I_n(\bar{x}_n, \bar{y}_n)}{N} \quad (3.20)$$

Then scintillation index at the centroid position is given by,

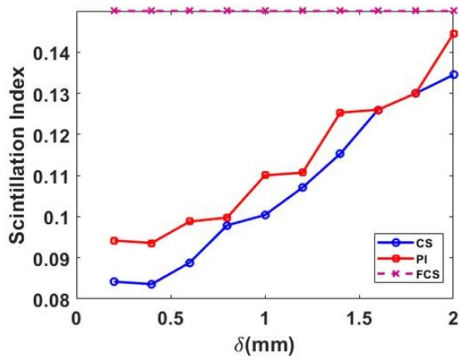
$$\sigma_{I_c}^2 = \sum \frac{I_n^2(\bar{x}_n, \bar{y}_n)}{N\bar{I}^2} - 1 \quad (3.21)$$

Fig. 3.6 sums up the scintillation index data obtained for GSM beams of different coherence lengths. From Fig. 3.6(a) it is clear that the scintillation index corresponding to partially coherent beams is considerably lower than that of their fully coherent counterpart. Scintillation corresponding to a fully coherent source is 0.15. A percentage reduction of 43.8 is obtained for GSM beam simulated via CS method for $\delta = 0.2mm$. The maximum percentage reduction of 37.2 is obtained for GSM beam simulated via PI method again at $\delta = 0.2mm$. For single passage geometry scintillation values follow a trend that is similar for both CS and PI beams of varying coherence lengths. In both the cases scintillation index increases as we increase the value of δ however reduction in scintillation is more for GSM beams simulated via the CS method. These results are presented in Table 3.1.

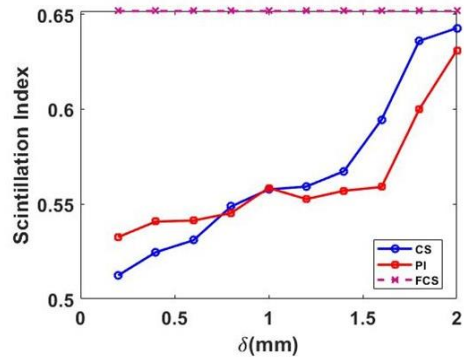
It can be clearly seen in Fig. 3.6(b) the scintillation values corresponding to GSM beams are less compared to their fully coherent counterparts even for stronger turbulence. Scintillation corresponding to a fully coherent source is 0.65. Percentage reduction of 21.37 and 18.27 are respectively observed for GSM beams simulated via CS and PI methods for $\delta = 0.2mm$. Here also scintillation index value increases as we increase the coherence length.

Table 3. 1 Percentage reduction in scintillation index from the value corresponding to a fully coherent source.

δ (mm)	Single Passage		Double Passage	
	CS	PI	CS	PI
0.2	43.87	37.20	21.37	18.28
0.4	44.27	37.60	19.50	17.02
0.6	40.80	34.13	18.53	16.94
0.8	34.73	33.47	15.80	16.33
1.0	33.06	26.64	14.42	14.30
1.2	28..6	26.19	14.19	15.20
1.4	23.13	16.46	12.95	14.53
1.6	16.13	16.00	08.78	14.22
1.8	14.00	13.33	02.41	07.95
2.0	10.33	03.67	01.38	03.18

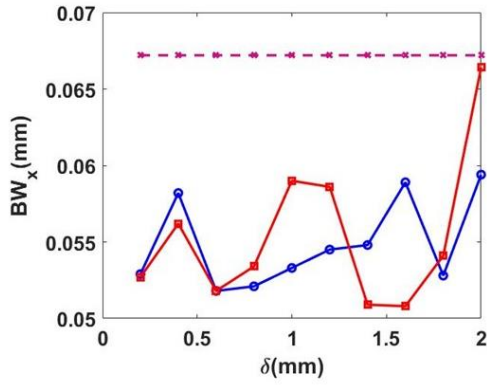


(a) single passage

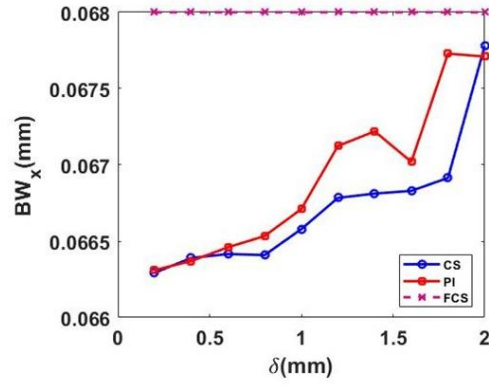


(b) double passage

Figure. 3. 6 Scintillation index corresponding to the single passage and the double passage.

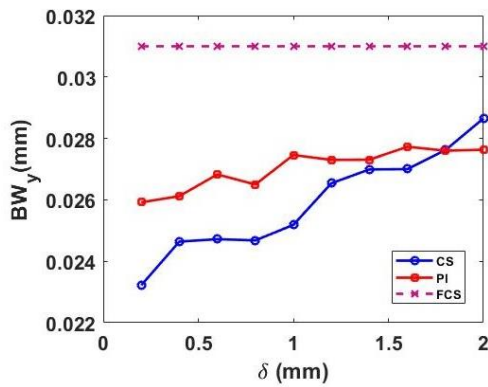


(a) Single passage

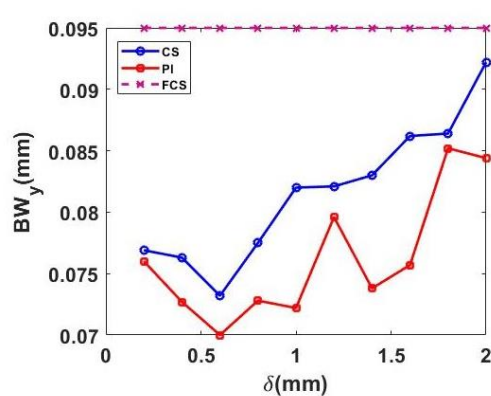


(b) Double passage

Figure. 3. 7 Beam wander in the x-direction corresponding to the single passage and double passage schemes. FCS means a fully coherent source.



(a) Single passage



(b) Double passage

Figure. 3. 8 Beam wander in the y-direction corresponding to the single passage and the double passage schemes. FCS means a fully coherent source.

3.4.4 Beam wandering calculations.

A beam moving along a certain direction might get deflected from its original path after passing through turbulence. This effect is manifested as the random deflections of the centroid at the detector plane. If the beam passes along the z-direction, beam wander along x and y directions are given by [2],

$$\langle \hat{x} \rangle = dx = \frac{\sum (x - \bar{x}_n) I}{\sum I} \quad (3.22)$$

$$\langle \hat{y} \rangle = dy = \frac{\sum (y - \bar{y}_n) I}{\sum I} \quad (3.23)$$

Fig. 3.7(a) shows the beam wandering along the x-direction for the single passage scheme. This beam wander hinders the quality of data transmission. Beam wandering along the y-direction is depicted in Fig. 3.8(a). It is evident that partially coherent beams suffer less beam wander compared to fully coherent Gaussian beams. In general beam wander increases as the coherence length increases. Percentage reduction in beam wander is given in table 3.2. Fig. 3.7(b) and Fig.3.8(b) show the beam wander for the double passage scheme. Again, it is obvious from the figure that partially coherent beams suffer less beam wander in the x and y directions compared to fully coherent Gaussian beam. A significant reduction is observed for both the beams simulated via CS and PI methods and the corresponding percentage variation is given in table 3.2.

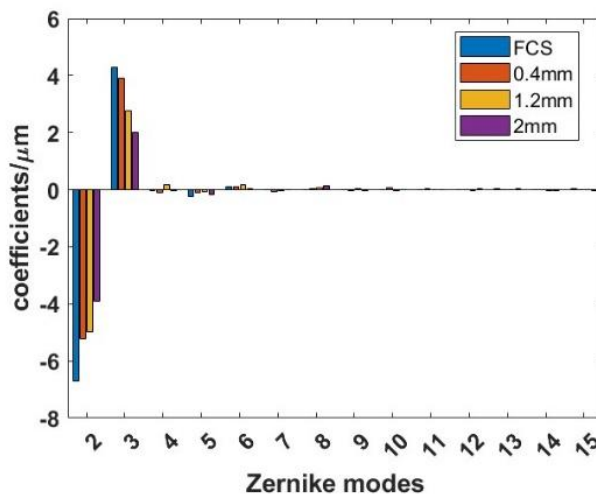
Table 3. 2 Percentage reduction in beam wander from the value corresponding to a fully coherent source.

δ (mm)	Beam wander in x direction				Beam wander in y direction			
	Single Passage		Double Passage		Single Passage		Double Passage	
	CS	PI	CS	PI	CS	PI	CS	PI
0.2	21.29	21.58	2.51	2.49	19.05	20.00	25.09	16.38
0.4	13.39	16.36	2.36	2.40	19.68	23.47	20.52	15.74
0.6	22.92	22.91	2.32	2.26	22.94	26.31	20.25	13.45
0.8	22.47	20.53	2.33	2.16	18.42	23.36	20.38	14.51
1.0	20.68	12.20	2.08	1.90	13.68	24.00	18.75	11.41
1.2	18.89	12.79	1.78	1.29	13.57	16.21	14.38	11.93
1.4	18.45	24.25	1.74	1.15	12.63	22.31	12.93	11.91
1.6	12.35	24.04	1.72	1.44	9.26	20.31	12.90	10.54
1.8	21.42	19.49	1.59	0.40	9.05	10.31	10.90	10.96
2.0	11.60	01.17	0.33	0.43	2.94	11.15	07.58	10.86

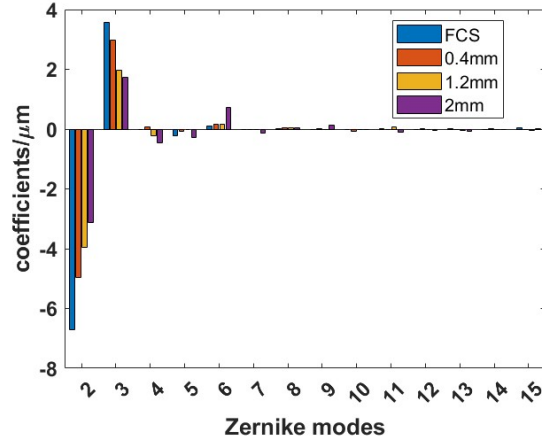
3.4.5 Zernike coefficients evaluation.

The phase of a non-singular optical beam can be conveniently expressed in terms of Zernike polynomials [2]. Each term in such an expression corresponds to a particular kind of aberration present in the wavefront. Some lower-order Zernike modes correspond to aberrations like piston, coma, and astigmatism. We used a Shack-Hartmann wavefront sensor (SHWFS) to find out the Zernike coefficients. The SHWFS is purchased from Thorlabs (WFS 150-5C). It has a lenslet array with each lenslet of $150\mu\text{m}$ diameter and pixels in that domain are 31×31 where each pixel size is $4.6\mu\text{m}$. The spot intensity measurement in each domain is done by calculating the summation of intensity over all pixels present in that domain.

Zernike modes except piston are plotted in Fig.3.9 for the single passage. It is evident that the lower order aberrations values are different for coherent and GSM beams, however values corresponding to higher-order modes tend to converge. Zernike coefficients are larger for GSM beams with $\delta = 2\text{mm}$. Similarly, Zernike modes except piston for the double passage scheme are plotted in Fig. 3.10. It is evident from these figures that lower-order aberrations are larger for fully coherent beams while values of higher-order aberrations converge. Zernike values tend to match for both CS and PI methods. Clearly, values Zernike coefficients are larger for double passage geometry.

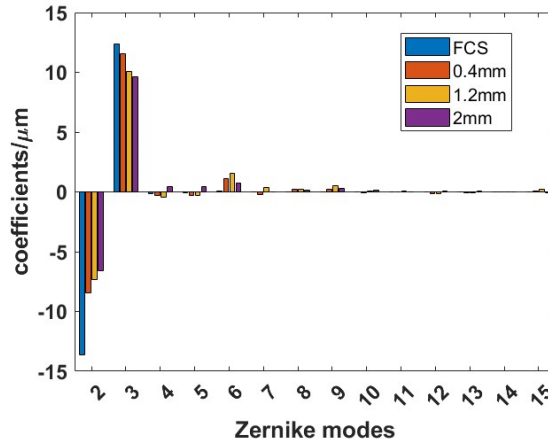


(a) single passage (CS)

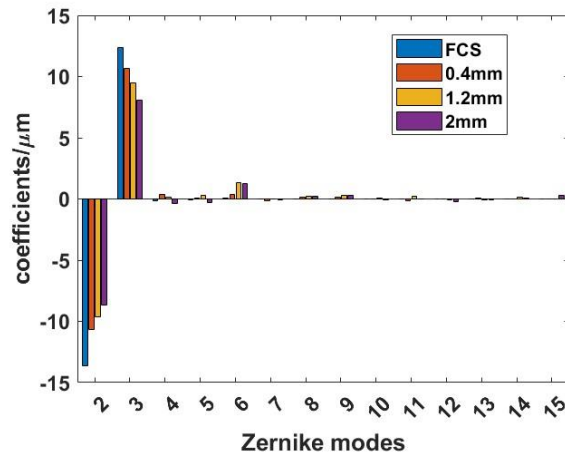


(b) single passage (PI)

Figure. 3. 9 Zernike polynomials corresponding to single passage geometry for both CS and PI beams. FCS means a fully coherent source.



(a) double passage (CS)



(b) double passage (PI)

Figure. 3. 10 Zernike polynomials corresponding to double passage geometry for both CS and PI beams. FCS means a fully coherent source.

3.5 Conclusion

In this chapter, we have simulated Gaussian Schell model beams using two different algorithms. Simulated beams with gradually varying coherence lengths were passed through a dynamic transmissive Kolmogorov turbulence simulator in two different experimental schemes. Scintillation index, beam wander and Zernike polynomials were calculated for all varied experimental conditions. It can be concluded that partially coherent beams are a better choice for free space optical communications. It is observed that the resilience of partially coherent beams is more under weaker turbulence.

CHAPTER 4

THE RESILIENCE OF ZERO ORDER BESSEL-GAUSSIAN BEAMS TO THE IMPACT OF DYNAMIC KOLMOGOROV TYPE OF TURBULENCE.

4.1 Introduction

In the case of free space optical communication systems, intensity fluctuations lead to an increase in the link error probability which will in turn reduce the overall performance[68]. However, in such wireless communication systems we have the freedom to choose the beam that we want to transmit. Many attempts have been made to optimize the transmitting beams to improve communication efficiency. One can find rich literature in this regard. Optimization of transmitting beams consists of many methods like altering their degree of coherence, and degree of polarization, or using different classes of beam shapes[5,50–53,55,69,70].

One important class of beams which has the potential to be used in free-space optical communication systems is Bessel beams[71,72]. Bessel beam corresponds to an exact, propagation invariant solution to the Helmholtz equation [71]. Bessel beams which propagate along the z-direction can be thought as a superposition of infinitely many plane waves whose wave vectors form a cone around the z-axis. These plane waves interfere and thus yields a propagation invariant transverse field distribution which is given by the Bessel function of the first kind. These beams are peculiar because of their non-diffracting property around opaque objects.

An ideal Bessel beam contains an infinite amount of energy which is impossible to achieve. Hence in practical scenario we truncate the Bessel beam at some radius. If we use Gaussian truncation, we get Bessel-Gaussian beams (BG beams) [73]. Because of this truncation again the problem of diffraction arises. However, the effect of diffraction can be minimised if we keep the propagation distance smaller than the corresponding diffraction length of the BG beam. Since the effect of diffraction on BG beam is initially seen in outer rings and sequentially progresses to the central region the central portion remains practically intact for certain propagation distance [74].

One important fact to be mentioned here is that the self-healing property of BG beams is not guaranteed if the obstructing object is transparent. However, a plethora of research has been conducted about the resilience of BG beams around transparent obstructions and inhomogeneous scattering media [68,75–83]. These studies suggest the resilience of BG beams compared to Gaussian beams when affected by transparent obstructions and scattering media. When it comes to the passage of BG beams through turbulence there is no unanimity in literature. One recent study showed theoretically and experimentally that BG beams do not always self-heal from transparent obstructions, and never self-heal from turbulence where the entire beam is affected. However, this study is limited to a digital turbulence simulation [76].

In our present work, we verify the impact of a dynamic, transmissive Kolmogorov kind of turbulence on the BG beams. BG beams are produced using axicons and passed through a rotating pseudo-random phase plate (PRPP), mimicking atmospheric turbulence[31,32]. We

report on the propagation characteristics of these turbulence-impacted BG beams qualitatively by evaluating intensity line profiles and quantitatively by calculating the scintillation index and beam wandering parameters. The whole analysis is done using both simulations and experiments. The present study confirms the resilience of BG beams when passed through a dynamic Kolmogorov turbulence in certain propagation regions.

4.2 Experimental Procedure and Theory

4.2.1 Bessel Gaussian beams (BG beams)

There are four fundamental families of ideal non-diffracting optical beams which are the exact, propagation invariant solutions to the Helmholtz equation and each of these corresponds to a particular coordinate system. Plane waves, Bessel beams, Mathieu beams, and parabolic beams are respectively the ideal non-diffracting beams for Cartesian, circular cylindrical, elliptic cylindrical, and parabolic cylindrical coordinate systems [84].

A Helmholtz-Gauss beam is a practically attainable optical beam, whose wavefield described at the plane $z=0$ is in fact the product of a solution of the two-dimensional Helmholtz equation in the transverse field of an arbitrary nondiffracting beam and a radial Gaussian function. One such beam, called the Bessel-Gauss beams are a special case of Helmholtz-Gauss beams. The complex amplitude of the BG beam has the form in the source plane ($z=0$) and is given by,

$$U(r, \theta) = AJ_l(k_r r) \exp\left(\frac{-r^2}{\omega_0^2}\right) \exp(il\theta) \quad (4.1)$$

Where r is the distance from the z axis and θ is the azimuthal angle, A denotes the complex amplitude, J_l is the Bessel function of the first kind of order l , k_r corresponds to the radial component of wavevector, and ω_0 denotes the beam waist of the corresponding Gaussian beam.

4.2.2 Generation of BG beams using an axicon

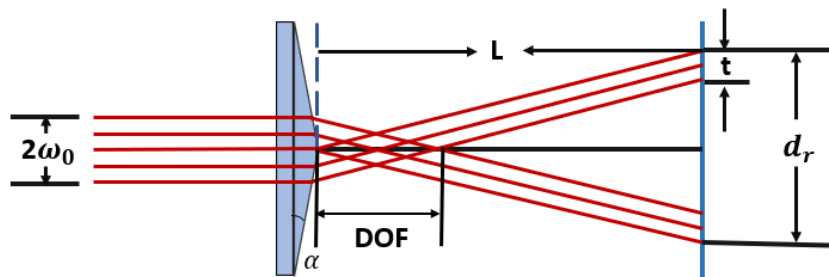


Figure 4. 1 Generation of Bessel Gaussian beam using an axicon of opening angle α . BG beams are formed in DOF (depth of focus) region.

BG beams are generated using axicons, annular slits, and digital holograms using spatial light modulators. The first reported experiment to generate a zeroth-order Bessel beam has been done by Durnin et al [72] and was done by illuminating an annular slit placed in the back focal plane of a lens with a plane wave. However, it has major drawback that most of the intensity of the incident beam gets blocked by the aperture. More efficient methods using holographic elements have also been reported. The most efficient technique to generate a fair

approximation to a zeroth-order Bessel beam is by the use of an axicon. If the waist size of illuminating Gaussian beam is smaller than the hard aperture of the axicon, the whole input intensity is converted into BG beam of zeroth order. Consider Fig. 4.1, where the process of generating BG beam using an axicon is shown. As depicted in Fig. 4.1, when a refracting axicon of opening angle α is illuminated by a Gaussian beam of radius ω_0 , we get BG beams in the depth of focus (DOF) region. The length of the DOF within which we get BG beams is given by,

$$DOF = \frac{\omega_0}{(n-1)\alpha} \quad (4.2)$$

Where n is the refractive index of the axicon. Beyond the DOF, the transverse profile of the beam changes to a ring shape. The thickness t of the ring is nearly equal to the radius of the input Gaussian beam. The diameter d_r of the ring at a distance L from the axicon is given by,

$$d_r \approx 2L \tan[(n-1)\alpha] \quad (4.3)$$

4.2.3 Simulation scheme



Figure. 4. 2 shows the scheme used for simulation studies. BG denotes Bessel-Gaussian beams.

To investigate the effect of Kolmogorov phase screen on the propagation of BG beams, we first simulated BG beams using the transmission function of axicon. The opening angle of axicon is varied from one to ten degrees with a step of one degree. Each of the simulated BG beams is propagated using a standard propagation algorithm and passed through a Kolmogorov phasescreen. In order to bring in the effect of dynamic turbulence, multiple phase screens are used. These turbulence- impacted beams are propagated further and are analysed qualitatively by finding their intensity line profiles, and quantitatively by calculating their scintillation index, and beam wander in Fresnel, Fourier and Fraunhofer regions. The simulation scheme is as shown in Fig.4. 2.

4.2.4 Experimental scheme

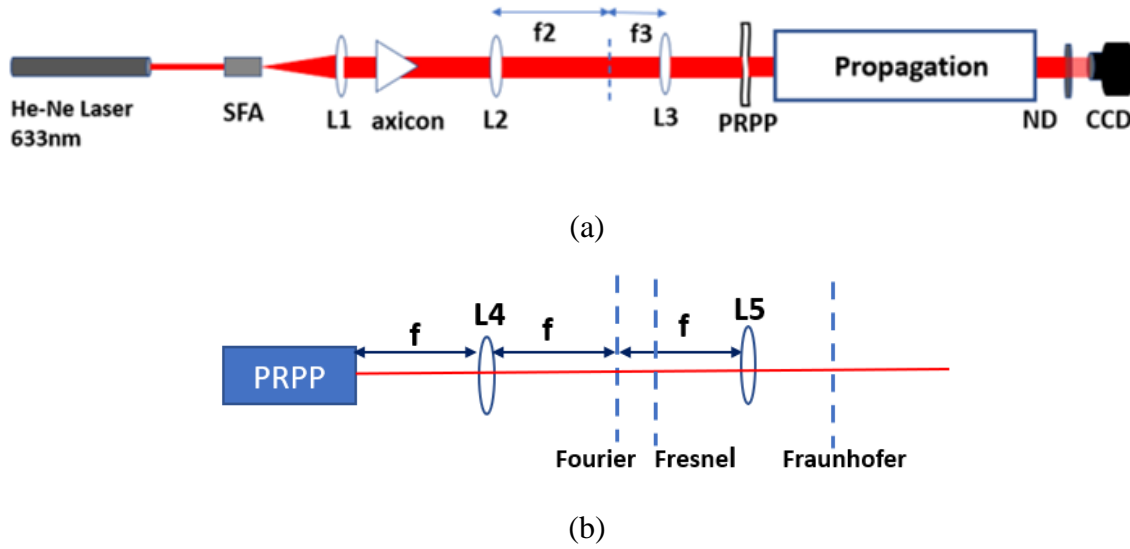


Figure. 4. 3 (a) shows the experimental setup for the generation of BG beams and passage through PRPP. SFA is spatial filter assembly and L1 is the collimating lens. Lenses L2 and L3 form a telescopic system. PRPP is the pseudo random phase plate while ND denotes a neutral density filter. CCD is the camera used. Figure 4.3(b) shows the propagation geometry used. Here L4 is a lens of focal length f . Lens L5 again of focal length f is used for Fraunhofer propagation.

Fig. 4.3 shows the experimental geometry where a laser beam from a He-Ne laser having wavelength of 633nm is spatially filtered and collimated using a lens L1 of focal length 50mm to obtain a Gaussian beam of radius 5mm. It is passed through axicons of refractive index 1.5 to generate BG beams. In the first experiment an axicon of opening angle 1° is used and in the second experiment the axicon angle is changed to 5° . In both cases, BG beams formed behind the axicon are passed through a telescopic system for dimensional scaling. The telescopic system consists of L2 and L3 having focal lengths f_2 and f_3 . Here f_2 and f_3 are taken as 30cms and 7.5cms so that the absolute value of angular magnification is four. The axicon with the opening angle one degree is used in the first case producing BG beam with the core radius of 0.8mm. Behind the telescopic system the core radius increases to 3.2mm. When an axicon of opening angle five degrees is used the initial central spot size is 0.5mm which increases to 2mm behind the telescopic system. The BG beams formed in each case are observed to maintain their shapes close to a distance of 0.75m. After this they tend to attain a ring shape. For the next experiment the axicon is removed such that we get a conventional Gaussian beam. All these beams are further passed through a rotating PRPP which is the atmospheric turbulence simulator. As shown in Fig. 4.3(b), after passing through the PRPP the beam is recorded using a CCD camera (Charge Coupled Device, PCO pixelfly USB 2.0) at three different propagation regions namely Fourier, Fresnel, and Fraunhofer regions. Neutral density filters are used to reduce the intensity of light beams falling onto the CCD. A lens L4 of focal length f ($=10\text{cm}$) is used to obtain the Fourier plane. The CCD is initially placed at this plane and slightly moved along positive z direction to reach the Fresnel region. Another lens L5 of focal length of f is used to obtain the Fraunhofer region. To create a dynamic turbulence effect, PRPP, which is fixed on a rotary stage, is rotated using a

stepper motor with the aid of a LabVIEW software. The speed of PRPP is kept at the lowest value so that CCD sees PRPP stationary at a particular instant. The turbulence-affected beams are sequentially recorded in Fourier, Fresnel, and Fraunhofer regions. These recorded beams are further processed in MATLAB to find the intensity line profile, scintillation index, and beam wander.

4.3 Results and Discussion

4.3.1 Line profiles

Fig. 4.4 shows the intensity line profiles of simulated BG beams before and after passing through the phase screen in the Fresnel region. The red lines show the input beams while the blue lines show the turbulence-impacted beams. Axicon angle used to generate BG beams is varied from one degree to ten degrees in steps of one. For the clarity only five peaks are shown for each BG beam. From Fig. 4.4 it is clear that the BG beams are more resilient to the impact of turbulence compared to conventional Gaussian beams and the resilience decreases as we increase the axicon angle. For the axicon angle of one degree the line profiles corresponding to both input beam and turbulence impacted beam nearly match. As we increase the axicon angle, for the same turbulence strength, there is a clear departure of turbulence impacted line profile from that of the input beam. The similar trend was observed in Fourier and Fraunhofer regions.

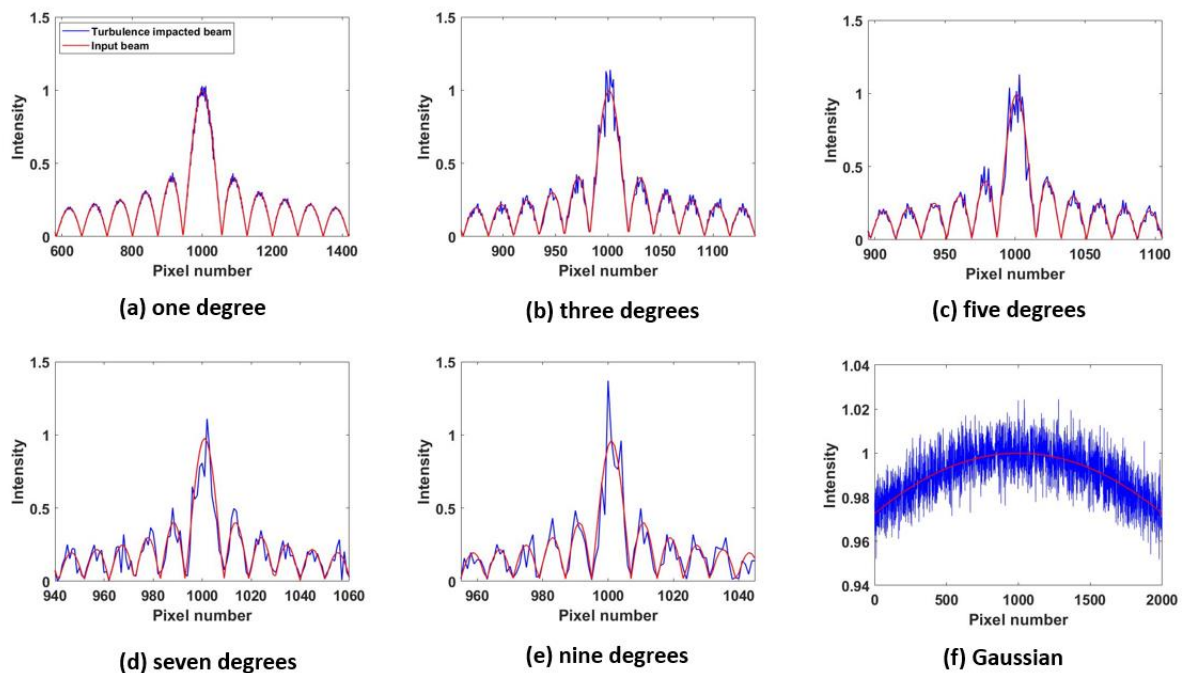
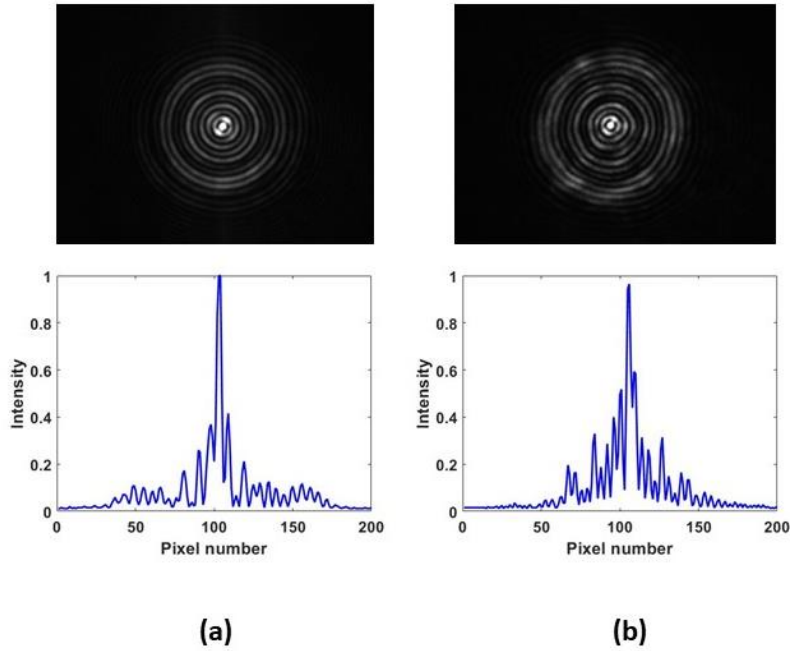


Figure. 4. 4 line profiles corresponding to BG beams of varying axicon angle (a-e) and conventional Gaussian beam(f). The blue line shows the line profiles of turbulence-impacted beams, and the red lines show that of input beams.

Fig. 4.5 shows the experimentally observed BG beams and Gaussian beams before and after the turbulence impact in the Fresnel region. The blue lines show their corresponding intensity line profiles. Fig. 4.5 (a-b) corresponds to BG beams formed by using an axicon of one

degree. Fig. 4.5 (a) is the input beam and Fig. 4.5 (b) is the turbulence impacted beam. There is a slight decrease in the intensity of turbulence impacted beam, however, BG beams nearly retain their shape even after passing through strong dynamic turbulence. Similarly, Fig. 4.5 (c-d) corresponds to BG beams, formed by using an axicon of five degrees, before and after passing through the PRPP. Here BG beams are also resilient to the impact of dynamic turbulence. However, the resilience is not as strong as that of BG beams formed by an axicon angle of one degree. Fig. 4.5 (e-f) corresponds to the conventional Gaussian beam before and after passing through the PRPP. One can clearly observe that conventional Gaussian beams lose their shape when affected by the turbulence. From Fig. 4.5 it can be concluded that the BG beams retain their shape even after passing through a transparent dynamic turbulence while conventional Gaussian beams lose their shape. When comparing BG beams generated by different axicons, it is evident that the resilience is more when the opening angle of the axicon is small. A similar trend is observed in the Fourier and Fraunhofer regions. This is exactly as predicted by the simulation results.



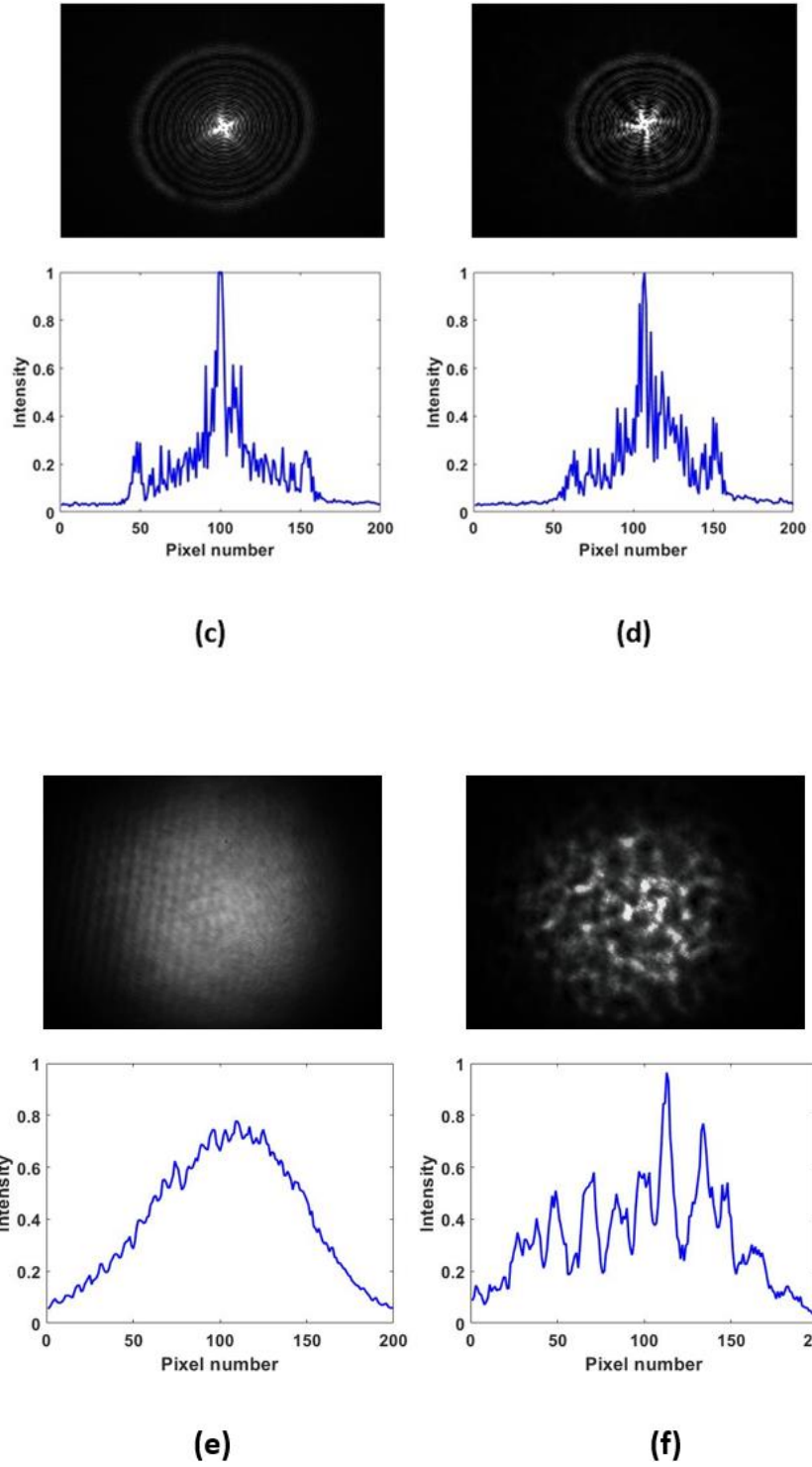


Figure. 4. 5 Images captured using CCD and their corresponding line profiles before and after turbulence impact. (a-b) correspond to BG beams formed by using an axicon of one degree. (c-d) correspond to BG beams formed by using an axicon of five degrees. (e-f) correspond to conventional Gaussian beam.

4.3.2 Scintillation index

We calculated the scintillation index of turbulent impacted BG beams generated by different axicon angles for the simulation geometry shown in Fig. 4.2 and the results are shown in Fig. 4.6. Here the calculations are done in Fourier, Fresnel, and Fraunhofer regions. One can easily infer from the images that there is a clear downtrend in the value of the scintillation index as we increase the axicon angle in the Fresnel region however in the Fourier and Fraunhofer regions the value of scintillation index increases with the increase in axicon angle. Even though the resilience of BG beams produced by the small axicon angles are larger as seen in line profiles, their scintillation index follows an opposite trend in the Fresnel region. In order to explain this discrepancy, we calculated the lateral speckle size of each turbulence impacted beam in three different propagation regions. It is in fact the laser speckles arising due to the turbulence impact that causes the observed scintillation effect. The speckle size is estimated as the full width half maximum of peak obtained through autocorrelation of recorded images and is found out that the lateral speckle size of the beams in Fresnel region is much smaller than that of the beams in the Fourier and Fraunhofer regions. This could be due to the interference of different plane waves emanating from the axicon in the Fresnel region. With the increase of axicon angle, the separation between plane waves becomes larger and the effect of interference becomes less conspicuous. This is manifested as the larger speckles when we increase the axicon angle. The effect of interference becomes negligible in the Fourier region and Fraunhofer regions again yielding larger speckles.

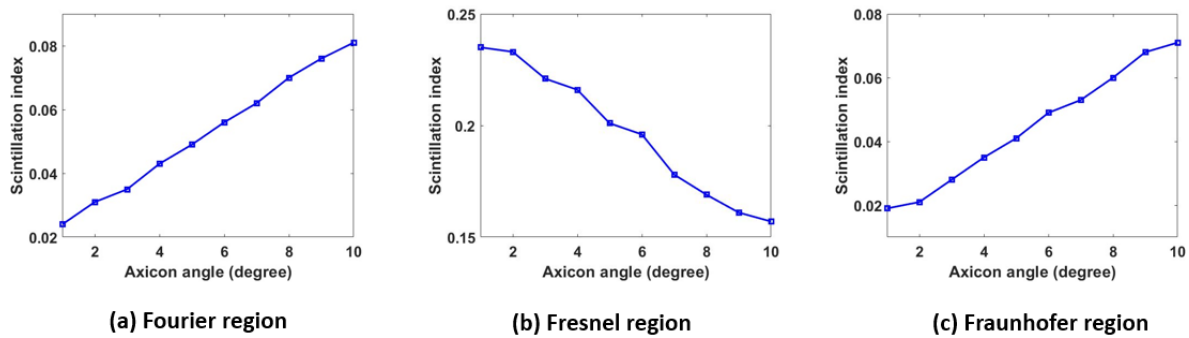


Figure. 4. 6 shows the scintillation index corresponding to turbulence-impacted BG beams in Fourier, Fresnel and Fraunhofer regions corresponding to the simulation geometry shown in Fig. 4. 2.

Table 4.1 summarises the calculated scintillation index and speckle sizes for the experimental geometry as shown in Fig. 4.3 in Fourier, Fresnel and Fraunhofer regions.

Table 4. 1 The calculated scintillation index and speckle sizes for BG beams and Gaussian beam in Fourier, Fresnel and Fraunhofer regions.

Beam type	Fourier		Fresnel		Fraunhofer	
	Speckle size (mm)	Scintillation index	Speckle size (mm)	Scintillation index	Speckle size (mm)	Scintillation index
Gaussian	0.229	0.0688	0.187	0.074	0.205	0.0701
BG (Five)	0.282	0.0442	0.162	0.091	0.268	0.0463

BG (One)	0.345	0.0212	0.139	0.103	0.321	0.0232
-----------------	-------	--------	-------	-------	-------	--------

From the Table 4.1 it is evident that , in Fourier and Fraunhofer regions, the scintillation index is smaller for BG beams compared to the conventional Gaussian beam. It can be seen that the value of scintillation index increases with the increase in axicon angle. There is clear proportionality between speckle size and the value of scintillation index. Smaller speckle size corresponds to larger scintillation index. In Fresnel region, as expected from the simulation results, the scintillation index is larger for BG beams and the value decreases with the increase in axicon angle. As discussed earlier this could be attributed to the interference of plane waves in the Fresnel region. One can notice that value of scintillation index for Gaussian beams in three regions remain nearly constant with a standard deviation of 0.0027 while the standard deviations of BG beams are respectively 0.0264 and 0.0467 for axicon angles of five degrees and one degree. Since the Gaussian beam comprises a single k vector it is devoid of the effect of interference and keeps the nearly constant speckle size in all three regions. The change in value for speckle size is observed for BG beams because of the presence of different k vectors and their possibility of interference. From simulation results and experimental observations, it can be concluded that BG beam generated using smaller axicon angle is less affected by the impact of turbulence in Fourier and Fraunhofer regions. This makes them a better candidate for free space optical communications than conventional Gaussian beams.

4.3.3 Beam wander

Fig.4.7 shows the beam wander in both x and y directions for the simulation geometry. Here also a clear trend is observed for BG beams produced using different axicon angles. With the increase in axicon angle, the beam suffers more wandering both in x and y directions. Unlike the scintillation index, a similar trend is observed for beam wandering in Fourier, Fresnel and Fraunhofer regions. One can easily understand the fact that the wandering of beam from its initial position does not depend on the speckle size.

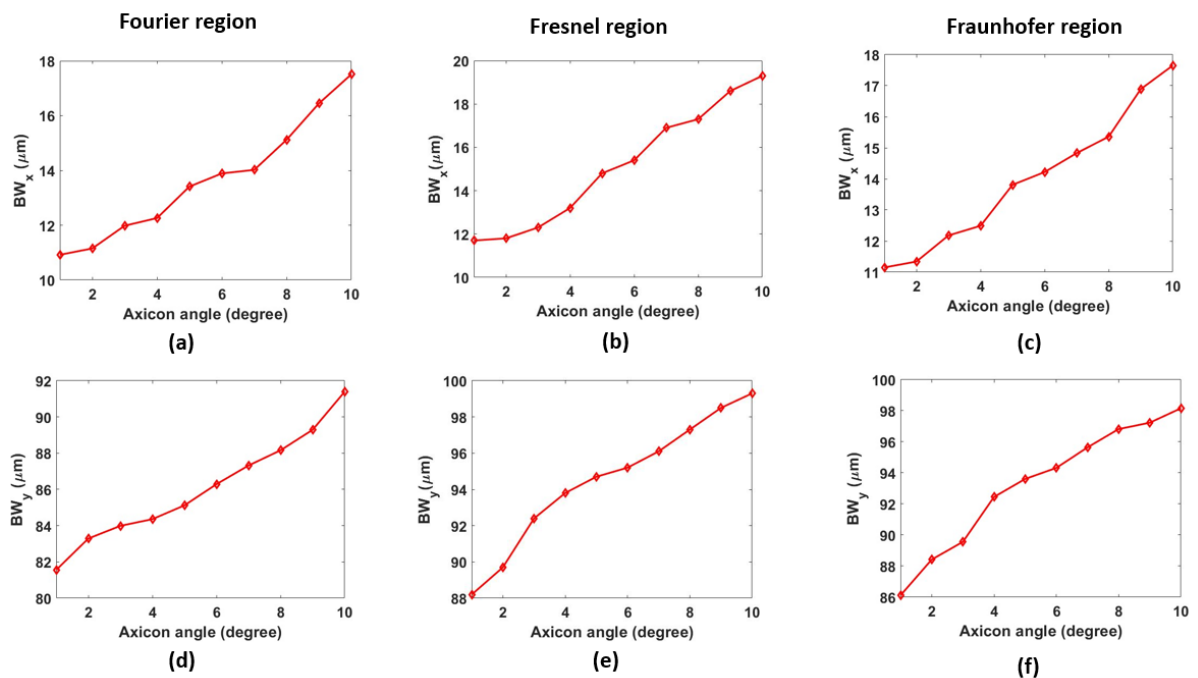


Figure. 4. 7 shows the beam wander corresponding to turbulence-impacted BG beams simulated using different axicons. Fig4.7(a-c) show the beam wander along the x-direction in Fourier, Fresnel and Fraunhofer regions respectively while (d-f) show the beam wander along the y-direction.

Table 4.2 summarises the calculated beam wander in x and y directions for the experimental geometry as shown in Fig.4.3 in Fourier, Fresnel and Fraunhofer regions.

Table 4. 2 The calculated beam wander for BG beams and Gaussian beam in Fourier, Fresnel and Fraunhofer regions along x and y directions

Beam shape	Fourier		Fresnel		Fraunhofer	
	BW _x (μm)	BW _y (μm)	BW _x (μm)	BW _y (μm)	BW _x (μm)	BW _y (μm)
Gaussian	32.23	120.34	38.12	125.65	36.47	123.19
BG (Five)	16.43	88.38	22.72	94.30	19.12	91.43
BG (One)	13.41	79.62	18.46	85.78	15.32	82.17

One can observe that BG beams have smaller beam wandering compared to conventional Gaussian beams in all three propagation regions. The beam wander along the y-direction is found out to be larger than that along the x direction under all varied experimental conditions. This can be explained using the rotation of the PRPP. Consider Fig.4.8 in which the incident beam is shown as point A and the direction of rotation of the PRPP is shown with the arrow. Clearly the beam sees turbulence as moving along the y direction making the dynamic turbulence anisotropic in nature. Since we are finding the beam wander for the sequential images, a higher value of beam wander along the y direction is expected. With the increase in axicon angle, the beam suffers more wandering both in x and y directions. Except from this anisotropy the beam follows the exact same trend in both the x and y directions confirming the resilience of BG beams to the impact of turbulence.

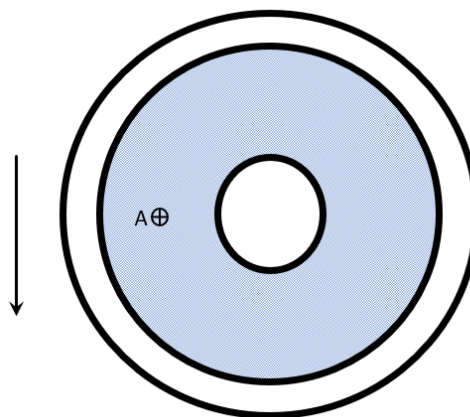
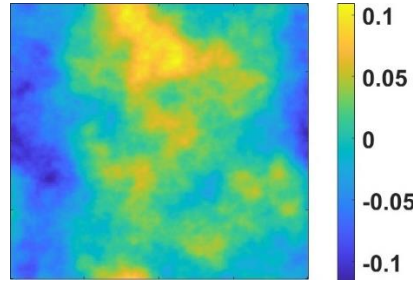


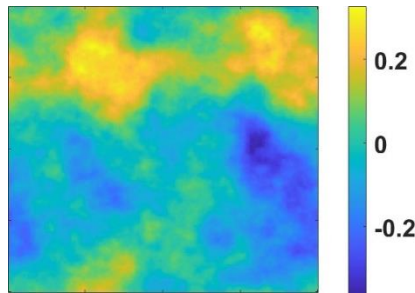
Figure. 4. 8 Schematic representation of the PRPP. Shaded region represents the area of phase aberrations. Point A shows the input beam and arrow shows the direction of rotation of the PRPP.

4.3.4 Simulation studies

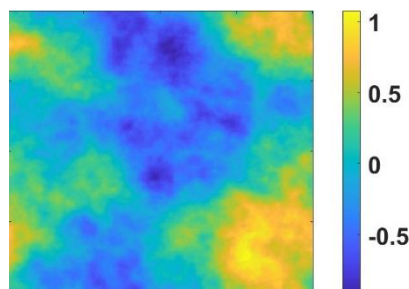
In order to validate our experimental results to actual FSO scales a simulation verification is carried out. Phase screens with turbulence strength matching to the actual atmospheric conditions are simulated, and BG beams corresponding to different axicon angles are passed through it. The single instances of simulated phase screens of variable strengths are shown in Fig. 4.9 and the Fig.4.10 shows the simulated BG beams Here, the grid size was taken to be 256x256. The colour bar indicates the phase values in radians. The input beams are propagated through multiple phase screens of varying distances. The propagation distances are varied from 0.25km to 1.5kms again to match the actual FSO scales.



$$(a)C_n^2 = 10^{-17} m^{-2/3}$$

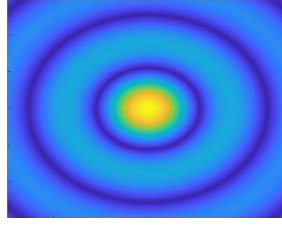


$$(b)C_n^2 = 10^{-16} m^{-2/3}$$

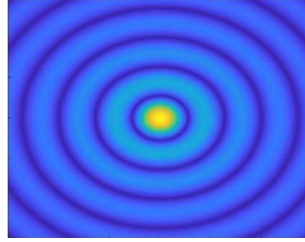


$$(c)C_n^2 = 10^{-15} m^{-2/3}$$

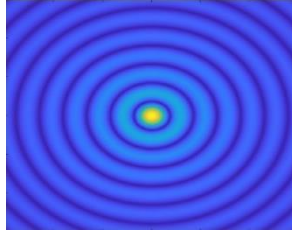
Figure 4.9 (a-c) show the simulated phase screens of increasing turbulence strength. The phase values are in radians.



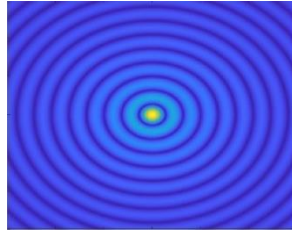
(a) $\alpha = 1^\circ$



(b) $\alpha = 2^\circ$



(c) $\alpha = 3^\circ$



(d) $\alpha = 4^\circ$

Figure 4.10 Bessel-Gaussian beams simulated with varying axicon angles.

Table 4.3 to 4.5 show the turbulence impacted beams propagated into different distances through multiple phase screens of refractive index structure parameter $C_n^2 = 10^{-17} m^{-2/3}$, $C_n^2 = 10^{-16} m^{-2/3}$, and $C_n^2 = 10^{-15} m^{-2/3}$ respectively.

Table 4. 3 Turbulence impacted BG beams for different propagation regions for $C_n^2 = 10^{-17} \text{m}^{-2/3}$.

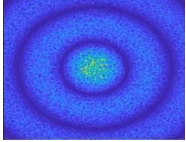
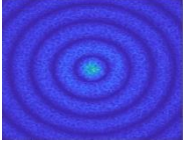
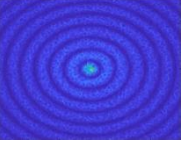
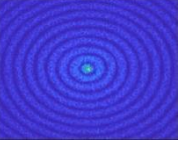
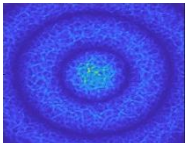
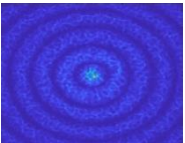
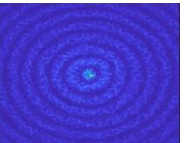
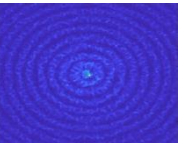
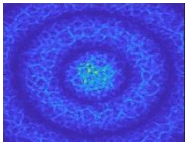
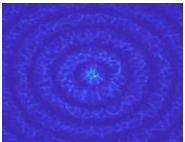
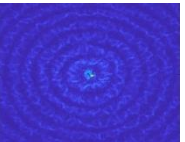
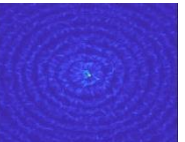
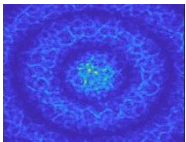
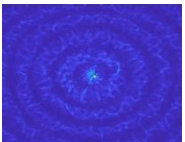
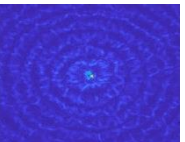
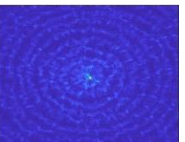
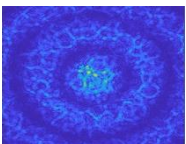
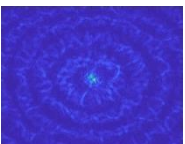
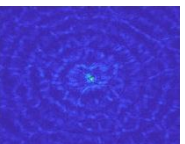
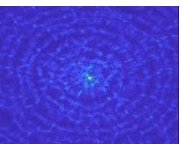
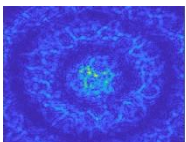
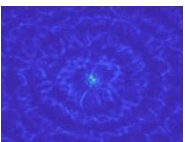
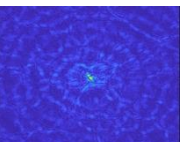
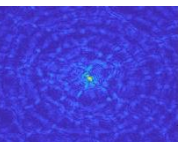
Propagation (m)	Axicon angle (degree)			
	1	2	3	4
250				
500				
750				
1000				
1250				
1500				

Table 4. 4 Turbulence impacted BG beams for different propagation regions for $C_n^2 = 10^{-16} m^{-2/3}$.

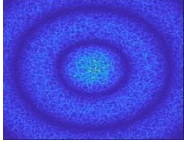
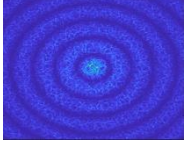
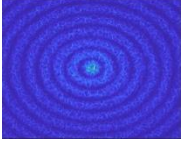
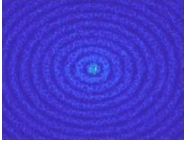
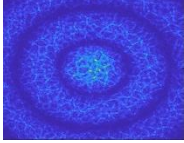
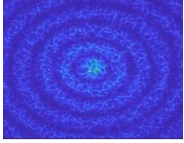
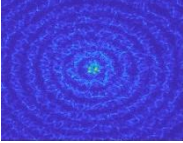
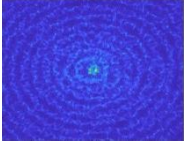
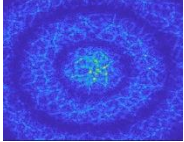
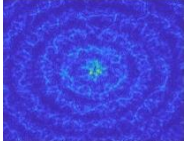
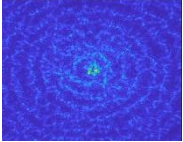
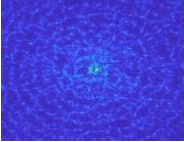
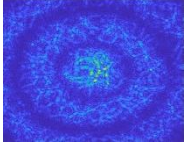
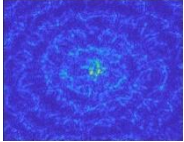
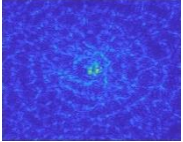
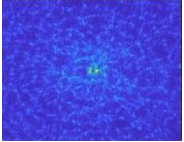
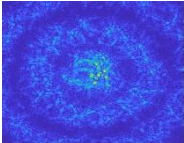
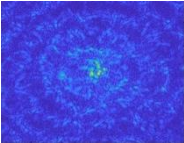
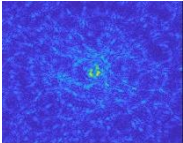
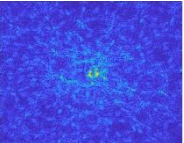
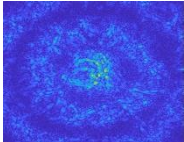
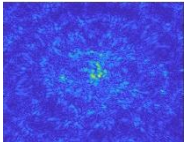
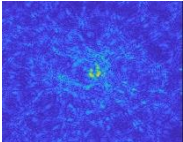
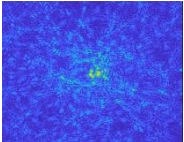
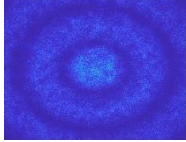
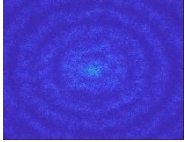
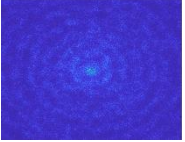
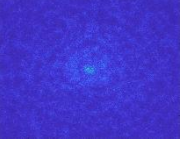
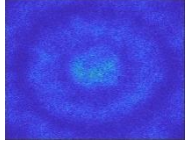
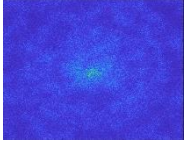
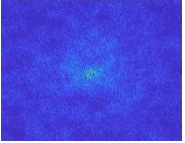
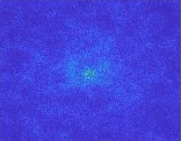
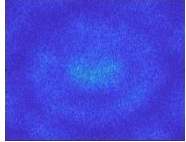
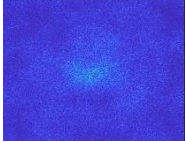
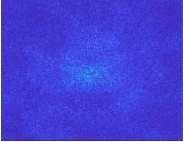
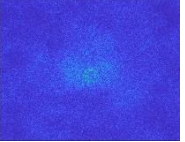
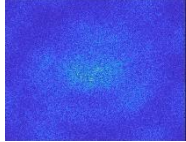
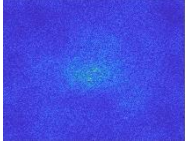
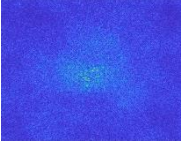
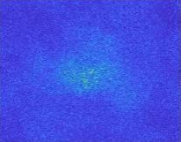
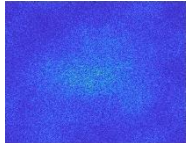
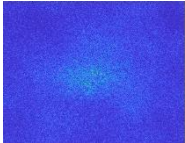
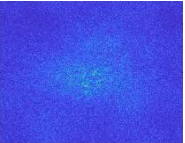
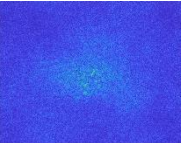
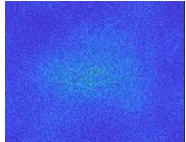
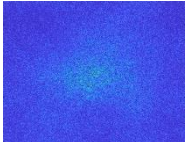
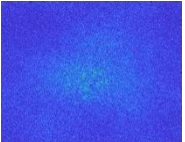
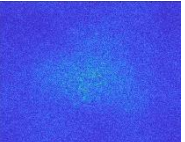
Propagation (m)	Axicon angle (degree)			
	1	2	3	4
250				
500				
750				
1000				
1250				
1500				

Table 4. 5 Turbulence impacted BG beams for different propagation regions for $C_n^2 = 10^{-15} m^{-2/3}$.

Propagation (m)	Axicon angle (degree)			
	1	2	3	4
250				
500				
750				
1000				
1250				
1500				

As expected from the experimental studies, BG beams produced using the axicon of smaller opening angle outperform those beams produced using axicons of bigger opening angle. For smaller turbulence strength, i.e., $C_n^2 = 10^{-17} m^{-2/3}$ BG beams produced using one-degree axicon angle fairly retains its shape up to a propagation distance of 1500m while BG beam produced using four degrees axicon loses its shape after a propagation distance of 750m. A similar

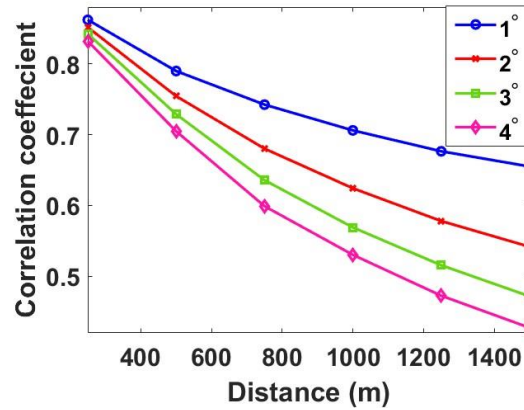
trend is observed for stronger turbulence as well. For a turbulence strength of $C_n^2 = 10^{-15} m^{-2/3}$ the beam loses its shape after 500m even for the beams produced using smaller angle axicons. Hence, we can conclude that, BG beams can be used for long distance communication purposes only when the turbulence strength is small.

Next, we evaluated the two-dimensional correlation coefficient between the input beams and the turbulence affected beams in different propagation distances to quantify the effect of turbulence impact. A higher correlation coefficient indicates that the beam is less effected by turbulence, whereas a lower correlation coefficient indicates that turbulence has a greater impact. The mathematical expression of two-dimensional correlation coefficient between two complex matrices A_{mn} and B_{mn} is given by,

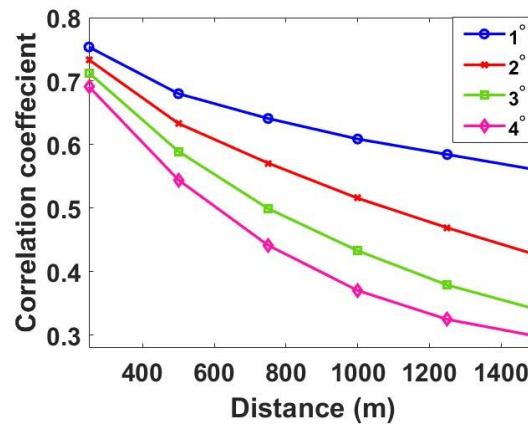
$$cc = \frac{\sum_m \sum_n (A_{mn} - \bar{A})(B_{mn} - \bar{B})}{\sqrt{\sum_m \sum_n [(A_{mn} - \bar{A})^2] [\sum_m \sum_n (B_{mn} - \bar{B})^2]}} \quad (4.4)$$

Where \bar{A} and \bar{B} denote the mean of all values in those matrices.

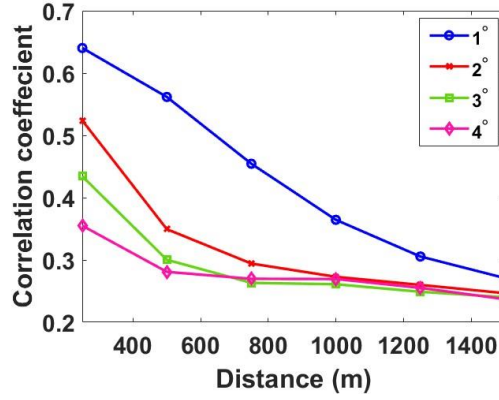
The correlation coefficient versus distance plot of different BG beams under different turbulence intensities is shown in Fig. 4.11.



(a) $C_n^2 = 10^{-17} m^{-2/3}$



$$(b) C_n^2 = 10^{-16} m^{-2/3}$$

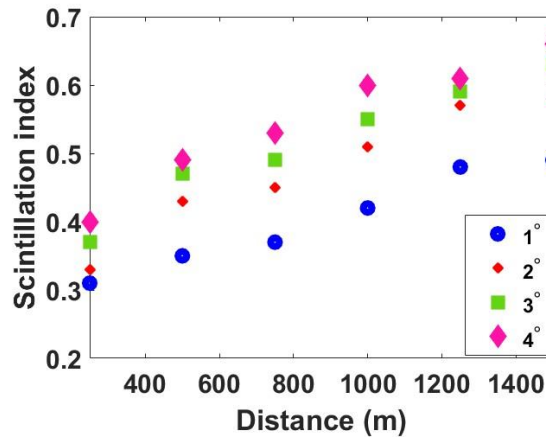


$$(c) C_n^2 = 10^{-15} m^{-2/3}$$

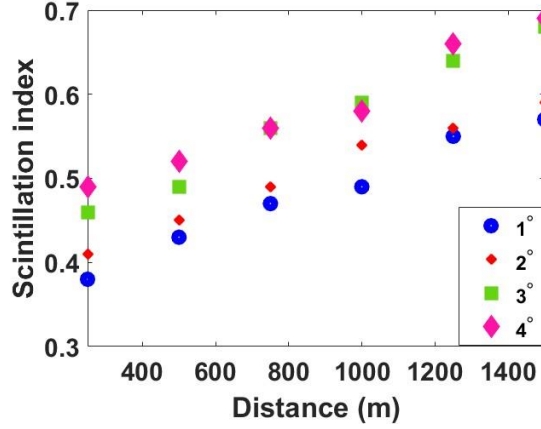
Figure 4.11 (a-c) show the correlation vs distance plot for different turbulent strengths.

One can infer from the correlation calculations that there is a clear downtrend for correlation coefficients as we increase the propagation distance and axicon angle. As suggested by the simulation results in the previous section BG beams produced using the smaller axicon angles show larger correlation coefficients suggesting greater resilience and vice versa. The rate at which the correlation coefficients fall nearly follows the same value for smaller turbulence value but there is a rapid decline in correlation coefficient for higher axicon angle beams under stronger turbulence. It can be seen that BG beams produced via smaller axicon angles are better suited for communication applications where the turbulence is stronger, and the propagation distances are relatively larger compared to the other BG beams.

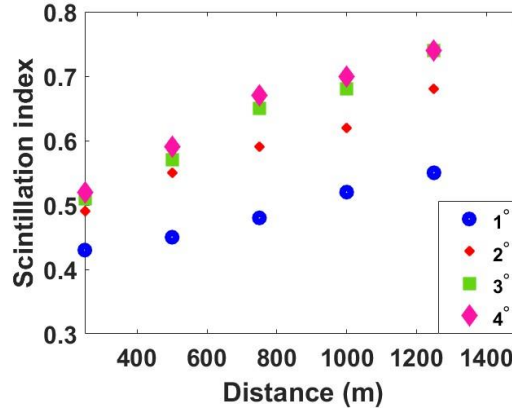
To verify our simulation and experimental analysis, we have calculated the scintillation index of turbulence impacted beams in different propagation regions. The calculation is repeated for different turbulence strengths and the results are shown in Fig. 4.12.



$$(a) C_n^2 = 10^{-17} m^{-2/3}$$



$$(b) C_n^2 = 10^{-16} m^{-2/3}$$



$$(c) C_n^2 = 10^{-15} m^{-2/3}$$

Figure 4.12 (a-c) show the scintillation index vs distance plot for different turbulent strengths.

Scintillation index calculations further establish the result that BG beams produces using smaller axicon angles are a better choice for FSO communication systems. From weaker to stronger turbulence and in all propagation distances they show smaller scintillation index values suggesting larger resilience. For stronger turbulence, BG beams corresponding to the axicon angle of one degree shows much smaller scintillation index, again indicating the result that they are a better candidate compared to the other BG beams, when the turbulence is stronger and propagation distances are larger.

4.4 Conclusions

In this chapter, we have successfully generated BG beams through simulations and by using axicons. These BG beams and conventional Gaussian beams are passed through a dynamic transmissive Kolmogorov turbulence simulator. The scintillation index, beam wander and intensity line profiles are calculated for different axicon angles in Fresnel, Fourier and Fraunhofer regions. We found that, compared to Gaussian beams, the BG beams show much less scintillation index in Fourier and Fraunhofer regions. In the case of beam wandering along both x and y directions, BG beams show smaller wandering compared to laser Gaussian beam. One of the main results of our experiment can be seen in Fig. 4.5 which

clearly shows the ability of BG beams to retain their shape even after passing through dynamic turbulence. This is the first time in the literature the effect of dynamic turbulence on BG beams is investigated. There is a clear match between experimental and simulation investigations, and it confirms the insensitivity of BG beams to the impact of dynamic turbulence compared to the conventional Gaussian beam. The experimental results are further verified by extending the turbulence strength and propagation distances to the actual atmospheric turbulence scales using simulations. These results find applications in free-space communications because of the resemblance of experimental conditions to the actual atmospheric turbulence.

CHAPTER 5

ROBUSTNESS OF PARTIALLY COHERENT VORTEX BEAMS TO THE IMPACT OF DYNAMIC KOLMOGOROV KIND OF TURBULENCE.

5.1 Introduction

In the case of free-space optical communication systems, scintillations cause an increase in the link error probability, which reduces the overall performance[85]. A plethora of research has been done on the optimization of transmitting beams for free space optical communication systems. Such optimization techniques comprise altering their degree of coherence, degree of polarization, or using different classes of beam shapes[50–52,55,69,86,87]. It has been verified that optical vortex beams carrying twist phases are more resilient to the impact of turbulence compared to the optical beams without such helical phases[88–92]. Vortex beams carry orbital angular momentum because of their helical phase. These orbital angular momentum (OAM) modes possessed by vortex beams can be used as an infinite basis set for free-space optical communication channels. This increases channel capacity without increasing the spectral bandwidth[93]. For a communications system, the orthogonality property of optical beams carrying vortex phases is indispensable. It implies that multiple independent data-carrying optical beams can be multiplexed and transmitted simultaneously in free space, thereby multiplying the system's data capacity by the total number of beams[83].

Many attempts have been made to study the resilience of optical beams with vortex phase in partially coherent regime when it passes through turbulence[94–97]. But none of them explore the effect of a controllable dynamic turbulence in the Kolmogorov regime.

In this work, we present the wave propagation analysis of Gaussian and partially coherent topologically charged beams (Gaussian Schell model vortex beams) through a dynamic (rotating) random phase screen which simulates atmospheric turbulence in the Kolmogorov turbulence regime. Experimental and simulation results are provided. These results can be effectively employed in free-space optical communication systems because of their resemblance to the actual atmospheric conditions.

5.2 Experimental Procedure and Theory

In the experiment scheme as shown in Fig. 5.1, light from a He-Ne laser of wavelength 633nm is spatially filtered and collimated using a lens L of focal length of 50mm. The collimated laser beam further passes through a vortex phase plate (RC Photonics) to generate a topologically charged beam. The laser beam is passed through different regions of the phase plate so as to produce vortex beams of charges zero to three. These beams then fall on the spatial light modulator (SLM). The SLM used in the present study is Holoeye PLUTO phase-only SLM based on reflective LCOS micro-displays. It has a resolution of 1920×1080 pixels and pixel size of $8\mu\text{m}$. It is optimized for different wavelength ranges (420-1700 nm). Phase profiles of simulated GSM beams in different coherence regimes, as shown in Fig. 5.1, are fed onto the SLM one at a time. The reflected beam from SLM then passes through an aperture and a mirror. Here the aperture is used to select first-order diffraction order. The mirror reflects this beam towards a pseudo-random phase plate which is the atmospheric

turbulence simulator. After passing through the PRPP the beam is detected using the CCD camera (Charge Coupled Device, PCO pixelfly USB). The distance between the PRPP and the CCD is chosen to be 50cms such that the effect of propagation also comes into the picture. To create a dynamic turbulence effect, PRPP, which is fixed on a rotary stage, is rotated using a stepper motor with the aid of LabVIEW software. However, the speed of PRPP is kept at the lowest value so that CCD sees the PRPP stationary at a particular instance. In order to synchronize the CCD with the SLM, we used an external trigger function with a function generator (Tektronics-AFG3022B). Phase maps of GSM beams are loaded onto SLM for different coherence lengths. For each phase map, turbulence-impacted beams are viewed with CCD. One thousand images are sequentially captured using CCD. These recorded beams are further processed in MATLAB to find the intensity line profile, scintillation index, and beam wander. The process is repeated for vortex beams having charges zero to three.

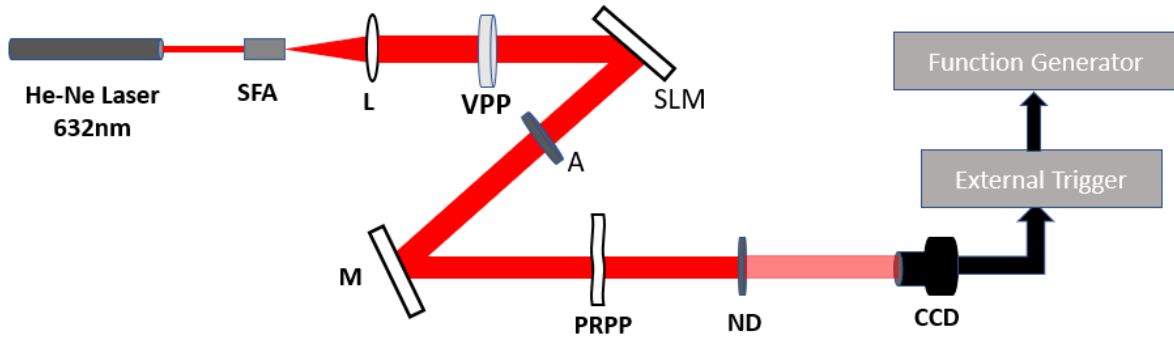


Figure 5. 1 shows the experimental setup where SFA denotes the spatial filter assembly and L is the collimating lens. VPP is the vortex phase plate while SLM denotes the spatial light modulator. A is an aperture and M denotes a mirror. PRPP is the pseudo-random phase plate, ND denotes a neutral density filter while BS is a beamsplitter. CCD is the camera used for recording images.

5.3 Simulation Scheme

In the simulation studies, the experimental results obtained at the laboratory level are verified by extending the parameters to the actual FSO scales. To investigate the effect of Kolmogorov phase screen on the propagation of partially coherent vortex beams, we first simulated Gaussian beams having vortex phase convolved with a Gaussian correlated random function of variable coherence width 0.2mm [22,23]. The topological charge of vortex beams is varied from zero to three. Each of the simulated GSMV beams is impacted by a Kolmogorov phase screen of thickness 0.5km to 5km. The refractive structure constant, C_n^2 is varied from 10^{-17} to $10^{-13} m^{-2/3}$ [22]. In order to bring in the effect of real turbulence scenario, multiple phase screens are used. The number phase screens are increased gradually to see the effect of propagation. These turbulence-impacted beams are analysed by finding the scintillation index and correlation coefficients.

5.4 Results and Discussion

5.4.1 Amplitude and phase images of GSM beams

A few instances of phase and amplitude of GSM beams simulated are shown in Fig. 5. 2 [22,23]. These phase profiles are fed onto the SLM to generate GSM beams with gradually

varying coherence widths. These phase profiles are fed onto the SLM to generate required GSMV beams.

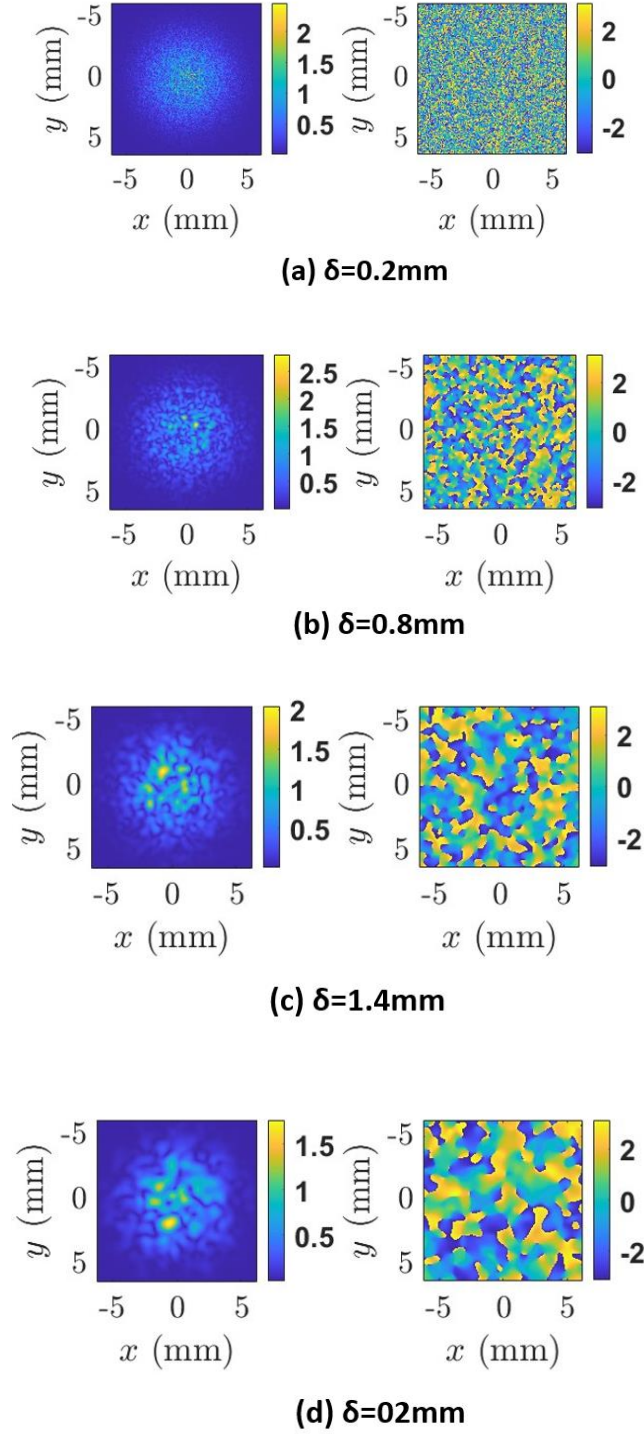


Figure. 5. 2 Shows the amplitude and phase of simulated Gaussian Schell model beams for $\delta = 0.2\text{mm}, 0.8\text{mm}, 1.4\text{mm}$, and 2mm respectively.

5.4.2 Experimental observations

Fig. 5.3 shows a few instances of the images captured using CCD before and after passing through the PRPP. Here, the coherence length is kept at one millimeter and the topological

charges are varied from zero to three. Fig. 5.3(a) is the conventional Gaussian beam (topological charge zero) and Fig. 5.3(b) is the same beam after the impact of turbulence. It is clear from the figure that the Gaussian beam is largely affected after passing through the PRPP. Fig. 5.3(c) and Fig. 5.3(d) are respectively the GSMV of order one before and after turbulence impact. Here also, one can observe the effect of the random phase screen, but the beam tends to keep its shape intact. Similarly, Fig. 5.3(e) and Fig. 5.3(f) correspond to the input and turbulence-impacted beams of order two. The impact of turbulence is evident in Fig. 5.3(f); however, it fairly retains shape. Fig. 5.3(g) is the GSMV beam of topological charge three and Fig. 5.3(h) is the same beam after the impact of turbulence. It can be clearly seen that, even after passing through the phase screen, the beam preserves its shape and shows considerable resilience in the case of higher order beams, compared to beams of lower orders. Our experimental observations also confirm the fact that partially coherent vortex beams are insensitive to the impact of turbulence.

5.4.3 Line profiles

Fig. 5.4 to Fig. 5.7 show a few examples of the line profiles of GSMV beams of different orders. Blue lines show the line profiles of input beams and red lines show that of the turbulence impacted beams. Line profiles of direct and turbulence impacted GSMV beams of order zero are depicted in Fig. 5.4. Here, the coherence width (\mathcal{S}) is varied from 0.2mm to 2mm. As inferred from Fig. 5.3, GSMV beams of order zero are greatly impacted by the phase screen. This fact is confirmed by the departure of turbulence-impacted beam line profile from that of the input beam. Line profiles of direct and turbulence impacted GSMV beams of the first order are shown in Fig. 5.5. Here also, the coherence width (\mathcal{S}) is varied from 0.2mm to 2mm. One can easily observe that these beams tend to retain their shape. However, as we increase the coherence length, turbulence-impacted beams slightly wander from their initial position. Similarly, line profiles of direct and turbulence impacted GSMV beams of the second order are shown in Fig. 5.6 when the coherence width (\mathcal{S}) is varied from 0.2mm to 2mm. Further, it can be easily seen that these beams tend to retain their shape and as we increase the coherence length turbulence-impacted beams slightly wander from their initial position. Finally, Fig. 5.7 shows the line profiles of direct and turbulence impacted GSMV beams of the third order. Even after passing through the phase screen, the beam clearly preserves its shape. It shows greater resilience compared to beams of lower orders. However, these beams also suffer from beam wander as we increase the coherence length.

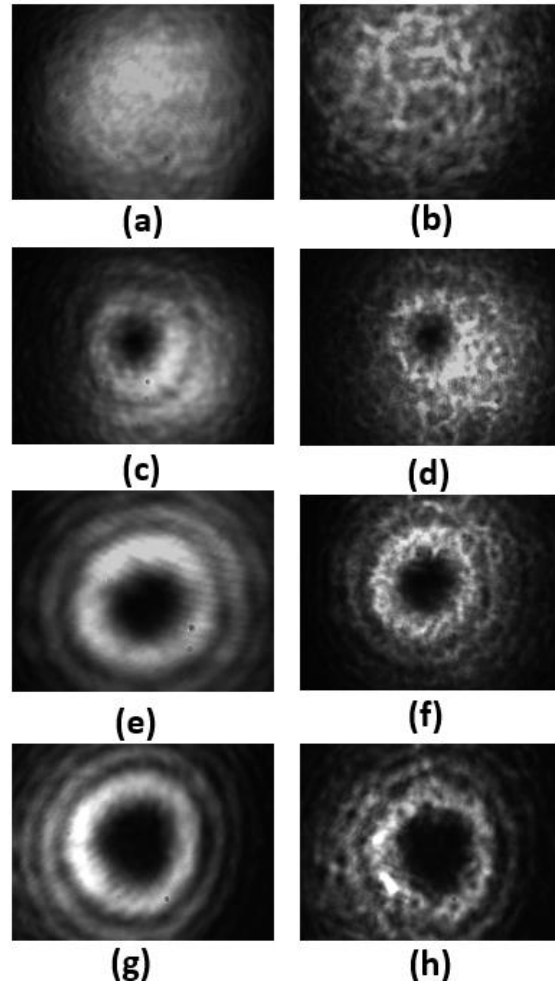


Figure. 5. 3shows the input beams(left side) and turbulence impacted beams(right side) of GSMV beams of various modes with coherence width one mm.

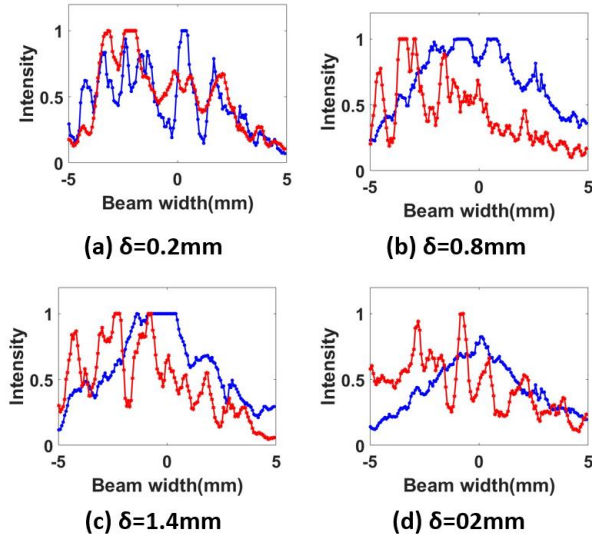


Figure. 5. 4 Line profiles of GSMV beam of zero order with different coherence widths.

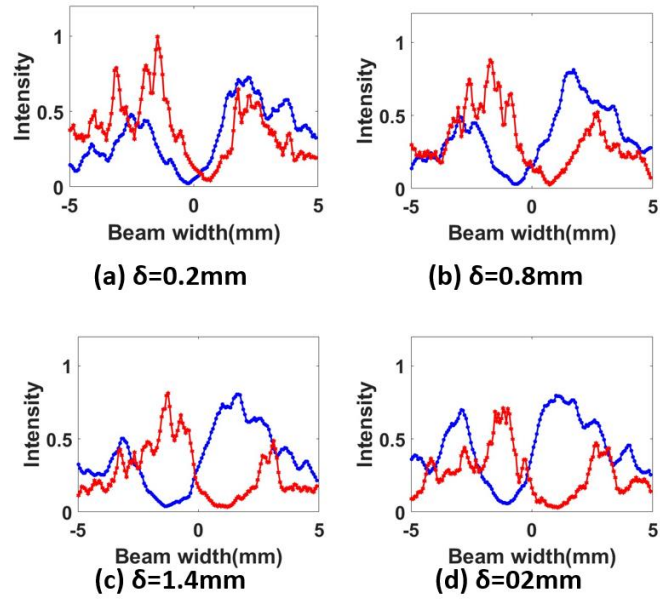


Figure. 5. 5 Line profiles of GSMV beam of first order with different coherence widths.

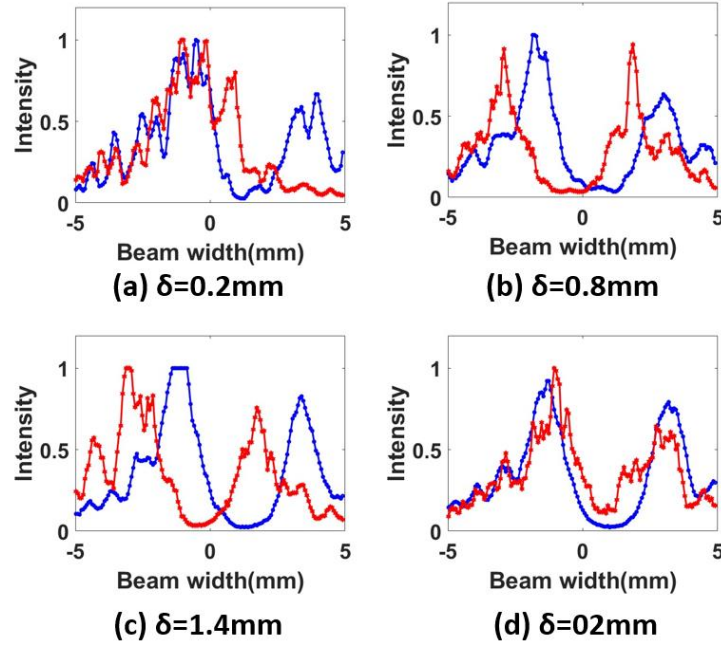


Figure. 5. 6. Line profiles of GSMV beam of second order with different coherence widths.

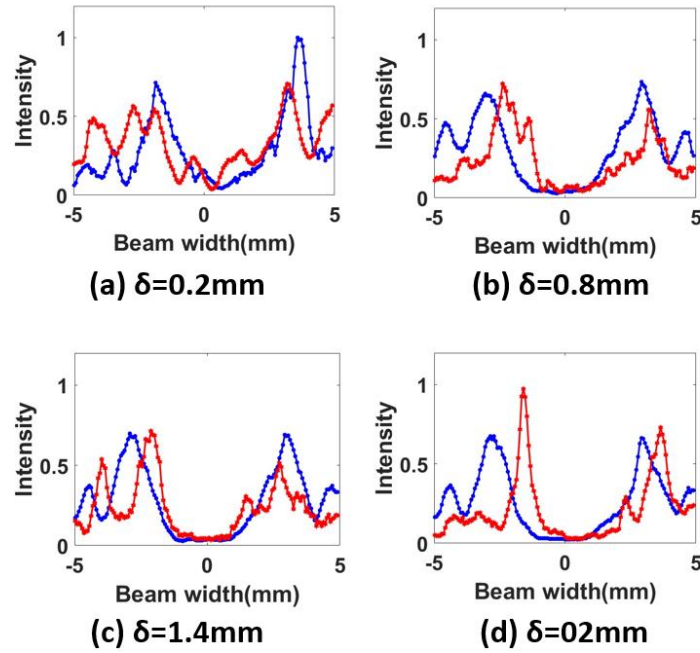


Figure. 5. 7 Line profiles of GSMV beam of third order with different coherence widths.

5.4.4 Scintillation index

The scintillation index is calculated using the sequential images captured from the experimental scheme shown in Fig. 5.1. Since the vortex beams possess a donut shape, we have to modify the method to calculate the scintillation index . For each propagation distance,

the corresponding beam width is found out using the free propagation algorithm and is denoted by $w(z)$. Then the irradiance of the numerically calculated vortex beams propagated through turbulence with an annular area between radii of $(1+10\%) w(z)$ and $(1-10\%) w(z)$ are used for the scintillation index as described in [98].

Fig.5.8 shows the scintillation index values obtained for GSMV beams of four orders with different coherence lengths. For zero order GSMV beam, the scintillation index is larger than that of the other GSMV beams. GSMV beams of higher orders shows lesser scintillation effects and minimum value of scintillation index is observed for GSMV beam of third order. From Fig.5.8, it can be clearly seen that the scintillation index increases as we increase the coherence length. And this trend is followed by GSMV beams of all orders. Scintillation index calculations again confirms the resilience of GSMV beams of higher orders.

5.4.5 Simulation results

The single instances of simulated phase screens of variable strengths are shown in Fig.5.9 and the Fig.5.10 shows the simulated GSMV beams of different topological charges with a coherence width of 0.2mm. We kept the coherence width at the minimum because of their greater resilience to the turbulence impact. Here, the grid size was taken to be 256x256. The color bar indicates the phase values in radians. The strengths of the phase screens are chosen so that they resemble to the actual atmospheric conditions. The input beams are propagated through multiple phase screens of varying distances. The propagation distances are varied from 0.5km to 1.5kms again to match the actual FSO scales. Table 5.1 shows the turbulence impacted beams propagated into different distances through multiple phase screens of refractive index structure parameter $C_n^2 = 10^{-17} m^{-2/3}$. Excluding the zero order GSM beam, one can observe that the optical vorticity is lost when we propagate the turbulence impacted beams to a certain distance. The first order GSMV beam preserves its vorticity up to a distance of 500m whereas the second order GSMV beam is able to keep the donut shape up to a distance of 750m. As expected from the laboratory level experiments, the third order GSMV beam is capable of sustaining its vorticity to a longer propagation distance. As inferred from the table, the singularity of third order beam is preserved even up to the distance of 1000m making it a better candidate for FSO communication applications. The same trend is observed even for stronger turbulence regimes.

In order to quantitatively estimate the effect of turbulence impact, we have calculated the two-dimensional correlation coefficient between the input beams and the turbulence impacted beams in different propagation distances. A higher value of correlation coefficient suggests that the beam is less impacted by the turbulence and a lesser value of correlation coefficient is suggestive of stronger impact of the turbulence. Fig.5.11 shows the correlation coefficient vs distance plot of GSMV beams of different order under different turbulence strengths. It can be clearly seen that the correlation coefficients for higher order topological charges possess smaller value implying their greater resilience to the effect of random phase fluctuations. For smaller propagation distances their values mostly converge, and the difference becomes conspicuous as we increase the propagation distances. However, for stronger turbulence the value of correlation coefficients nearly matches for all propagation distances. From the correlation coefficient calculations, we can infer that GSMV beams of higher topological charges are better suited for communication applications where the turbulence is weak, and the propagation distances are relatively larger.

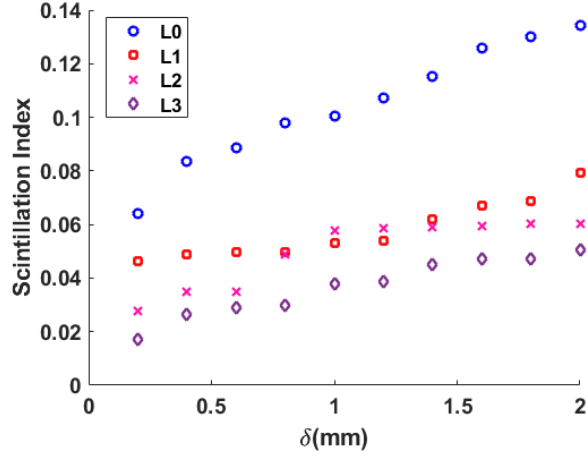


Figure. 5. 8 coherence length vs Scintillation index corresponding to GSMV beams of different orders.

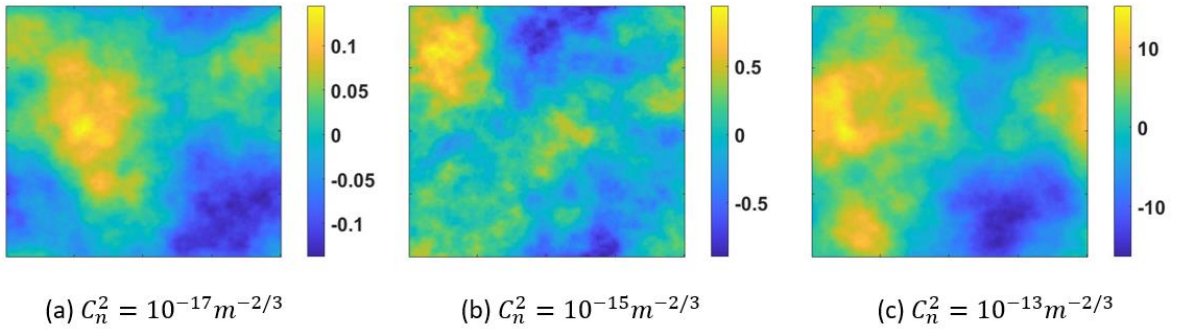


Figure. 5. 9(a-c) show the simulated phase screens of increasing turbulence strength. The colorbar is in radians.

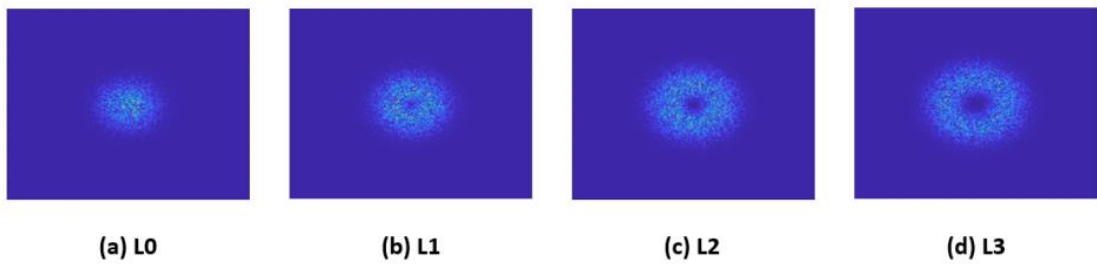
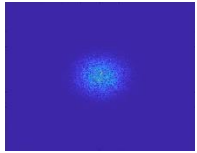
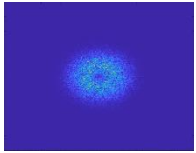
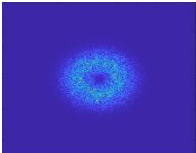
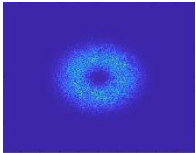
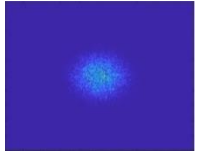
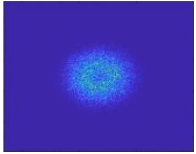
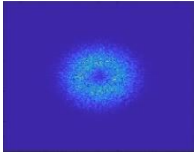
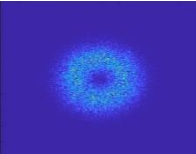
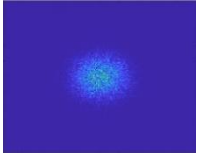
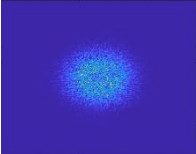
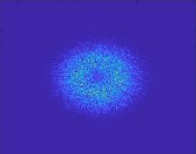
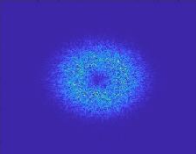
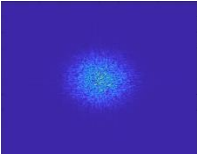
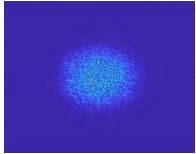
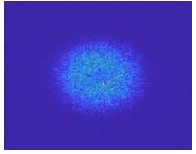
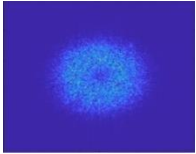
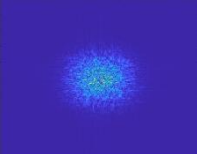
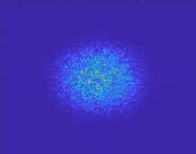
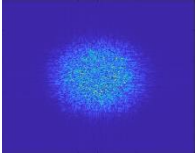
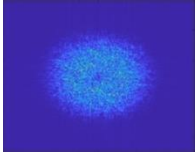
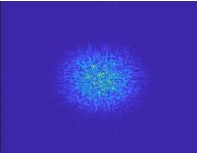
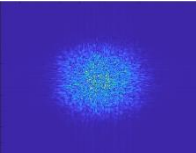
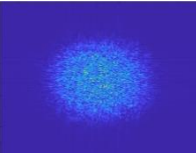
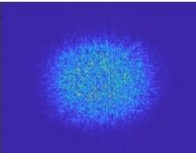


Figure. 5. 10(a-d) show the GSMV beams of different topological charges zero to three.

Table 5. 1 Turbulence impacted GSMV beams of topological charges zero to three for different propagation regions for $C_n^2 = 10^{-17} \text{m}^{-2/3}$.

Propagation (m)	L0	L1	L2	L3
250				
500				
750				
1000				
1250				
1500				

As mentioned earlier, the scintillation index is the most important parameter that quantifies the impact of turbulence. To verify our simulation results and to extend our experimental analysis, we have calculated the scintillation index of turbulence impacted beams in different propagation regions. The calculation is repeated for different turbulence strengths and the results are shown in Fig. 5.12.

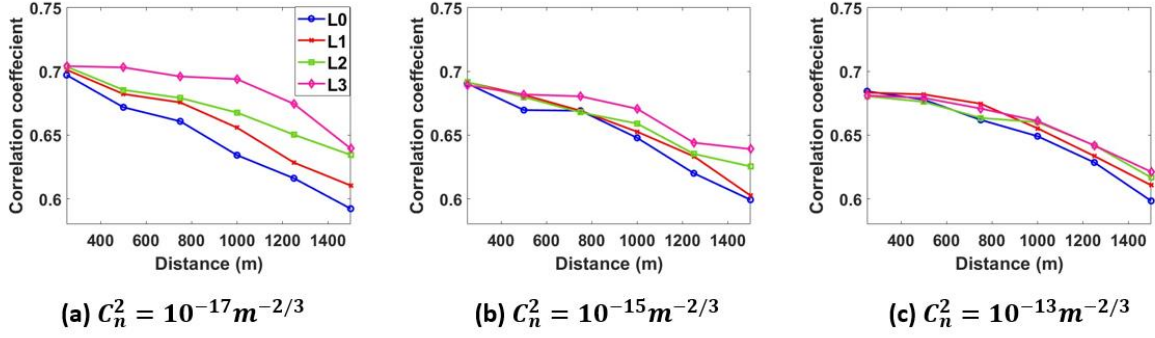


Figure. 5. 11 (a-c) show the correlation vs distance plot for different turbulent strength.

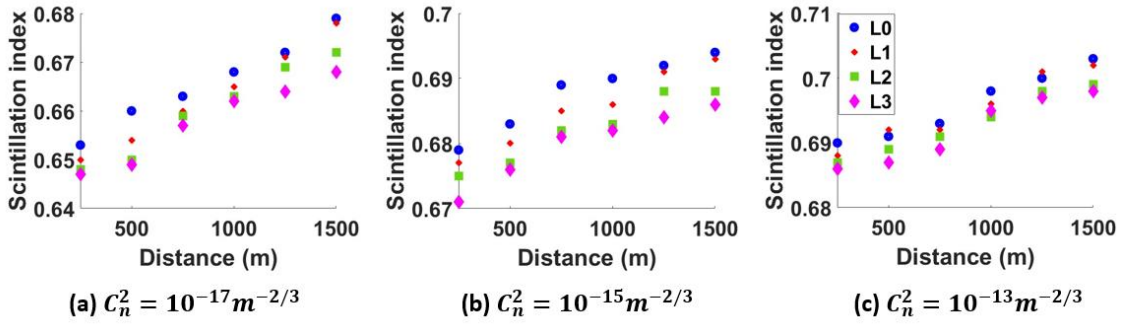


Figure. 5. 12(a-c) shows the scintillation index vs distance for turbulence impacted beams of topological charge zero to three for different turbulence strengths.

From Fig. 5.12 it is evident that scintillation index corresponding to beams carrying higher order topological charges are less compared to their lower order counterparts. The difference is clearer for weak to moderate turbulence strengths. When it comes to stronger turbulence, the scintillation index nearly coincides for all the beams. This is exactly as predicted by the correlation coefficient estimations. This again confirms the fact that GSMV vortex beams of higher order topological charges are a promising candidate for FSO communication systems when the turbulence is weak to moderate.

5.5 Conclusion

In this chapter, we generated GSMV beams of different orders and are passed through a dynamic transmissive Kolmogorov turbulence simulator. Scintillation index, intensity line profiles and correlation coefficients are found for different coherence regimes. It has been experimentally verified that GSMV beams of higher orders show less scintillation, and their resilience decreases as we increase the coherence width. One important result of our experiment is shown in Fig.5.3 which clearly shows the ability of GSMV beams of higher orders to retain their shape even after passing through dynamic turbulence. The robustness of

higher order GSMV beams is further confirmed by the intensity line profiles shown in Fig.5.4 to Fig.5.7. This is the first time in the literature the effect of dynamic Kolmogorov turbulence on GSMV beams in different coherence regimes has been experimentally investigated and verified. The experimental results are further verified by extending the turbulence strength and propagation distances to the actual atmospheric turbulence scales using simulations. These results find applications in free-space communications because of the resemblance of experimental and simulation conditions to the actual atmospheric turbulence.

CHAPTER 6

ENHANCED BACKSCATTERING THROUGH TURBULENCE

6.1 Introduction

Most of the phenomena associated with the atmospheric turbulence are detrimental to the data transmission. However, there are still some phenomena which mitigate the adverse effect of the beam propagation through turbulence. One such phenomenon is called the enhanced backscattering (EBS)[19,99–104]. It arises due to the fine coherence effects caused by a double passage of waves through the same medium inhomogeneities. These effects cause the scattered beams to be ordered rather than degraded. The EBS effect is often observed when the beam is reflected from a retro reflector. The EBS is seen as bright spot near the optic axis, which has a relatively high intensity patch compared to the rest of the beam. The direct and the reflected waves are ideally phase-conjugated, and the effect turbulence is eliminated. Through EBS the FSO system shows higher robustness and has been experimentally investigated elsewhere[102–110]. The double passage problems through the turbulence have got much attention recently because of the modulating reflector technology in free space communication systems. The EBS phenomenon may be utilised to adjust the quality of a beam on a target. The intensity at the focal point of the lens is indicative of the beam quality at the target plane due to the channel's reciprocity. The EBS signal, in conjunction with adaptive optics, can be used to reduce the impacts of turbulence on the bit-error-rate or beam profile in free-space optics communication systems or directed energy applications. However, there are certain challenges to observe EBS. Averaging the received intensity profile across several double passes with uncorrelated turbulence between each double pass is possible only with by standard detection algorithms. This produces two issues: a delay in detecting the EBS signal and, when detected, the EBS signal does not match the current status of the turbulent channel. Furthermore, for objects resembling mirrors or diffuse reflectors, considerable turbulence is required for detection of EBS.

The experimental investigations on the EBS phenomenon were so far limited to a very few classes of beams and relatively weaker turbulence regimes. One such article verifies the enhanced backscattering effect on LG beams [111] and there is an article which explores the effect of double passage through turbulence on partially coherent LG beams[96]. There is another comprehensive study on GSM beams[104]. They study statistical properties such as average intensity, beam wander, intensity probability density function and scintillation index using double-pass, monostatic turbulence channels, both experimentally and numerically. Their experimental findings show that the EBS steadily reduces as the spatial coherence of the GSM source falls, finally disappearing for sufficiently low source spatial coherence states.

Here in this chapter, we present the wave propagation analysis on the effect of double passage of Gaussian vortex beams with even topological charges and Bessel-Gaussian beam through a slowly rotating phase plate (PRPP) in the Kolmogorov regime. The enhanced backscattering is observed under certain conditions. The effect of random phase plate on these beams are further characterised by calculating scintillation index which gives a quantitative measure of the turbulence impact. These results can be utilised in satellite

communications and LIDAR systems. And it finds applications in remote sensing, imaging through turbulence, study of wave propagation through oceanic turbulence and tracking objects in the atmosphere.

6.2 Theoretical Description of EBS

When a wave travels through a phase screen and is reflected back through it, the effect of the second pass can produce a radically different phenomenon. This effect amplifies the backscattered wave caused by the screen's refractive deviations being correlated with the wave. There are two distinct ways that can enhance backscatter: coherent and incoherent. The coherent mechanism is the constructive interference of reflected wave parts after they have passed through different refractive inhomogeneities. When the mirror is placed considerably beyond the phase screen, this is the primary contributing mechanism to the backscatter. When a component of the reflected wave travels through the same refractive inhomogeneity that focussed this component of the wave onto the mirror, the incoherent process occurs.

Consider a uniform plane wavefront containing rays E_1, E_2, E_3 , and E_4 . Till it reaches the phase screen P they follow the parallel direction and upon the incidence to the phase screen they emerge in random directions as shown in Fig. 6.1. These scattered rays are then reflected back to the phase screen. Assume that the ray E_1 is reflected and scattered back into the position which the ray E_4 had already followed, but in the opposite direction. Then the two rays swap places and exit parallel to each other. Due to the scattering mechanism, these two rays depart with no phase difference because they travelled the same path but in opposing directions. This pairing of returning rays will occur in successive realisations anytime any ray may be scattered back towards the direction of the incident wave[112].

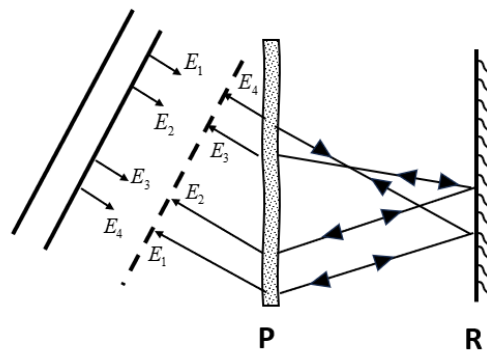


Figure 6. 1 Ray model of double passage through the phase screen P using the reflector R .

Mathematically the total field associated with the beam can be expressed as,

$$E = E_1 + E_2 + E_3 + E_4 \quad (6.1)$$

Then the intensity is given by,

$$\begin{aligned} I &= |E|^2 \\ &= |E_1|^2 + |E_2|^2 + |E_3|^2 + |E_4|^2 + 2E_1E_2 \cos \theta_{12} + \\ &\quad 2E_1E_3 \cos \theta_{13} + 2E_1E_4 \cos \theta_{14} + 2E_2E_3 \cos \theta_{23} \end{aligned} \quad (6.2)$$

If we assume the wave has a uniform intensity such that,

$$I_0 = |E_1|^2 = |E_2|^2 = |E_3|^2 = |E_4|^2 \quad (6.3)$$

Then the total intensity becomes,

$$I = 4I_0 + 2I_0(\cos \theta_{12} + \cos \theta_{13} + \cos \theta_{14} + \cos \theta_{23}) \quad (6.4)$$

Because of the existence of reciprocity, $\theta_{14} = \theta_{23} = 0$. Then the equation 6.4 becomes,

$$I = 4I_0 + 2I_0(\cos \theta_{12} + \cos \theta_{13} + 2) \quad (6.5)$$

When we average over many realizations,

$$\langle I \rangle = 4I_0 + 2I_0(\langle \cos \theta_{12} \rangle + \langle \cos \theta_{13} \rangle + 2) \quad (6.6)$$

Here $\langle \cos \theta_{12} \rangle$ and $\langle \cos \theta_{13} \rangle$ are zero because all phase variations in directions other than the incident wave are random. Then,

$$\begin{aligned} \langle I \rangle &= 4I_0 + (2I_0 + 2I_0) \\ &= \text{incoherent portion} + \text{coherent portion} \end{aligned} \quad (6.7)$$

With a few more assumptions Jakeman developed an equation for the backscattered wave's far-field intensity distribution[106]. He demonstrated that the intensity of backscattered light gets enhanced in the direction of the incident beam. Gaussian speckle will occur at the mirror if it is situated sufficiently enough away from the screen. In this situation, it was demonstrated that the average angularly distributed intensity of a Gaussian beam attains the form,

$$I(\theta_b) = I_b^2 \exp\left(\frac{-2P^2}{n_0^2}\right) \times \left[1 + \frac{\omega_0^2}{\omega_0^2 + zn_0^2} \exp(-2k^2 m^2 Q^2)^{1/2}\right] \quad (6.8)$$

Here I_b^2 is the peak intensity of the backscattered beam, z is the distance between screen and the reflector, n_0 represents the rms value of the sine of the scattering angle of the phase screen, and finally the term zn_0^2 is proportional to the area of the scattering disk at the screen on the second pass. Other terms in the equation are defined as,

$$m^{-2} = \omega_0^{-2} + (zn_0)^{-2} \quad (6.9)$$

$$\begin{aligned} P &= \frac{1}{2}(\sin \theta_b + \sin \theta_i) \\ Q &= \frac{1}{2}(\sin \theta_b - \sin \theta_i) \end{aligned} \quad (6.10)$$

Where θ_b is the observed scattering angle and θ_i is the angle of incidence. For a plane wave with $\omega_0 \gg zn_0$ the Eqn. 6.8 attains the form,

$$I(\theta_b) = I_b^2 \exp\left(\frac{-2P^2}{n_0^2}\right) \left[1 + \exp(-2k^2 m^2 Q^2)^{1/2}\right] \quad (6.11)$$

The first exponential factor describes the intensity angular distribution, and the intensity-enhancement distribution is described by the exponential term included in brackets.

6.3 Experimental

The experimental schemes employed are as shown in Fig. 6.2 and 6.3. In the first experiment, light from a He-Ne laser of wavelength 633nm is spatially filtered and collimated using a lens L1 of focal length of 50mm. The collimated laser beam further passes through a vortex phase plate (RC Photonics) to generate a topologically charged beam. The laser beam is passed through different regions of the phase plate so as to produce vortex beams of charges zero, two and four. These beams are subsequently split into two beams with the use of a beam splitter. One part of the beam is blocked using an opaque screen and the other half is passed through the PRPP and which eventually reflected back using a reflector. In the first case a mirror is used for a conventional Gaussian beam (zero topological charge) as the reflector and throughout the rest of the experiment it is replaced by a retroreflector. The reflected beam again passes through the PRPP and is focussed onto the screen using the lens L2. Here the focal length of the lens L2 is 20cm and the CCD is placed at a distance of 18cm from the lens. Here the detector is not placed at the focal plane because of the imperfections in the retroreflector which would cause the unwanted scatter light to be focussed on the focal plane. The PRPP was rotated during the entire process at the minimum speed so that the incoming and reflected waves undergoes the same phase perturbation. A thousand images are recorded which are further processed in MATLAB to find out the average intensity, intensity line profiles and scintillation index.

Similarly, in the second experiment the collimated beam is passed through an axicon of opening angle on degree so as to produce a BG beam. This BG beam is further passed through a beam splitter. The rest of the experimental set up was as mentioned above. Here again a thousand images are captured for analysis.

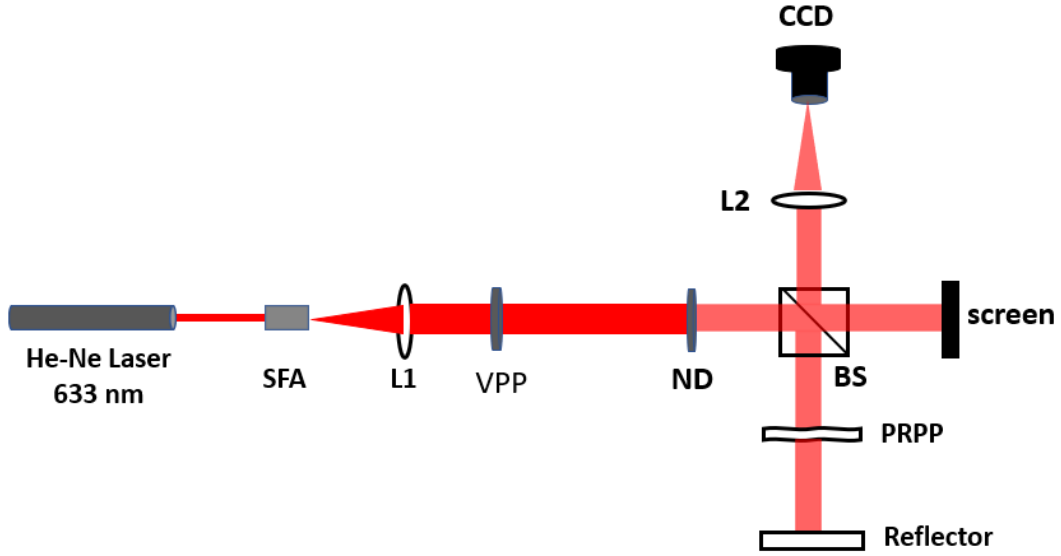


Figure 6. 2 Schematic of experimental set up for double passage of Gaussian vortex beams through the PRPP where SFA denotes the spatial filter assembly and L is the collimating lens. VPP is the vortex phase and PRPP is the pseudo-random phase plate, ND denotes a neutral density filter while BS is a beamsplitter. L2 is the focusing lens and CCD is the camera used for recording images. Here the reflector is initially a mirror and then replaced by a retroreflector.

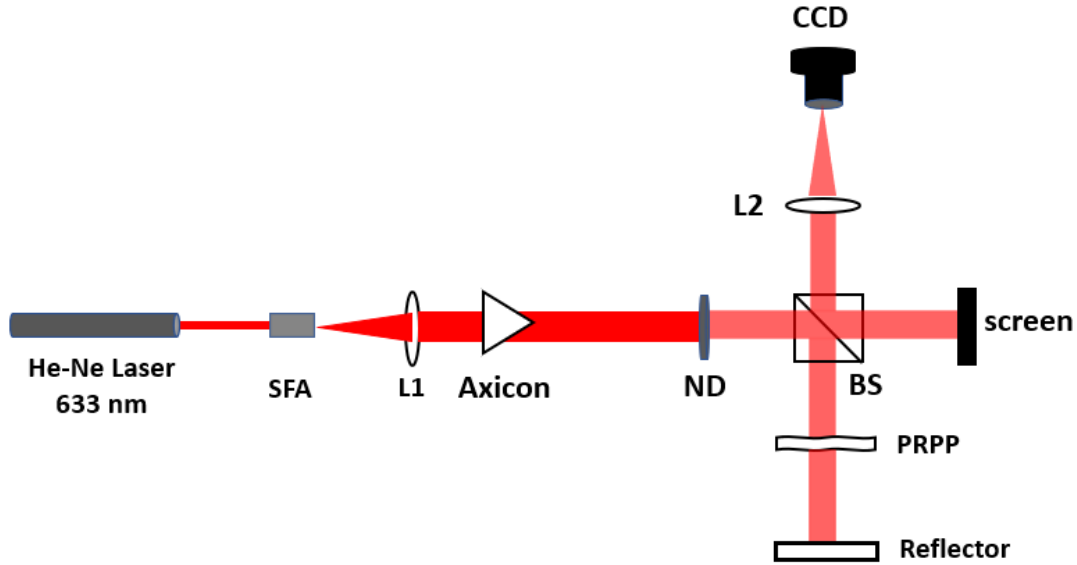


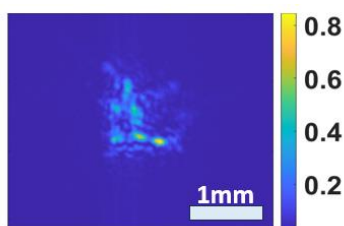
Figure 6. 3 Schematic of experimental set up for double passage of BG beams through the PRPP where SFA denotes the spatial filter assembly and L is the collimating lens. PRPP is the pseudo-random phase plate, ND denotes a neutral density filter while BS is a beamsplitter. L2 is the focusing lens and CCD is the camera used for recording images. Here the reflector is initially a mirror and then replaced by a retroreflector.

6.4 Results and Discussion

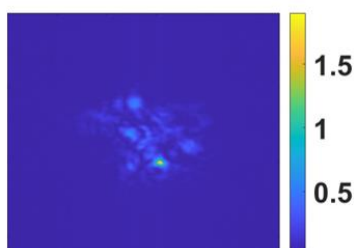
It has been experimentally verified earlier that only the vortex beams having even topological charges exhibit enhanced backscattering[111]. Hence, we limit our experiment to beams with even topological charges. Average intensity captured using the CCD for the backscattered beams are shown in Fig 6.4.

From the Fig.6.4 one can clearly observe the existence of enhancement in the intensity of backscattered beam when reflected from a retroreflector. The average normalised intensity reaches a value around two for conventional Gaussian beam and the value decreases as we increase the topological charge of the vortex beam. Similarly enhanced backscattering is observed for BG beam reflected from a retroreflector. This is the first time in literature , the enhanced backscattering of BG beam is reported. And this altogether the first time the enhanced backscattering using a rotating phasescreen is observed and reported. Another important thing to notice here is the resemblance of ring-shaped BG beams to the incident beam. It clearly shows the resilience of BG beam even after impacted by the strong turbulence twice.

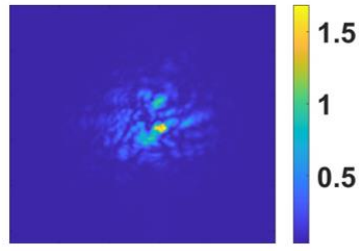
Furthermore, the intensity line profiles are plotted and are shown in Fig. 6.5. In order to clearly observe the enhanced backscattering only the intensity near to the peak is shown.



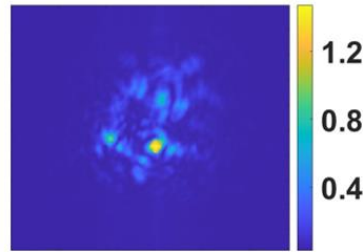
(a) LO (mirror)



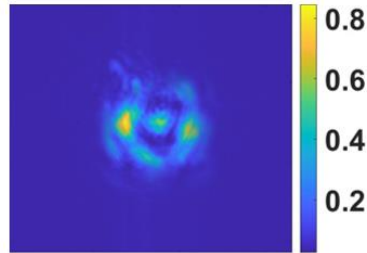
(b) LO (RR)



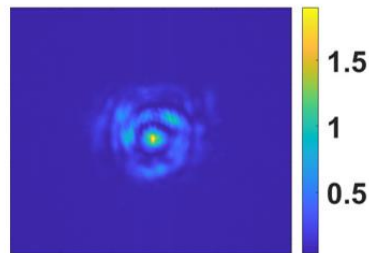
(c) L2 (RR)



(d) L4 (RR)

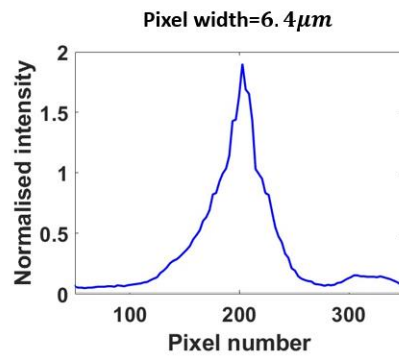


(e) BG (mirror)

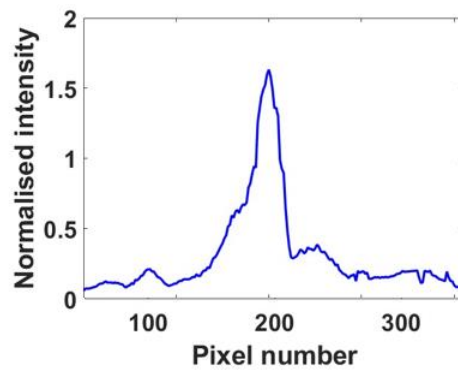


(f) BG (RR)

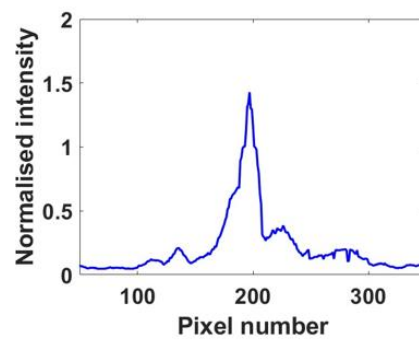
Figure 6. 4 (a) shows the average intensity obtained at the CCD plane when the conventional Gaussian beam was reflected from a mirror, while (b) shows the backscattered beam after reflecting from a retroreflector (RR). (c) and (d) are the respectively the backscattered Gaussian vortex beams of charges two and four from a retroreflector. (e) and (f) show the backscattered beam from a mirror and retroreflector respectively.



(a) L0



(b) L2



(c) L4

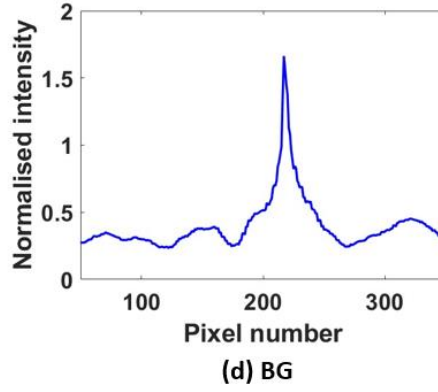


Figure 6. 5 shows the intensity line profiles of backscattered beams. (a)-(c) show the line profiles corresponding to Gaussian vortex beams respectively having charges zero, two and four. (d) shows the intensity line profile of backscattered BG beam.

It can be observed that there is an enhancement of average intensity in the backscattered beams. The maximum intensity reflected by the flat mirror is used to normalise the average intensity pattern. The enhancement factors for different beams are plotted in Fig. 6.6.

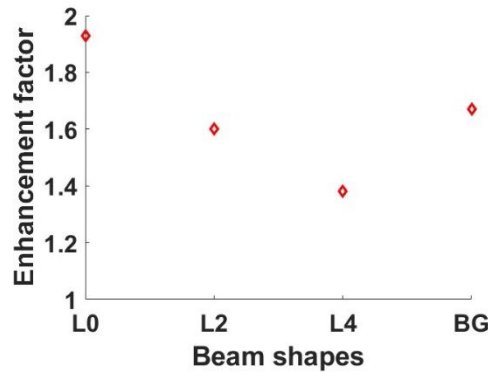


Figure 6. 6 shows the enhancement factor for different beam shapes. L0 denote Gaussian beam, L2 and L4 denote Gaussian vortex beams having topological charges two and four respectively. BG means the Bessel-Gaussian beam generated using an axicon of opening angle one degree.

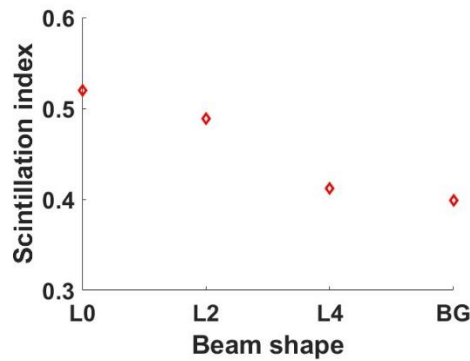


Figure 6. 7 shows the scintillation index for different beam shapes. L0 denotes Gaussian beam, L2 and L4 denote Gaussian vortex beams having topological charges two and four respectively. BG means the Bessel-Gaussian beam generated using an axicon of opening angle one degree.

In order to estimate the effect of dynamic turbulence on backscattered beams the scintillation index is calculated and plotted in Fig. 6.7.

The values of enhancement factor , scintillation index and their percentage variation from the values corresponding to the conventional Gaussian beam are tabulated in Table 6.1.

Table 6. 1The values of enhancement factor , scintillation index and their percentage variation from the values corresponding to the conventional Gaussian beam.

Beam shape	Enhancement factor	Percentage reduction	Scintillation index	Percentage reduction
L0	1.978	00.00	0.520	00.00
L2	1.599	19.16	0.489	05.96
L4	1.386	29.92	0.412	20.76
BG	1.645	16.84	0.399	23.27

From the table we can draw the conclusion that even though there is highest enhancement factor observed for Gaussian beam it has got the maximum value for scintillation index as well implying that the enhanced backscattering does not ensure better resilience to the turbulence impact. Hence for free space communication purposes and target tracking we need to have a trade-off between maximum intensity and intensity fluctuations. Looking at the table one can see that considering the enhancement factor as well as the scintillation index BG beams proves to be a better candidate for communication systems involving double passage through the turbulence. It has got a fairly high enhancement factor and the lowest value of scintillation index. This is the first time in literature the phenomenon along with the robustness of beams to the impact of turbulence is simultaneously studied for double passage problems. Again, this is the first time observing the enhanced backscattering effect with BG beams. These results can be used to develop a communication system where the transmitting beams will be more resilient to the atmospheric degradation thereby minimising the use of adaptive optics systems.

6.5 Conclusion

In the present chapter we generated Gaussian vortex beams using a vortex phase plate and a BG beam using an axicon. The generated beams are passed through a rotating dynamic turbulence twice and focussed onto a detector. The backscattered beams after passing through the PRPP are thoroughly analysed. Enhanced backscattering is observed when the beam is reflected from a retroreflector. The amplification factor reaches a value close to two as we use conventional Gaussian beam, and the value reduces as we increase the topological charge. The enhanced backscattering is observed for BG beam also with an enhancement factor of 1.645. Along with the enhanced backscatter, it can be seen that the resilience of the BG beams is preserved comparing to the other incident beams. The resilience is further verified by the scintillation index calculations. We can make use of these results to the actual ground to satellite to ground communication systems.

CHAPTER 7

CONCLUSION AND FUTURE SCOPE

7.1 Conclusions

The primary objective of the thesis was to investigate the effect of dynamic Kolmogorov kind of turbulence on different structured beams for employing them on FSO communication systems. Different classes of beams have been quantitatively and qualitatively optimised. Certain classes of beams in different coherence regimes and different spatial structures are found to be more resilient to the impact of turbulence compared to the conventional Gaussian beams making them a better choice to be used in free space communication purposes.

- The thesis starts with the characterization of turbulent simulator, the PRPP, which has been used throughout our investigations. In that chapter, we suggest a simple approach for determining the Fried parameter of a dynamic turbulence simulator at the laboratory level. The Fried coherence length was calculated using a unique approach. In a two-dimensional phase map created from a Mach-Zehnder interferometer, we used the autocorrelation function of a single point to estimate the Fried parameter of the PRPP. In contrast to the previously described characterisation procedures, this method is simple, employs a basic experimental setup, and produces higher precision.
- Next, we used two distinct techniques to simulate Gaussian Schell model beams. In two separate experimental approaches, simulated beams with gradually varying coherence lengths were passed through a dynamic transmissive Kolmogorov turbulence simulator. For each experimental condition, the scintillation index, beam wander, and Zernike polynomials were determined. It is possible to infer that partially coherent beams are more effective for free space optical communications. It becomes apparent that the robustness of partly coherent beams is more under weaker turbulence.
- Further, we analysed the impact of a rotating turbulence BG beams. In this chapter, we successfully produced BG beams using simulations and axicons. A dynamic transmissive Kolmogorov turbulence simulator is used to study the effect on these BG beams and standard Gaussian beams. For various axicon angles in the Fresnel, Fourier, and Fraunhofer regions, the scintillation index, beam wander, and intensity line profiles are determined. We discovered that, as compared to Gaussian beams, BG beams had a substantially lower scintillation index in the Fourier and Fraunhofer regions. When it comes to beam wandering in both the x and y axes, BG beams outperform laser Gaussian beams. One of the primary findings of our experiment is that BG beams may keep their form even after travelling through dynamic turbulence. The influence of dynamic turbulence on BG beams is explored for the first time in the literature. There is a strong match between experimental and simulation findings, confirming the insensitivity of BG beams to the influence of dynamic turbulence as compared to ordinary Gaussian beams.
- The work continued to analyse the impact of PRPP on Gaussian Schell model vortex beams. We created GSMV beams of various orders, which then passed through a dynamic transmissive Kolmogorov turbulence model. For various coherence regimes, the scintillation index, intensity line profiles, and correlation coefficients are

calculated. It has been experimentally demonstrated that GSMV beams of higher orders exhibit less scintillation, and their robustness reduces as the coherence width increases. One significant outcome of our experiment clearly demonstrates the capacity of higher order GSMV beams to preserve their form even after travelling through dynamic turbulence. The intensity line profiles further support the resilience of higher order GSMV beams. The influence of dynamic Kolmogorov turbulence on GSMV beams in different coherence regimes has been experimentally explored and proven for the first time in the literature. The experimental results are further validated by employing simulations to extend the turbulence strength and propagation lengths to the real atmospheric turbulence scales.

- The final part of the thesis deals with the phenomenon of enhanced backscattering through turbulence. We used a vortex phase plate to create Gaussian vortex beams and an axicon to generate BG beams. The produced beams are focused onto a detector after passing through a rotating dynamic turbulence twice. The backscattered rays are examined using a CCD . When a beam is reflected off a retroreflector, it exhibits enhanced backscattering. When we employ a typical Gaussian beam, the amplification factor approaches two, and it decreases as the topological charge increases. The BG beam also exhibits enhanced backscattering, with an enhancement factor of 1.645. Along with the increased backscatter, the endurance of the BG beams is preserved as compared to the other incident beams.

Our experimental investigations suggest that certain classes of beams are better candidates compared to the conventional Gaussian beams when used as transmitting beams in FSO communication channels. When we solely consider the coherence factor of the transmitting beams and their resilience, it was shown that for weak to moderate turbulence levels, partially coherent beams with smaller coherence width outperforms their fully coherent counter parts. When we consider the spatial structure of the transmitting beams as well, Gaussian Schell model beams with vortex phases and BG beams show more robustness compared to the normal Gaussian beam. If we quantitatively compare the effect of turbulence on BG beams and Gaussian Schell model vortex beams, the former outperforms the latter in terms of scintillation index for shorter propagation distances. However, according to our simulation studies, which resemble to the actual atmospheric turbulence parameters, predict that BG beams are not a better choice for long distance communications. The resilience of BG beams is lost in less than a few kilometres even under a very weak turbulence.

When considering the double passage through the same turbulence an enhancement in intensity is observed for Gaussian beams, GSMV beams and BG beams. We may conclude that, while the Gaussian beam has the largest enhancement factor, it also has the highest scintillation index, showing that increased backscattering does not guarantee superior resilience to turbulence influence. As a result, for free space communication and target tracking, we must make a trade-off between maximum intensity and intensity fluctuations. When both the enhancement factor and the scintillation index are considered, BG beams are a superior choice for communication systems including double transit through turbulence. It has a relatively high amplification factor and the lowest scintillation index value.

7.2 Future Perspectives

The following session outlines the possible future directions of the present work.

- There are infinite possible structured beams which can be digitally created and propagated. We can extend our studies by incorporating more structured light beams to our turbulence analysis.
- Another way of extending the investigation is by incorporating the vector nature of the optical fields. We can explore the effect of polarization on the turbulence impacted light beams.
- Our current work is limited to Kolmogorov kind of turbulence. There are other turbulence models which might have different kinds of impact on the propagating light beams.
- The most important future direction of the investigation is validating our experimental investigations to the actual FSO communication systems with data encryption and decryption.

REFERENCES

- [1] G. Gbur, Partially coherent beam propagation in atmospheric turbulence [Invited], *J. Opt. Soc. Am. A* 31 (2014) 2038. <https://doi.org/10.1364/JOSAA.31.002038>.
- [2] R.K. Tyson, *Principles of adaptive optics*, 2nd ed, Academic Press, Boston, 1998.
- [3] J.W. Strohbehn, *Laser Beam Propagation in the Atmosphere*, Springer-Verlag Springer e-books, Berlin, Heidelberg, 2005.
- [4] Dissipation of energy in the locally isotropic turbulence, *Proc. R. Soc. Lond. A* 434 (1991) 15–17. <https://doi.org/10.1098/rspa.1991.0076>.
- [5] J.C. Leader, Intensity fluctuations resulting from partially coherent light propagating through atmospheric turbulence, *J. Opt. Soc. Am.* 69 (1979) 73. <https://doi.org/10.1364/JOSA.69.000073>.
- [6] H. Willebrand, B.S. Ghuman, *Free space optics: enabling optical connectivity in today's networks*, SAMS, Indianapolis, Ind, 2002.
- [7] T.H. Carbonneau, D.R. Wisely, Opportunities and challenges for optical wireless: the competitive advantage of free space telecommunications links in today's crowded marketplace, in: P. Christopher, L. Langston, G.S. Mecherle (Eds.), *Dallas, TX*, 1998: p. 119. <https://doi.org/10.1117/12.301022>.
- [8] K. Tsukamoto, A. Hashimoto, Y. Aburakawa, M. Matsumoto, The case for free space, *IEEE Microwave* 10 (2009) 84–92. <https://doi.org/10.1109/MMM.2009.933086>.
- [9] A. Mahdy, J.S. Deogun, Wireless optical communications: a survey, in: *2004 IEEE Wireless Communications and Networking Conference (IEEE Cat. No.04TH8733)*, IEEE, Atlanta, GA, USA, 2004: pp. 2399–2404. <https://doi.org/10.1109/WCNC.2004.1311464>.
- [10] H. Izadpanah, T. ElBatt, V. Kukshya, F. Dolezal, B.K. Ryu, High-availability free space optical and RF hybrid wireless networks, *IEEE Wireless Commun.* 10 (2003) 45–53. <https://doi.org/10.1109/MWC.2003.1196402>.
- [11] H. Kaushal, V.K. Jain, S. Kar, *Free Space Optical Communication*, 1st ed. 2017, Springer India : Imprint: Springer, New Delhi, 2017. <https://doi.org/10.1007/978-81-322-3691-7>.
- [12] T. Siegel, S.-P. Chen, Investigations of Free Space Optical Communications Under Real-World Atmospheric Conditions, *Wireless Pers Commun* 116 (2021) 475–490. <https://doi.org/10.1007/s11277-020-07724-1>.
- [13] H. Weichel, *Laser beam propagation in the atmosphere*, SPIE Optical Engineering Press, Bellingham, Wash., USA, 1990.
- [14] R.S. Lawrence, J.W. Strohbehn, A survey of clear-air propagation effects relevant to optical communications, *Proc. IEEE* 58 (1970) 1523–1545. <https://doi.org/10.1109/PROC.1970.7977>.
- [15] R.F. Lutomirski, H.T. Yura, Propagation of a Finite Optical Beam in an Inhomogeneous Medium, *Appl. Opt.* 10 (1971) 1652. <https://doi.org/10.1364/AO.10.001652>.
- [16] A.M. Prokhorov, F.V. Bunkin, K.S. Gochelashvily, V.I. Shishov, Laser irradiance propagation in turbulent media, *Proc. IEEE* 63 (1975) 790–811. <https://doi.org/10.1109/PROC.1975.9828>.
- [17] R.L. Fante, Electromagnetic beam propagation in turbulent media, *Proc. IEEE* 63 (1975) 1669–1692. <https://doi.org/10.1109/PROC.1975.10035>.
- [18] R.L. Fante, Electromagnetic beam propagation in turbulent media: An update, *Proc. IEEE* 68 (1980) 1424–1443. <https://doi.org/10.1109/PROC.1980.11882>.
- [19] A. Ishimaru, *Wave Propagation and Scattering in Random Media*, IEEE, 1999. <https://doi.org/10.1109/9780470547045>.
- [20] A.D. Wheelon, *Electromagnetic Scintillation*, 1st ed., Cambridge University Press, 2003. <https://doi.org/10.1017/CBO9780511534812>.

- [21] M.A. Cox, N. Mphuthi, I. Nape, N.P. Mashaba, L. Cheng, A. Forbes, Structured Light in Turbulence, (2020). <https://doi.org/10.48550/ARXIV.2005.14586>.
- [22] J.D. Schmidt, Numerical simulation of optical wave propagation with examples in MATLAB, SPIE, Bellingham, Wash, 2010.
- [23] P.D. Mier, J.J. van den Hurk, Lysosomal hydrolases of the epidermis. I. Glycosidases, *Br J Dermatol* 93 (1975) 1–10. <https://doi.org/10.1111/j.1365-2133.1975.tb06468.x>.
- [24] R.J. Sasiela, Electromagnetic wave propagation in turbulence: evaluation and application of Mellin transforms, 2. ed, SPIE, Bellingham, Wash, 2007.
- [25] D.L. Fried, Statistics of a Geometric Representation of Wavefront Distortion, *J. Opt. Soc. Am.* 55 (1965) 1427. <https://doi.org/10.1364/JOSA.55.001427>.
- [26] J.C. Gutiérrez-Vega, M.A. Bandres, Ince–Gaussian beams in a quadratic-index medium, *J. Opt. Soc. Am. A* 22 (2005) 306. <https://doi.org/10.1364/JOSAA.22.000306>.
- [27] M.W. Hyde, Independently Controlling Stochastic Field Realization Magnitude and Phase Statistics for the Construction of Novel Partially Coherent Sources, *Photonics* 8 (2021) 60. <https://doi.org/10.3390/photonics8020060>.
- [28] F. Gori, M. Santarsiero, Devising genuine spatial correlation functions, *Opt. Lett.* 32 (2007) 3531. <https://doi.org/10.1364/OL.32.003531>.
- [29] E. Wolf, Introduction to the theory of coherence and polarization of light, Cambridge University Press, Cambridge, 2007.
- [30] A. Dixit, V. Porwal, A. Kumar, S.K. Mishra, Systematic Characterization of Near-Index-Matched Optics Based Atmospheric Turbulence Simulator, *MAPAN* 35 (2020) 221–232. <https://doi.org/10.1007/s12647-020-00370-9>.
- [31] S.V. Mantravadi, T.A. Rhoadarmer, R.S. Glas, Simple laboratory system for generating well-controlled atmospheric-like turbulence, in: J.D. Gonglewski, M.T. Gruneisen, M.K. Giles (Eds.), Denver, CO, 2004: p. 290. <https://doi.org/10.1117/12.559933>.
- [32] S.M. Ebstein, Pseudo-random phase plates, in: J.D. Gonglewski, M.A. Vorontsov, M.T. Gruneisen (Eds.), San Diego, CA, 2002: pp. 150–155. <https://doi.org/10.1117/12.454707>.
- [33] R. Sharma, C.S. Narayanamurthy, Characterization of Pseudo-Random-Phase-Plate as a Kolmogorov/non-Kolmogorov turbulence simulator using statistical parameters and the phase structure function, *J Opt* 45 (2016) 58–65. <https://doi.org/10.1007/s12596-015-0263-8>.
- [34] R. Sharma, C.S. Narayanamurthy, Single and double passage interferometric analysis of Pseudo-Random-Phase-Plates, *Optics Communications* 345 (2015) 37–46. <https://doi.org/10.1016/j.optcom.2015.01.064>.
- [35] D.E. Novoseller, Coherence length evaluation for linear propagation of radiation through a turbulent medium, *Appl. Opt.* 19 (1980) 352. <https://doi.org/10.1364/AO.19.000352>.
- [36] J. Vernin, C. Munoz-Tunon, Measuring astronomical seeing: The DA/IAC DIMM, *PASP* 107 (1995) 265. <https://doi.org/10.1086/133549>.
- [37] F.D. Eaton, J.R. Hines, J.J. Drexler, D.B. Soules, Short term variability of atmospheric turbidity and optical turbulence in a desert environment, *Theor Appl Climatol* 56 (1997) 67–81. <https://doi.org/10.1007/BF00863784>.
- [38] S. Horst, C.J. Radosevich, C.J. Pellizzari, M.F. Spencer, Measuring the Fried parameter of transmissive phase screens using digital-holographic detection, in: J.J. Dolne, M.F. Spencer, M.E. Testorf (Eds.), Unconventional and Indirect Imaging, Image Reconstruction, and Wavefront Sensing 2019, SPIE, San Diego, United States, 2019: p. 13. <https://doi.org/10.1117/12.2529680>.

- [39] F. Wang, I. Toselli, O. Korotkova, Two spatial light modulator system for laboratory simulation of random beam propagation in random media, *Appl. Opt.* 55 (2016) 1112. <https://doi.org/10.1364/AO.55.001112>.
- [40] T.A. Rhoadarmer, J.R.P. Angel, Low-cost, broadband static phase plate for generating atmosphericlike turbulence, *Appl. Opt.* 40 (2001) 2946. <https://doi.org/10.1364/AO.40.002946>.
- [41] E.P. Magee, B.M. Welsh, Characterization of laboratory-generated turbulence by optical phase measurements, in: S.S. Cha, J.D. Trolinger (Eds.), San Diego, CA, 1993: pp. 50–61. <https://doi.org/10.1117/12.163751>.
- [42] L.R. Bissonnette, Atmospheric scintillation of optical and infrared waves: a laboratory simulation, *Appl. Opt.* 16 (1977) 2242. <https://doi.org/10.1364/AO.16.002242>.
- [43] C.C. Davis, Y. Zhang, M.L. Plett, P. Polak-Dingels, P.R. Barbier, D.W. Rush, Characterization of a liquid-filled turbulence simulator, in: J.D. Gonglewski, M.A. Vorontsov (Eds.), San Diego, CA, 1998: pp. 38–49. <https://doi.org/10.1117/12.327986>.
- [44] D.C. Dayton, S.L. Browne, S.P. Sandven, J.D. Gonglewski, A.V. Kudryashov, Theory and laboratory demonstrations on the use of a nematic liquid-crystal phase modulator for controlled turbulence generation and adaptive optics, *Appl. Opt.* 37 (1998) 5579. <https://doi.org/10.1364/AO.37.005579>.
- [45] L. Burger, I. Litvin, A. Forbes, Simulating atmospheric turbulence using a phase-only spatial light modulator, *South African Journal of Science* 104 (2008).
- [46] N.H. Farwell, O. Korotkova, Multiple phase-screen simulation of oceanic beam propagation, in: A.M.J. Van Eijk, C.C. Davis, S.M. Hammel (Eds.), San Diego, California, United States, 2014: p. 922416. <https://doi.org/10.1117/12.2062683>.
- [47] B. Rodenburg, M. Mirhosseini, M. Malik, O.S. Magaña-Loaiza, M. Yanakas, L. Maher, N.K. Steinhoff, G.A. Tyler, R.W. Boyd, Simulating thick atmospheric turbulence in the lab with application to orbital angular momentum communication, *New J. Phys.* 16 (2014) 033020. <https://doi.org/10.1088/1367-2630/16/3/033020>.
- [48] I. Toselli, O. Korotkova, X. Xiao, D.G. Voelz, SLM-based laboratory simulations of Kolmogorov and non-Kolmogorov anisotropic turbulence, *Appl. Opt.* 54 (2015) 4740. <https://doi.org/10.1364/AO.54.004740>.
- [49] M. Takeda, H. Ina, S. Kobayashi, Fourier-transform method of fringe-pattern analysis for computer-based topography and interferometry, *J. Opt. Soc. Am.* 72 (1982) 156. <https://doi.org/10.1364/JOSA.72.000156>.
- [50] J.C. Ricklin, F.M. Davidson, Atmospheric turbulence effects on a partially coherent Gaussian beam: implications for free-space laser communication, *J. Opt. Soc. Am. A* 19 (2002) 1794. <https://doi.org/10.1364/JOSAA.19.001794>.
- [51] V.A. Banakh, V.M. Buldakov, Effect of the initial degree of spatial coherence of a light beam on intensity fluctuations in a turbulent atmosphere, *Optics and Spectroscopy* 55 (1983) 423–426.
- [52] O. Korotkova, Model for a partially coherent Gaussian beam in atmospheric turbulence with application in Lasercom, *Opt. Eng* 43 (2004) 330. <https://doi.org/10.1117/1.1636185>.
- [53] J.C. Ricklin, F.M. Davidson, Atmospheric optical communication with a Gaussian Schell beam, *J. Opt. Soc. Am. A, JOSAA* 20 (2003) 856–866. <https://doi.org/10.1364/JOSAA.20.000856>.
- [54] C. Nelson, S. Avramov-Zamurovic, R. Malek-Madani, O. Korotkova, R. Sova, F. Davidson, Measurements and comparison of the probability density and covariance functions of laser beam intensity fluctuations in a hot-air turbulence emulator with the maritime atmospheric environment, in: A.M.J. Van Eijk, C.C. Davis, S.M. Hammel,

- A.K. Majumdar (Eds.), San Diego, California, USA, 2012: p. 851707. <https://doi.org/10.1117/12.951931>.
- [55] O. KOROTKOVA, RANDOM LIGHT BEAMS: theory and applications, CRC Press, Place of publication not identified, 2019.
 - [56] K.R. Drexler, M.C. Roggemann, Far-field scintillation reduction utilizing Gaussian-Schell model beams, in: Imaging and Applied Optics, OSA, Toronto, 2011: p. LTuD2. <https://doi.org/10.1364/LSC.2011.LTuD2>.
 - [57] T.J. Schulz, Iterative transform algorithm for the computation of optimal beams, J. Opt. Soc. Am. A 21 (2004) 1970. <https://doi.org/10.1364/JOSAA.21.001970>.
 - [58] T.J. Schulz, Optimal beams for propagation through random media, Opt. Lett. 30 (2005) 1093. <https://doi.org/10.1364/OL.30.001093>.
 - [59] M.W. Hyde, Stochastic complex transmittance screens for synthesizing general partially coherent sources, J. Opt. Soc. Am. A 37 (2020) 257. <https://doi.org/10.1364/JOSAA.381772>.
 - [60] F. Wang, H. Lv, Y. Chen, Y. Cai, O. Korotkova, Three modal decompositions of Gaussian Schell-model sources: comparative analysis, Opt. Express 29 (2021) 29676. <https://doi.org/10.1364/OE.435767>.
 - [61] Y. Cai, Y. Chen, F. Wang, Generation and propagation of partially coherent beams with nonconventional correlation functions: a review [Invited], J. Opt. Soc. Am. A 31 (2014) 2083. <https://doi.org/10.1364/JOSAA.31.002083>.
 - [62] D. Voelz, X. Xiao, O. Korotkova, Numerical modeling of Schell-model beams with arbitrary far-field patterns, Opt. Lett. 40 (2015) 352. <https://doi.org/10.1364/OL.40.000352>.
 - [63] S. Basu, M.W. Hyde, X. Xiao, D.G. Voelz, O. Korotkova, Computational approaches for generating electromagnetic Gaussian Schell-model sources, Opt. Express 22 (2014) 31691. <https://doi.org/10.1364/OE.22.031691>.
 - [64] A. Bhattacharjee, R. Sahu, A.K. Jha, Generation of a Gaussian Schell-model field as a mixture of its coherent modes, J. Opt. 21 (2019) 105601. <https://doi.org/10.1088/2040-8986/ab3b24>.
 - [65] M.W. Hyde, S.R. Bose-Pillai, R.A. Wood, Synthesis of non-uniformly correlated partially coherent sources using a deformable mirror, Applied Physics Letters 111 (2017) 101106. <https://doi.org/10.1063/1.4994669>.
 - [66] R. Wang, S. Zhu, Y. Chen, H. Huang, Z. Li, Y. Cai, Experimental synthesis of partially coherent sources, Opt. Lett. 45 (2020) 1874. <https://doi.org/10.1364/OL.388307>.
 - [67] D. Coburn, D. Garnier, J.C. Dainty, A single star SCIDAR system for profiling atmospheric turbulence, in: K. Stein, A. Kohnle (Eds.), Bruges, Belgium, 2005: p. 59810D. <https://doi.org/10.1117/12.627531>.
 - [68] S. Li, J. Wang, Adaptive free-space optical communications through turbulence using self-healing Bessel beams, Sci Rep 7 (2017) 43233. <https://doi.org/10.1038/srep43233>.
 - [69] S. Avramov-Zamurovic, C. Nelson, R. Malek-Madani, O. Korotkova, Polarization-induced reduction in scintillation of optical beams propagating in simulated turbulent atmospheric channels, Waves in Random and Complex Media 24 (2014) 452–462. <https://doi.org/10.1080/17455030.2014.944242>.
 - [70] P. Panchal, D.N. Naik, C.S. Narayanamurthy, Insensitivity of higher order topologically charged Laguerre–Gaussian beams to dynamic turbulence impact, Optics Communications 495 (2021) 127023. <https://doi.org/10.1016/j.optcom.2021.127023>.
 - [71] F. Gori, G. Guattari, C. Padovani, Bessel-Gauss beams, Optics Communications 64 (1987) 491–495. [https://doi.org/10.1016/0030-4018\(87\)90276-8](https://doi.org/10.1016/0030-4018(87)90276-8).
 - [72] J. Durnin, J.J. Miceli, J.H. Eberly, Diffraction-free beams, Phys. Rev. Lett. 58 (1987) 1499–1501. <https://doi.org/10.1103/PhysRevLett.58.1499>.

- [73] R.K. Tyson, ed., *Topics in Adaptive Optics*, InTech, Rijeka, 2012.
- [74] Exact solutions for nondiffracting beams. I. The scalar theory, (n.d.). <https://opg.optica.org/josaa/fulltext.cfm?uri=josaa-4-4-651&id=2714> (accessed October 18, 2022).
- [75] V. Kollarova, T. Medrik, R. Celechovsky, Z. Bouchal, O. Wilfert, Z. Kolka, Application of nondiffracting beams to wireless optical communications, in: E.M. Carapezza (Ed.), Florence, Italy, 2007: p. 67361C. <https://doi.org/10.1117/12.737361>.
- [76] N. Mphuthi, R. Botha, A. Forbes, Are Bessel beams resilient to aberrations and turbulence?, *J. Opt. Soc. Am. A* 35 (2018) 1021. <https://doi.org/10.1364/JOSAA.35.001021>.
- [77] H.T. Eyyuboğlu, Propagation of higher order Bessel–Gaussian beams in turbulence, *Appl. Phys. B* 88 (2007) 259–265. <https://doi.org/10.1007/s00340-007-2707-6>.
- [78] I.P. Lukin, Coherence of Pseudo-Bessel Beams in a Turbulent Atmosphere, *Atmos Ocean Opt* 31 (2018) 590–603. <https://doi.org/10.1134/S1024856019010093>.
- [79] T. Doster, A.T. Watnik, Laguerre–Gauss and Bessel–Gauss beams propagation through turbulence: analysis of channel efficiency, *Appl. Opt.* 55 (2016) 10239. <https://doi.org/10.1364/AO.55.010239>.
- [80] P. Birch, I. Ituen, R. Young, C. Chatwin, Long-distance Bessel beam propagation through Kolmogorov turbulence, *J. Opt. Soc. Am. A* 32 (2015) 2066. <https://doi.org/10.1364/JOSAA.32.002066>.
- [81] W. Nelson, J.P. Palastro, C.C. Davis, P. Sprangle, Propagation of Bessel and Airy beams through atmospheric turbulence, *J. Opt. Soc. Am. A* 31 (2014) 603. <https://doi.org/10.1364/JOSAA.31.000603>.
- [82] C.Z. Çil, H.T. Eyyuboğlu, Y. Baykal, O. Korotkova, Y. Cai, Beam wander of J₀- and I₀-Bessel Gaussian beams propagating in turbulent atmosphere, *Appl. Phys. B* 98 (2010) 195–202. <https://doi.org/10.1007/s00340-009-3724-4>.
- [83] A.E. Willner, Z. Zhao, C. Liu, R. Zhang, H. Song, K. Pang, K. Manukyan, H. Song, X. Su, G. Xie, Y. Ren, Y. Yan, M. Tur, A.F. Molisch, R.W. Boyd, H. Zhou, N. Hu, A. Minoofar, H. Huang, Perspectives on advances in high-capacity, free-space communications using multiplexing of orbital-angular-momentum beams, *APL Photonics* 6 (2021) 030901. <https://doi.org/10.1063/5.0031230>.
- [84] C. López-Mariscal, Observation of the experimental propagation properties of Helmholtz-Gauss beams, *Opt. Eng* 45 (2006) 068001. <https://doi.org/10.1117/1.2210485>.
- [85] S. Li, J. Wang, Adaptive free-space optical communications through turbulence using self-healing Bessel beams, *Sci Rep* 7 (2017) 43233. <https://doi.org/10.1038/srep43233>.
- [86] J.C. Leader, Intensity fluctuations resulting from partially coherent light propagating through atmospheric turbulence, *J. Opt. Soc. Am., JOSA* 69 (1979) 73–84. <https://doi.org/10.1364/JOSA.69.000073>.
- [87] O. Korotkova, Scintillation index of a stochastic electromagnetic beam propagating in random media, *Optics Communications* 281 (2008) 2342–2348. <https://doi.org/10.1016/j.optcom.2007.12.047>.
- [88] Z. Bouchal, Resistance of nondiffracting vortex beam against amplitude and phase perturbations, *Optics Communications* 210 (2002) 155–164. [https://doi.org/10.1016/S0030-4018\(02\)01753-4](https://doi.org/10.1016/S0030-4018(02)01753-4).
- [89] G. Gbur, R.K. Tyson, Vortex beam propagation through atmospheric turbulence and topological charge conservation, *J. Opt. Soc. Am. A* 25 (2008) 225. <https://doi.org/10.1364/JOSAA.25.000225>.

- [90] G.P. Berman, V.N. Gorshkov, S.V. Torous, Scintillation reduction for laser beams propagating through turbulent atmosphere, *J. Phys. B: At. Mol. Opt. Phys.* 44 (2011) 055402. <https://doi.org/10.1088/0953-4075/44/5/055402>.
- [91] H.T. Eyyuboğlu, Y. Baykal, X. Ji, Scintillations of Laguerre Gaussian beams, *Appl. Phys. B* 98 (2010) 857–863. <https://doi.org/10.1007/s00340-009-3702-x>.
- [92] A. Saito, A. Tanabe, M. Kurihara, N. Hashimoto, K. Ogawa, Propagation properties of quantized Laguerre-Gaussian beams in atmospheric turbulence, in: H. Hemmati, D.M. Boroson (Eds.), San Francisco, California, United States, 2016: p. 973914. <https://doi.org/10.1117/12.2212517>.
- [93] P. Martelli, A. Gatto, P. Boffi, M. Martinelli, Free-space optical transmission with orbital angular momentum division multiplexing, *Electron. Lett.* 47 (2011) 972. <https://doi.org/10.1049/el.2011.1766>.
- [94] Z. Liu, D. Zhao, Propagation of partially coherent vortex beams in atmospheric turbulence by a spatial light modulator, *Laser Phys. Lett.* 16 (2019) 056003. <https://doi.org/10.1088/1612-202X/ab0a6b>.
- [95] C.S.D. Stahl, G. Gbur, Twisted vortex Gaussian Schell-model beams, *J. Opt. Soc. Am. A* 35 (2018) 1899. <https://doi.org/10.1364/JOSAA.35.001899>.
- [96] K. Dong, M. Cheng, M.P.J. Lavery, S. Geng, P. Wang, L. Guo, Scattering of partially coherent vortex beam by rough surface in atmospheric turbulence, *Opt. Express* 30 (2022) 4165. <https://doi.org/10.1364/OE.444155>.
- [97] G. Gbur, Partially coherent vortex beams, in: D.L. Andrews, E.J. Galvez, J. Glückstad (Eds.), *Complex Light and Optical Forces XII*, SPIE, San Francisco, United States, 2018: p. 2. <https://doi.org/10.1117/12.2287170>.
- [98] W. Cheng, J.W. Haus, Q. Zhan, Propagation of scalar and vector vortex beams through turbulent atmosphere, in: O. Korotkova (Ed.), San Jose, CA, 2009: p. 720004. <https://doi.org/10.1117/12.809138>.
- [99] V.A. Banach, V.L. Mironov, S. Chomet, E.R. Pike, V.A. Banakh, V.L. Moronov, V.A. Banach, *LIDAR in a turbulent atmosphere*, Artech House, Boston, 1987.
- [100] Yu.N. Barabanenkov, Yu.A. Kravtsov, V.D. Ozhin, A.I. Saichev, II Enhanced Backscattering in Optics, in: *Progress in Optics*, Elsevier, 1991: pp. 65–197. [https://doi.org/10.1016/S0079-6638\(08\)70006-4](https://doi.org/10.1016/S0079-6638(08)70006-4).
- [101] O. Korotkova, Partially coherent beam propagation in turbulent atmosphere, with applications, VDM Verlag Dr. Muller, Saarbrücken, Ger., 2009.
- [102] O. Korotkova, Enhanced backscatter in LIDAR systems with retro-reflectors operating through a turbulent ocean, *J. Opt. Soc. Am. A* 35 (2018) 1797. <https://doi.org/10.1364/JOSAA.35.001797>.
- [103] J. Li, G. Martinez-Piedra, O. Korotkova, Enhanced Back-Scatter in double-pass optical links with non-classic turbulence, *Opt. Express* 26 (2018) 10128. <https://doi.org/10.1364/OE.26.010128>.
- [104] T. Zhou, J. Yu, F. Wang, Y. Cai, O. Korotkova, Effects of source spatial partial coherence on intensity statistics of optical beams in mono-static turbulent channels, *Opt. Express* 28 (2020) 20135. <https://doi.org/10.1364/OE.393805>.
- [105] S.S. Kashkarov, T.N. Nesterova, A.S. Smirnov, Light intensity fluctuations in backscatter from a turbulent medium, *Radiophys Quantum Electron* 27 (1984) 890–894. <https://doi.org/10.1007/BF01039452>.
- [106] P.R. Tapster, A.R. Weeks, E. Jakeman, Observation of backscattering enhancement through atmospheric phase screens, *J. Opt. Soc. Am. A* 6 (1989) 517. <https://doi.org/10.1364/JOSAA.6.000517>.

- [107] V.A. Myakinin, Observation of the improvement of image quality under active illumination through turbulence, *Optics Communications* 89 (1992) 164–166. [https://doi.org/10.1016/0030-4018\(92\)90152-H](https://doi.org/10.1016/0030-4018(92)90152-H).
- [108] A.S. Gurvich, Lidar sounding of turbulence based on the backscatter enhancement effect, *Izv. Atmos. Ocean. Phys.* 48 (2012) 585–594. <https://doi.org/10.1134/S0001433812060047>.
- [109] W. Nelson, J.P. Palastro, C. Wu, C.C. Davis, Enhanced backscatter of optical beams reflected in atmospheric turbulence, in: A.M.J. Van Eijk, C.C. Davis, S.M. Hammel (Eds.), San Diego, California, United States, 2014: p. 922411. <https://doi.org/10.1117/12.2062946>.
- [110] F. Reil, J.E. Thomas, Observation of Phase Conjugation of Light Arising from Enhanced Backscattering in a Random Medium, *Phys. Rev. Lett.* 95 (2005) 143903. <https://doi.org/10.1103/PhysRevLett.95.143903>.
- [111] J. Yu, Y. Huang, G. Gbur, F. Wang, Y. Cai, Enhanced backscatter of vortex beams in double-pass optical links with atmospheric turbulence, *Journal of Quantitative Spectroscopy and Radiative Transfer* 228 (2019) 1–10. <https://doi.org/10.1016/j.jqsrt.2019.02.021>.
- [112] G. Welch, R. Phillips, Simulation of enhanced backscatter by a phase screen, *J. Opt. Soc. Am. A* 7 (1990) 578. <https://doi.org/10.1364/JOSAA.7.000578>.

List of Papers Based on the Thesis

- **Journal papers**

- 1) Lekshmi S.R., Dinesh N. Naik, C.S. Narayanamurthy “Fried’s coherence length measurement of dynamic Kolmogorov type turbulence using the autocorrelation function”, (Journal of Optics, Volume 24, 2022 *J. Opt.* **24** 044010 DOI 10.1088/2040-8986/ac3f91)
- 2) Lekshmi S.R., Dinesh N. Naik & C.S. Narayanamurthy (2023) Insensitivity of partially coherent Gaussian -Schell model beams to the impact of dynamic Kolmogorov type turbulence, *Journal of Modern Optics*, 70:3, 161-169, DOI: 10.1080/09500340.2023.2219770
- 3) Lekshmi S.R., C.S. Narayanamurthy, The resilience of zero order Bessel–Gaussian Beams to the impact of dynamic Kolmogorov type of turbulence, *Optics Communications*, Volume 532,2023,129243,ISSN 0030-4018, DOI :<https://doi.org/10.1016/j.optcom.2022.129243>.
- 4) Lekshmi S R and C S Narayanamurthy , Robustness of partially coherent vortex beams to the impact of dynamic Kolmogorov kind of turbulence(physica scripta) 2024 *Phys. Scr.* **99** 035507 DOI 10.1088/1402-4896/ad1909

- **Conference papers**

- 1) Lekshmi, S.R., Narayanamurthy, C.S. (2021). Design of Photorefractive Waveplates Using Stokes Parameters. In: Singh, K., Gupta, A.K., Khare, S., Dixit, N., Pant, K. (eds) ICOL-2019. Springer Proceedings in Physics, vol 258. Springer, Singapore. https://doi.org/10.1007/978-981-15-9259-1_186
- 2) Lekshmi SR, Dinesh N. Naik, C S Narayanamurthy, Statistical properties of a Kolmogorov phasescreen (oral presentation), XLIV OSI Symposium on Frontiers in Optics and Photonics 2021 (FOP21), IIT Delhi.
- 3) Lekshmi S.R., C.S. Narayanamurthy, The resilience of zero order Bessel–Gaussian Beams to the impact of dynamic Kolmogorov type of turbulence (poster presentation), Women in Optics and Photonics India-2022, RRI Bangalore.

- **Papers under preparation**

- 1) Lekshmi SR, Dinesh N. Naik, C S Narayanamurthy, Enhanced backscattering through a Kolmogorov turbulence.